Fall 1-31-2011

Model reference control for ultra-high precision positioning systems

Lan Yu

New Jersey Institute of Technology

ABSTRACT

MODEL REFERENCE CONTROL FOR ULTRA-HIGH PRECISION POSITIONING SYSTEMS

by
Lan Yu

Due to the increasing demands of high-density semiconductors, molecular biology, optoelectronics, and MEMS/NEMS in the past decades, control of ultra-high precision positioning using piezoelectricity has become an important area because of its high displacement resolution, wide bandwidth, low power consumption, and potential low cost. However, the relatively small displacement range limits its application. This work proposed a practical ultra-high precision piezoelectric positioning system with a complementary high displacement range actuation technology. Solenoids are low cost, high speed electromagnetic actuators which are commonly used in on-off mode only because of the inherent high nonlinear force-stroke characteristics and unipolar forces (push/pull) generated by the magnetic fields. In this work, an integrated positioning system based on a monolithic piezoelectric positioner and a set of push-pull dual solenoid actuators is designed for high speed and high precision positioning applications. The overall resolution can be sub-nanometer while the moving range is in millimeters, a three order of magnitude increase from using piezoelectric positioner alone.

The dynamic models of the dual solenoid actuator and piezoelectric nano-positioner are derived. The main challenge of designing such positioning systems is to maintain the accuracy and stability in the presence of un-modeled dynamics, plant variations, and parasitic nonlinearities, specifically in this work, the friction and force-stroke nonlinearities of the dual solenoid actuator, and the friction, hysteresis and

coupling effects of piezoelectric actuator, which are impossible to be modeled accurately and even time–varying. A model reference design approach is presented to attenuate linear as well as nonlinear uncertainties, with a fixed order controller augmenting a reference model that embeds the nominal dynamics of the plant. To improve transient characteristics, a Variable Model Reference Zero Vibration (VMRZV) control is also proposed to stabilize the system and attenuate the adverse effect of parasitic nonlinearities of micro-/nano- positioning actuators and command-induced vibrations. The speed of the ultra-high precision system with VMRZV control can also be quantitatively adjusted by systematically varying the reference model. This novel control method improves the robustness and performance significantly. Preliminary experimental data on dual solenoid system confirm the feasibility of the proposed method.

MODEL REFERENCE CONTROL FOR ULTRA-HIGH PRECISION POSITIONING SYSTEMS

by
Lan Yu

A Dissertation
Submitted to the Faculty of
New Jersey Institute of Technology
in Partial Fulfillment of the Requirements for the Degree of
Doctor of Philosophy in Electrical Engineering

Department of Electrical and Computer Engineering

January 2011

APPROVAL PAGE

MODEL REFERENCE CONTROL FOR ULTRA-HIGH PRECISION POSITIONING SYSTEMS

Lan Yu

Dr. Timothy N. Chang, Dissertation Advisor — Date
Professor of Electrical and Computer Engineering, NJIT

Dr. Andrew Meyer, Committee Member — Date
Professor Emeritus of Electrical and Computer Engineering, NJIT

Dr. Richard A. Haddad, Committee Member — Date
Professor of Electrical and Computer Engineering, NJIT

Dr. Sui-hoi E. Hou, Committee Member — Date
Associate Professor of Electrical and Computer Engineering, NJIT

Dr. Zhiming Ji, Committee Member — Date
Associate Professor of Mechanical Engineering, NJIT

BIOGRAPHICAL SKETCH

Author: Lan Yu

Degree: Doctor of Philosophy

Date: January 2011

Undergraduate and Graduate Education:

- Doctor of Philosophy in Electrical Engineering,
  New Jersey Institute of Technology, Newark, NJ, 2010
- Master of Science in Control Science and Engineering,
  Harbin Institute of Technology, Harbin, P. R. China, 2005
- Bachelor of Engineering in Control Science and Engineering,
  Harbin Institute of Technology, Harbin, P. R. China, 2003

Major: Electrical Engineering

Presentations and Publications:

Yu, L., & Chang, T. N. (2010). Zero vibration on-off position control of dual solenoid actuator. IEEE Transactions on Industrial Electronics, Vol. 57, No. 7, 2519-2526.

Yu, L., & Chang, T. N. (2010). Model reference zero vibration control of ultrahigh precision piezoelectric nanopositioner. American Control Conference 2010.

Yu, L., & Chang, T. N. (2008). Variable model reference high precision position control of dual solenoid actuator. Industrial Electronics, IECON 2008. 34th Annual Conference of the IEEE.

Yu, L., & Chang, T. N. (2008). Model reference zero vibration balance control of dual solenoid position actuator. International Symposium on Flexible Automation.

Shen, Q., Chang, T. N., & Yu, L. (2008). Control and implementation of a real-time liquid spotting system for microarray applications. IEEE Transactions on Industrial Electronics, Vol. 55, No. 9, 3266-3272.

Yu, L., & Chang, T. N. (2007). Zero vibration on-off position control of dual solenoid actuator. Industrial Electronics, IECON 2007. 33rd Annual Conference of the IEEE.

Shen, Q., Chang, T. N., & Yu, L. (2007). Automated real-Time spotting system for DNA/protein microarray applications. Industrial Electronics, ISIE 2007. IEEE International Symposium.

To my beloved grandmother, parents, fiancé, and loyal four-leg friend.

I will always appreciate your love and support.

ACKNOWLEDGMENT

I wish to express my deepest gratefulness and respect to my dissertation advisor Dr. Timothy N. Chang for his guidance and insight throughout my research, and financial support during my study.

Many thanks go to my dissertation committee members, Dr. Andrew Meyer, Dr. Richard A. Haddad, Dr. Sui-hoi E. Hou, and Dr. Zhiming Ji for their valuable suggestions and comments.

For their expertise and technical assistance, I would like to thank Dr. Xuemei Sun, Dr. Puttiphong Jaroonsiriphan, Dr. Biao Cheng, Dr. Ding Yuan, Dr. Qiong Shen, Wei Shi, Jing Yang, and all the other colleagues and friends who made my stay at the university a memorable and valuable experience.

Lastly, but in no sense the least, I express my thanks and appreciation to my family for their great love, support and extraordinary encouragement.

TABLE OF CONTENTS

TABLE OF CONTENTS
(Continued)

Chapter **Page**

TABLE OF CONTENTS
(Continued)

Chapter **Page**

TABLE OF CONTENTS
(Continued)

Chapter **Page**

LIST OF TABLES

LIST OF FIGURES

LIST OF FIGURES
(Continued)

Figure **Page**

LIST OF FIGURES
(Continued)

LIST OF FIGURES
(Continued)

Figure **Page**

LIST OF SYMBOLS

A	Area of the gap
a	Error tolerance range of On-off control
$A_1^{'}, A_2^{'}$	Amplitudes of ZV command with set points r and initial position x_0
A_i	Amplitude of i^{th} impulse of ZV shaper
$\tilde{A}(\cdot)$	Area of the segment along the magnetic circuit
$Amp_{err}(i)$	Amplitude of the error when $t \in [\overline{t}_i, \overline{t}_{i+1})$
B	Magnetic flux density
Bal	Balance in balance control
d	Piezoelectric strain coefficient
d_0, β	Constants depending on the material and geometry of the solenoid
D	Electrical displacement
$D(s)$	Denominator polynomial
e	Energy stored in the gap of the solenoid
$e_y(t)$	Position error between the plant and the reference model
$e_v(t)$	Velocity error between the plant and the reference model
f	Friction
F	Magnetic force
F_c	Coulomb friction coefficient
F_v	Viscous friction coefficient

LIST OF SYMBOLS
(Continued)

$G(s)$	Transfer function of the plant
$G_0(s)$	Transfer function of inner closed-loop feedback controller
$G_1(s)$	Transfer function of model reference controller
$G_m(s)$	Transfer function of the reference model
h	Thickness of the PZT
$H(\cdot)$	Unit step function
i	Current that flows through the coil of solenoid
I	Electric field
K	Gain of balance control
K_e	Gain of On-off control
K_{MO}	Modify gain of balance control
k_i	Integral gain of PI controller for piezoelectric nano-positioner
k_{mp}	Proportional gain of model reference controller
k_p	Proportional gain of PI controller for piezoelectric nano-positioner
k_u	Constant for the model of piezoelectric nano-positioner
l	Length of the PZT
m	Mass of the plunger
N	Number of turns in the coil
$N(s)$	Numerator polynomial

LIST OF SYMBOLS
(Continued)

P_x	Pressure produced by the deformation
r	Amplitude of the reference command
R	Resistance of the coils of the solenoid
$\tilde{r}(t)$	Shaped command filtered by the ZV shaper
S	Strain
s^E	Elastic coefficient
sgn (.)	Signum function
T	Stress
$\overline{t_i}$	Zero speed time instances
t_p	Peak time of transient response of 2^{nd} order system
u	Control command
u_0	On-amplitude of On-off control
$\tilde{\mu}(\cdot)$	Permeability of the segment along the magnetic circuit
V	Residual vibration
v	Velocity of the plant
v_m	Velocity of the reference model
V_x	Driving voltage on the x-axis electrodes pair of PZT
V_y	Driving voltage on the y-axis electrodes pair of PZT
w	Air gap length

LIST OF SYMBOLS
(Continued)

x_{max}	Maximum travel of the plunger
$\bar{X}$	Equilibrium point for linearization
y	Displacement of the plant
y_m	Displacement of the reference model
Y_{11}^E	The Young's modulus
ε^T	Dielectric coefficient
ζ_m	Damping ratio of 2nd-order reference model
ζ	Damping ratio of 2nd-order plant
λ	Flux linkage
λ_ϕ	Flux leakage coefficient
μ_0	Permeability in free space
ω_m	Natural frequency of 2nd-order reference model
ω_n	Natural frequency of 2nd-order plant

CHAPTER 1

INTRODUCTION

Over the past two decades, the explosive growth of engineering research in the field of nanotechnology is expected to lead breakthroughs in the areas of biotechnology, manufacturing, high-density semiconductors, optoelectronics and defense. Among those areas, controlling the ultra-high precision devices and materials plays a critical role in achieving successful progress. Ultra-high precision technology involves precision control and manipulation of devices and materials at micro-/nano-scale. This chapter presents an overview of the available ultra-high precision positioning applications, and challenges in Section 1.1. Two types of actuators, solenoids and piezoelectric ceramics, which are implemented in the ultra-high precision positioning system presented in this work are introduced in Sections 1.2 and 1.3 respectively. The outline of the dissertation is presented in Section 1.4.

1.1 Ultra-high Precision Positioning Systems

Ultra-high precision positioning technology is manipulating mechatronic systems to move objects over a small range with a resolution down to a fraction of an atomic diameter with the contribution of accurate precision sensing and efficient control methods. How to design and manipulate the positioning system with extremely high resolution, bandwidth, accuracy, and stability are the main issues in ultra-high positioning technology. This section reviews recent improvements and implementations in the field of ultra-high precision positioning.

1.1.1 Ultra-high Precision Positioning Systems and Applications

The invention and application of the scanning tunneling microscope (STM) (Binnig et al. in 1982), the atomic force microscope (AFM) (Binnig et al in 1986), and the scanning probe microscope (SPM) (Wiesendanger in 1994) have encouraged the research in high precision positioning technology significantly in the past decades. Zou et al. presented some control issues in high-speed AFM for biological applications in 2004. A MEMS-based scanning-probe is presented to position the storage medium in the data-storage devices in two dimensions (Pantazi et al. in 2007). Owing to the increasing areal density of hard-disk drives (HDDs), ultra-high precision dual-stage servo systems are applied to position the read-write head over smaller data tracks (Kobayashi et al. in 2001, and Kim et al. in 2004). Novel ultra-high positioning tools are also needed for lithography systems (Vettiger et al. in 1996), semiconductor inspection systems (Verma et al. in 2005), and mask alignment systems for imprint lithography (White et al. in 2000).

Furthermore, the micro-/nano-positioning technologies play critical roles in molecular biology for alignment and extreme accurate manipulation, such as cell tracking, nano-material testing, DNA analysis, and nanoassembly (Meldrum et al. 2001). Rihong et al. implemented a micro-/nanopositioner on to the optical alignment system to realize the CCD parameter measurement in 1998.

1.1.2 Actuators for Ultra-high Precision Systems

For the ultra-high precision systems actuators and sensors must have the properties of high resolution and bandwidth. The dimension, weight, displacement range, and power consumption are also important issues to be considered under diverse working conditions among the vast range of applications. The ultra-high precision actuators studied in the

recent years can be classified by the type of materials, which include piezoelectric, electrostatic, electromagnetic, magnetostrictive and thermal actuators (Devasia et al. in 2007).

Among various operating principles, piezoelectric is currently the dominant type in building micro-/nanopositioner because of its improving characteristics such as high resolution, fast response, its scale factor, linearity and stability. It is implemented in many fields such as scanning near field optical microscopy (Paesler et al. in 1996), scanning tunneling microscopy, and high frequency vibration control. The main drawback of piezoelectric actuators is the relatively small range of displacement. Besides the ceramic piezoelectric devices based on lead zirconate titanate (PZT) which are implemented commonly, some thin-film-based devices have emerged recently (Fukada in 2000).

The electromagnetic actuator generates forces by the flow of current through coils of wires in the presence of a magnetic field, which have the advantages of low power consumption and large travel range (Despont et al. in 2007). Magnetostrictive actuators which are made of magnetostrictive or piezomagnetic material offer the larger displacement range and ratio of mass per unit stress compared with piezoelectric actuators (Ueno et al. in 2003).

The inchworm actuator is an electrostatic design with clamp and slip motion (Tas et al. in 1998). The inchworm actuator, also called the shuffle actuator, only can offer 1-DOF movement until now (Albrecht et al. in 2004). However, it tends to wear out due to the shuffling motion.

Other designs of electrostatic actuators include interdigitated comb actuators, and parallel-plates actuators, which have been explored as the secondary actuators in dual

stage servo systems of hard-disk drives because of the ease of fabrication (Horowitz et al. in 2004). Potential problems exist in their high power consumption and relative weak force.

1.1.3 Sensors for Ultra-high Precision Systems

Accurate position sensing of the motion and feedback control methodology is the key to successful ultra-high precision positioning. Among the variety of sensing techniques, piezoresistive position sensors (Pedrak et al. in 2003), optical position sensors (Yu et al. in 2007), capacitive position sensors (Chang et al in 2001), thermal position sensors (Lantz et al. in 2005), and inductive position sensors (Brinkerhoff et al. in 2000), are widely used in ultra-high positioning applications. The choice of the position-sensing mechanism depends on its simplicity, linearity, and bandwidth. Working environment and resolution requirement of the ultra-high precision systems are also necessary considerations.

1.2 Piezoelectric Actuators

In recent years, a number of piezoelectric high precision actuators have been invented. This section discusses some characteristics of piezoelectric materials, and challenges on the design of the nanopositioners presented in this work.

1.2.1 Direct and Converse Piezoelectric Effect

In 1880, the Curie brothers discovered the piezoelectric effect: some crystals show positive and negative charges on certain portions of surfaces when they are squeezed in particular directions, and these charges disappear when the pressure is released. The generated charges are proportional to the pressure (Arnau in 2004). However, the use of

piezoelectric materials as nanopositioners exploits the converse piezoelectric effect: the application of an electric field causes a deformation in the piezoelectric materials, which was predicted by Lippmann and experimentally verified by the Curie brothers (Ballato in 1996). The direct and converse piezoelectric effects are described in equation (1.1) and (1.2) respectively.

$$D_m = D_{mi} T_i + \varepsilon^T_{mk} I_k \tag{1.1}$$

$$S_i = s^E_{ij} T_j + d_{mi} I_m \tag{1.2}$$

in which S, T, D and I represent strain, stress, electrical displacement and electric field respectively; s^E, d and ε^T represent the elastic, piezoelectric strain and dielectric coefficients which depend on materials; the indexes $i, j = 1, 2, ..., 6$ and $m, k = 1, 2, 3$ refer to directions within the Cartesian coordinate system as shown in Figure 1.1. The first index refers to the stimuli direction, while the second refers to the reaction direction (IEEE standard on piezoelectricity, 1988).

Figure 1.1 shows the converse effect on the monolithic cruciform piezoelectric actuator studied in this work. When the voltage is applied on the shadow section III, a deformation along y axis is produced.

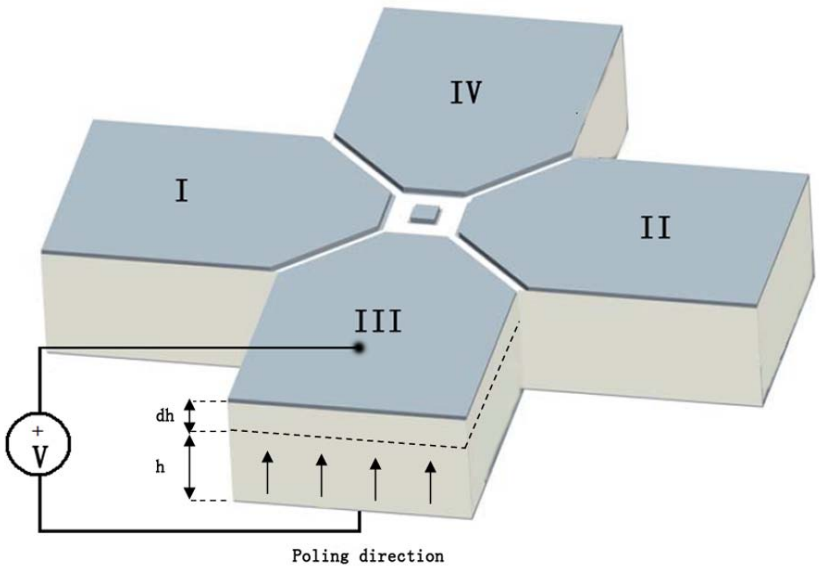

Figure 1.1 Converse effects on the monolithic cruciform piezoelectric actuator.

1.2.2 Polarization

The reason for the electric dipole behavior is the separation of charges between the positive and negative ions. Before the polarization treatment, the groups of dipoles are randomly oriented in the raw ceramic material such that the material is isotropic and does not exhibit the piezoelectricity (Figure 1.2 (a)). To change this state, a strong DC electric field (>2,000V/mm) is applied to the heated piezo ceramics. The material expands along the axis of the applied field and contracts perpendicular to that axis (Figure 1.2 (b)). The electric dipoles align and roughly stay in alignment upon cooling. As a result, there is a distortion that causes growth in the dimensions aligned with the field and a contraction along the axes normal to the electric field (Figure 1.2 (c)). When an electric voltage is applied to a polarized piezoelectric material, the Weiss domains increase their alignment proportional to the voltage. The result is a change of the dimensions (expansion, contraction) of the piezoelectric material.

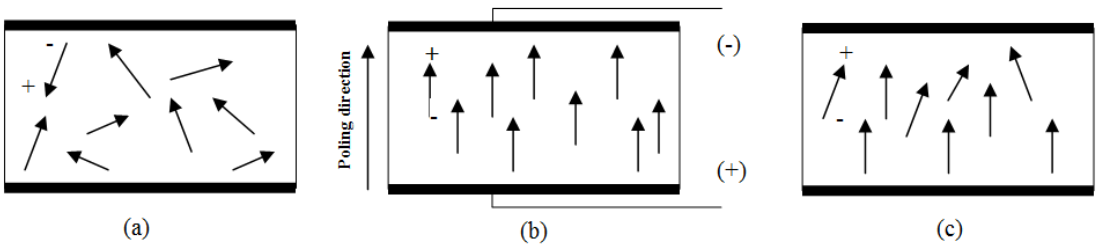

Figure 1.2 Polarization process: (a) Prior to polarization; (b) Polarization; (c)After polarization.

It should be mentioned that piezoelectric ceramics are ferroelectric materials, which have non-centrosymmetric unit cells below a critical temperature, called Curie temperature. Above the Curie temperature, these ceramics have a centrosymmetric structure so that there is no dipole moment and no piezoelectric characteristics. The polarization is usually processed at a temperature slightly below the Curie temperature.

1.2.3 Creep

When the operating voltage of a piezoelectric actuator increases, the remnant polarization continues to increase. This undesired effect is called creep, since there is a slow creep after the voltage change completes. It may affect the accuracy especially for the high speed positioning applications. Equation (1.3) and (1.4) give the nonlinear model (Jung et al. in 2000) and linear transfer function (Croft et al. in 2001) of the creep effect respectively.

$$x(t) = x_0\left[1+\gamma \log\left(\frac{t}{t_0}\right)\right] \tag{1.3}$$

$$C(s) = \frac{1}{k_0} + \sum_{i=1}^{3} \frac{1}{c_i s + k_i} \tag{1.4}$$

in which $x(t)$ is a PZT actuator's displacement for any fixed input voltage; $C(s)$ is the transfer function of the measured displacement response over the input voltage affecting the movement; $\gamma, k_0, c_i,$ and k_i are constants decided by the actuator behavior; t_0 is initial time when the creep effect appears; and x_0 is the displacement at time t_0.

1.2.4 Hysteresis

Hysteresis is one of inherent nonlinearities in piezoelectric ceramics. Such effect increases when the electric field strength or the piezoelectric sensitivity of the material increases. Hysteresis loop is due to the alternation of Weiss domains direction resulting from the change of the electric field. Thus the effects of creep and hysteresis are not mutually exclusive.

Hysteresis effect is related to the amplitude and frequency of the driving voltage. There are six popular hysteresis models applied to modeling the piezoelectric ceramic positioning system: hysteron model, Bouc-Wen model, Chua-Stromsmoe model, Preisach model, Dahl model, and Maxwell resistive capacitor model. Hysteron model is defined on piecewise monotone continuous inputs (Sain et al. in 1997). Bouc-Wen model represents a large number of hysteresis effects. Chua-Stromsmoe model suits for modeling ferromagnetic hysteresis which has saturation characteristics (Sun in 2001). Preisach model is expressed as double integral of the outputs of an ideal relay (Mrad et al. in 2002). Dahl model is built based on the friction theory (Dahl in 1976).

1.3 Solenoid Actuators

Solenoids are widely used as actuators to convert electrical energy into mechanical linear movement. They are simple in construction and low cost. Common applications are

limited to the on-off movements, because of their inherent non-linear force-stroke characteristics (Xu and Jones in 1997). For example, switches, relays, solenoid valves (Wang et al. in 2002) and many other movements from one end to the other end. There is very little research dealing with position control using solenoids.

Solenoids are designed to have the force in only one direction, which can be either push or pull. Thus there is a need of some sort of return force to restore the plunger to its original de-energized position. There are mainly three ways to generate the return force. One way is to use AC source solenoid which could change the direction of magnetic field constantly. This field reversal causes significant losses in the metal structure unless meticulous steps are taken during the design. Moreover, when the plunger is in its total de-energized position, magnetic field attraction is the weakest, which could have an adverse effect on the rapid performance of the solenoid. The second way is to use a spring (Cheung et al. in 1993). The plunger extends outward by releasing the energy from the spring. Now since there is energy stored in the system most of the time, it is less efficient to stabilize and control, especially for position control instead of just on/off movement. The third way is to connect two solenoids in the opposite position so that only one solenoid is activated to generate push or pull movement at any given time (Li and Yuan in 2004). In this paper, the third method is implemented in the ultra-high precision positioning presented in this work to achieve continuous movement.

The friction effect between the push-pull plunger and the cores of solenoids is another issue in controlling the solenoid actuators. Wang et al. (2002) applied Coulomb friction model in their electromechanical valve actuator model.

1.4 Outline of the Dissertation

This first chapter presents an overview of ultra-high precision positioning technology and devices (actuators and sensors). Two types of high precision positioning actuators, solenoids and piezoelectric actuators are introduced respectively. It also gives some background on the challenges of the previously proposed control schemes associated with the two types of actuators, and presents the design philosophy that will be studied in this work. At the end of this chapter, the principle contributions of this work will be outlined.

Presented in Chapter 2 are literature reviews on controller development for ultra-high-precision positioning systems, especially for systems with uncertainties and parasitic nonlinearities. In Chapter 3, a novel controller called Viable Model Reference Zero Vibration (VMRZV) is proposed to attenuate the uncertainties of the physical plant. The VMRZV method is implemented to a generic second order system with friction nonlinearity, which is a common model of the ultra-high precision positioning system. The related theoretical derivations and simulation results are also illustrated in this chapter.

Chapter 4 introduces the design, modeling and control of a dual solenoid micro-positioning actuator. Some feedback controllers, Balance control and On-off control, are proposed to stabilize the solenoid systems. A feedforward control strategy, Zero Vibration input shaping, is designed according to various feedback controllers. The relative simulation results are discussed at the end of this chapter. Chapter 5 deals with the modeling and control design of piezoelectric cruciform nano-positioning actuator.

Chapter 6 illustrates the experimental setup of the ultra-high precision positioning system. In this work, an integrated positioning system based on a monolithic piezoelectric

nanopositioner and a set of push-pull dual solenoid actuators is designed for high speed and high-precision positioning applications. The overall resolution can be sub-nanometer while the moving range is in millimeters, a three order of magnitude increase from using a piezoelectric positioner alone. The hardware and software configurations for the real time control platform are introduced.

Chapter 7 compares various control schemes mentioned above by implementing them on the ultra-high precision positioning systems. The effects and merits of the VMRZV are addressed according to the experimental data. Finally, Chapter 8 summarizes the current results and future work.

CHAPTER 2

LITERATURE SURVEY

The micro-/nanoscale fabrication techniques and physical effects found on the micro-/ nanoscales may create geometric, parametric, and dynamic uncertainties in the components of ultra-high precision systems. For example, the uncontrolled chemical processes in the fabrication sequence may cause parametric uncertainties (Shapiro in 2005). Besides, dynamic uncertainties arise from poorly understood or unknown physical phenomena. The reduced-order model which aids the control design on the micro-/nanoscale may lose some high frequency dynamics. Another type of unmodeled dynamics is the cross coupling effects between two axes.

Undesirable nonlinear properties of the actuator degrade the precision and speed of the positioning system, for example, the friction force between plunger and cores of the solenoids, the friction force between the piezoelectric ceramic and the frame, the creep and hysteresis effects in the piezoelectric ceramic. Friction forces between sliding surfaces have discontinuous behavior around zero velocity. A large amount of research has been directed at modeling the friction phenomenon. Armstrong-Helouvry et al. (1994) and Olsson et al. (1998) provided a comprehensive review of the research on friction modeling and compensation. Most of the studies of friction phenomenon concentrate on contact surface with grease or oil lubrication, which induces significant Stribeck effect (Armstrong-Helouvry et al. in 1994), as shown in Figure 2.1 (a). The friction model used in this study is a Coulomb friction plus viscous friction shown in Figure 2.1(b). Although this model is simple, it represents the dominant effects of friction in most real systems with dry contact surfaces. Furthermore, Coulomb friction can be a major detriment to the

performance of high precision systems (Hekman et al. 2004). Control of the system must allow for and design around these unavoidable fabrication uncertainties, un-modeled dynamics, plant variations, and parasitic nonlinearities. This chapter deals with literature reviews on controller development for ultra-high precision positioning systems, especially for the system with uncertainties and parasitic nonlinearities.

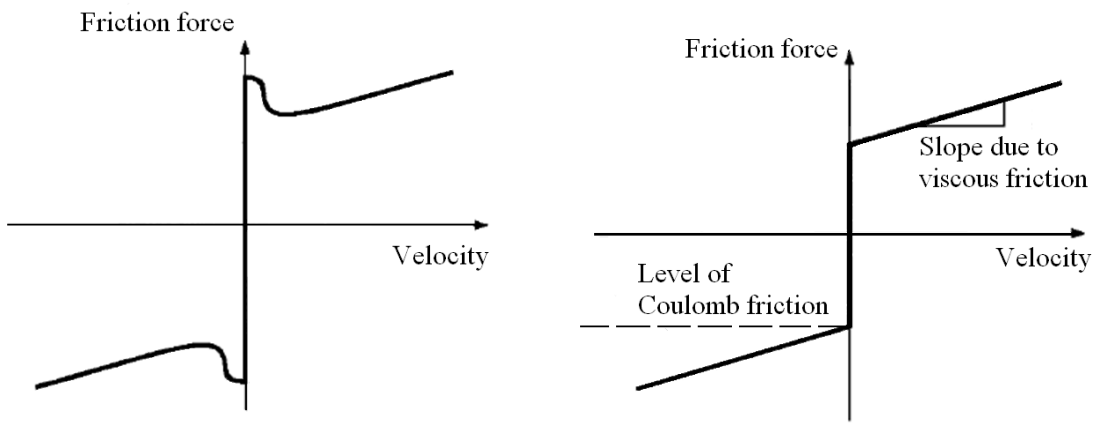

(a) Stribeck curve (b) Coulomb friction plus viscous friction

Figure 2.1 Modeling of friction (Olsson et al. in 1998**).**

Figure 2.2 indicates the generic structure of ultra-high precision positioning control system, which integrates the feedforward and feedback controllers. Among numerous feedback control methods, Proportional-integral-derivative (PID) and proportional-double-integral (PII) controllers are the most common forms of feedback controllers currently used for ultra-high precision positioning systems, since they are simple and reliable to provide high gain feedback at low frequency (Kouno in 2006). Feedforward controllers, such as input shaping method (Singer et al. in 1990) can improve the transient tracking performance without incurring the stability problems that

are associated with feedback design. Kenison and Singhose (2000) presented a concurrent design of the PID and input shaping control for insensitivity to parameter variations. However, both input shaping and PID designs lack robustness (Tan in 2005). More robust controllers are necessary since uncertainties may exacerbate performance such as the steady state error, and transient response in ultra-high precision systems.

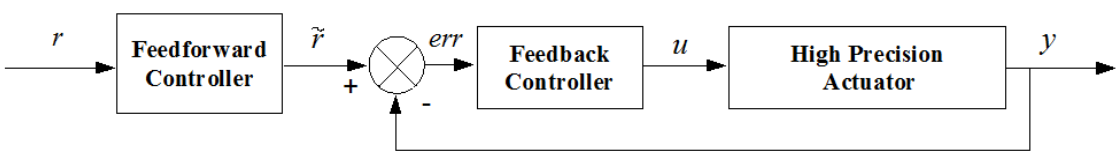

Figure 2.2 Block diagram of ultra-high precision positioning system.

Many efforts have been made to counter the nonlinear effects. One straightforward way is to change the method of open-loop implementation. For example, the hysteresis effect can be substantially eased by replacing voltage control with charge control (Kaizuka in 1989). The nonlinear dynamic model of solenoid system can be simplified using current control instead of voltage control (Yuan in 2004). This method can not be widely used since it depends on the unique properties of diverse precision actuators. Furthermore, the change of implementation methodology may lead to other problems. Charge control in the piezoelectric actuator achieves lower hysteresis but leads to more creep, less travel and a lower positioning bandwidth (Sebastian in 2005).

Adaptive and interactive control strategy can combine with the feedback and feedforward controller mentioned above to increase the robustness of the system. For example, the PID parameters are designed to be tuned automatically via a learning nonlinear PID controller (Tan et al. in 2001). An interactive learning input shaping is

applied to suppress the time-varying nonlinear residue vibration (Park et al. in 2006). Cutforth and Pao (2002) presented an adaptive input shaper which provides robustness to parameter uncertainty by tuning the shaper to the flexible mode frequency.

Furthermore, adaptive algorithms can be applied to estimate or identify the nonlinearity of the system, and thereby to improve the precision of the positioning systems. Sato et al. (2004) proposed an adaptive friction compensation strategy based on the notion of H_∞ optimality. Neural-Network is used to parameterize the nonlinear characteristic function of the friction model. Tan and Baras (2005) developed an adaptive inverse control scheme where one aims to cancel out the nonlinear effect by identifying and updating the inverse of the model adaptively. Tsang and Li (2001) used a robust nonlinear model as the reference model to overcome the dead zone adaptively. A challenge in iterative approaches is the difficulty in proof of its convergence.

Robust control is another approach that deals with those uncertainties and nonlinearities. Tsai and Chen (2003) developed a Smith predictor-based robust controller for piezoelectric actuator. A hysteresis model which consists of a variable gain and a variable time-delay is approximated to achieve high-precision tracking. Salapaka et al. (2005) designed a modern robust H_∞ controller which demonstrates substantial improvements in the nano-positioning speed and precision, while eliminating the undesirable nonlinear effects of the actuator. The Glover–McFarlane design was proposed by Sebastian et al. (2005) particularly to robustify an existing controller with specific tracking requirements such as having to track ramp signals with zero steady-state error.

Several feedforward input shapers which use sensor feedback information to minimize the residual vibration are designed to deal with system nonlinearities. For

example, Park and Chang (2001) used a learning scheme to update the input shaper parameters for repetitive motion tasks. Dijkstra and Bosgra (2003) applied the iterative learning control method in designing the input signal for a point-to-point motion control on a high precision wafer-stage. Lawrence and Hekman (2002 and 2005) proposed an input shaper design method to compensate the Coulomb friction. Heckman et al. (2004) showed that the input shaping is effective in reducing vibration levels in position control under the effects of Coulomb friction on a solder cell machine. However, the parameter of Coulomb friction must be known when designing the proposed input shaping methods.

Another feedforward methodology, called inversion based (model-based) feedforward controller which invert mathematical models of the nonlinearity to determine its compensation input, is popular for high precision system (Devasia in 2002). Schitter and Stemmer (2004) presented a similar model-based feedforward controller which inverse the linear dynamic model of the system to increase the bandwidth. The challenge is the computational complexity of the inversion.

To compromise the computation efficient, design complexity and performance in ultra-high precision positioning systems, viable model reference control with input shaping method is proposed in this work to attenuate the effects of uncertainties.

CHAPTER 3

VARIABLE MODEL REFERENCE ZERO VIBRATION CONTROL DESIGN

3.1 Introduction

In industrial applications, the plant parameters and uncertainties keep changing with operating environment and conditions. Those un-modeled effects may degrade the precision and speed of the system significantly. The main challenge of manipulating ultra-high precision systems is how to maintain the accuracy and stability in the presence of plant variations and parasitic nonlinearities, in particularly, when the characteristics of those uncertainties are poorly known and time-varying. Model-based control design offers an efficient method to drive such systems behave like the desired model. The use of fixed-structure model reference controller results in faster computation and improves the overall robustness.

This chapter offers an effective control method, called Variable Model Reference Zero Vibration Control (VMRZV), to compensate these nonlinearities without knowing the accurate model, which is impossible to achieve actually. VMRZV combines the advantages of zero vibration input shaping and model reference control to handle linear as well as nonlinear uncertainties. The model reference control has a fixed order controller augmenting a reference model that embeds the nominal dynamics of the plant. The proposed method is inspired, in part, by model reference adaptive methods, in which the linear plant dynamics are regulated adaptively to approach those of a reference model. This novel control method improves the robustness and performance significantly.

3.2 Zero Vibration Input Shaping

3.2.1 Zero Vibration Shaper Design

Input shaping is a feed forward technique to suppress command–induced vibrations (Singer and Seering, 1990). It is assumed that the positioning system has been stabilized via feedback close loops. Without loss of generality, the closed loop positioning system is assumed to be modeled as a second-order underdamped system:

$$G(s)=\frac{\omega_m^2}{s^2+2\zeta_m\omega_m s+\omega_m^2} \tag{3.1}$$

in which ζ_m and ω_m represent the damping ratio and natural frequency. The unit impulse response of Equation (3.1) is given as:

$$y(t)=\frac{1}{\sqrt{1-\zeta_m^{\,2}}}e^{-\zeta_m\omega_m(t-t_0)}\cos\left(\left(\omega_m\sqrt{1-\zeta_m^{\,2}}\right)(t-t_0)+\theta\right)H(t-t_0) \tag{3.2}$$

where t_0 is the impulse time, $\theta=\tan^{-1}\left(\frac{\zeta_m}{\sqrt{1-\zeta_m^{\,2}}}\right)$, and $H(\cdot)$ is the unit step function:

$$H(t)=\begin{cases}1, & t\geq 0;\\ 0, & t<0.\end{cases} \tag{3.3}$$

Let $y_i(t)$ be the response to impulse

$$A_i\delta(t-t_i)=\begin{cases}+\infty, & t=t_i\\ 0, & t\neq t_i\end{cases},\qquad i=1,2,\cdots,m; \tag{3.4}$$

$$\int_{-\infty}^{\infty} A_i \delta(t) dt = A_i \tag{3.5}$$

The total response to a succession of impulses of amplitude A_i and delay time t_i

$$y(t) = \sum_{i=1}^{m} y_i(t) \tag{3.6}$$

where

$$y_i(t) = \frac{A_i}{\sqrt{1-\zeta_m^{\,2}}} e^{-\zeta_m \omega_m (t-t_i)} \cos\left(\left(\omega_m \sqrt{1-\zeta_m^{\,2}}\right)(t-t_i) + \theta\right) H(t-t_i) \tag{3.7}$$

Let

$$B_i = \frac{A_i}{\sqrt{1-\zeta_m^{\,2}}} \tag{3.8}$$

and

$$\omega_d = \omega_m \sqrt{1-\zeta_m^{\,2}} \tag{3.9}$$

The total response at settling time $t = t_N$ can be written as:

$$y(t_N) = \sum_{i=1}^{m} B_i e^{-\zeta_m \omega_m t_N} e^{\zeta_m \omega_m t_i} \cos\left(\omega_d (t_N - t_i) + \theta\right) \tag{3.10}$$

Alternatively,

$$y(t_N) = e^{-\zeta_m \omega_m t_N} \left\{ \left[\sum_{i=1}^{m} B_i e^{\zeta_m \omega_m t_i} \cos(\omega_d t_i) \right] \cos(\phi) + \left[\sum_{i=1}^{m} B_i e^{\zeta_m \omega_m t_i} \sin(\omega_d t_i) \right] \sin(\phi) \right\} \tag{3.11}$$

in which $\phi = \omega_d t_N + \theta$. By eliminating the $\sin(\phi)$ and $\cos(\phi)$ terms, the residual vibration $V(\omega_m, \zeta_m, t_N)$ can be expressed as:

$$V(\omega_m, \zeta_m, t_N) = |y(t_N)|$$
$$= e^{-\zeta_m \omega_m t_N} \sqrt{\left[\sum_{i=1}^{m} B_i e^{\zeta_m \omega_m t_i} \cos(\omega_d t_i)\right]^2 + \left[\sum_{i=1}^{m} B_i e^{\zeta_m \omega_m t_i} \sin(\omega_d t_i)\right]^2} \qquad (3.12)$$
$$\text{for} \quad t_N > t_1, t_2 \cdots, t_m.$$

Now since $V(\omega_m, \zeta_m, t_N)$ also depends upon A_i and t_i for $i = 1, 2, \cdots, m$, it is possible to solve for A_i and t_i to zero out the residual vibration. In the case of two impulses, i.e. $m = 2$, the Zero Vibration (ZV) shaper (Singer and Seering in 1990) corresponds to a sequence of two impulses. Its parameters are obtained by setting the residual vibration Equation (3.12) to zero with constraints $\sum A_i = 1$ and $A_i > 0$ for $i = 1, 2$. This gives

$$B_1 e^{\zeta_m \omega_m t_1} \cos(\omega_d t_1) + B_2 e^{\zeta_m \omega_m t_2} \cos(\omega_d t_2) = 0 \qquad (3.13)$$

$$B_1 e^{\zeta_m \omega_m t_1} \sin(\omega_d t_1) + B_2 e^{\zeta_m \omega_m t_2} \sin(\omega_d t_2) = 0 \qquad (3.14)$$

On substituting $t_1 = 0$, and $B_i = \dfrac{A_i}{\sqrt{1 - \zeta_m^{\,2}}}$ into (3.13) and (3.14), the following equations are obtained:

$$\frac{A_1}{\sqrt{1-\zeta_m^{\,2}}}+\frac{A_2}{\sqrt{1-\zeta_m^{\,2}}}e^{\zeta_m\omega_m t_2}\cos\left(\omega_d t_2\right)=0 \tag{3.15}$$

$$\frac{A_2}{\sqrt{1-\zeta_m^{\,2}}}e^{\zeta_m\omega_m t_2}\sin\left(\omega_d t_2\right)=0 \tag{3.16}$$

Since $\sin\left(\omega_d t_2\right)=0$, when $\omega_d t_2=n\pi$, therefore

$$t_2=\frac{n\pi}{\omega_d}=\frac{n\pi}{\omega_m\sqrt{1-\zeta_m^{\,2}}} \tag{3.17}$$

$$A_1+A_2e^{\frac{n\zeta_m\pi}{\sqrt{1-\zeta_m^{\,2}}}}\cos\left(n\pi\right)=0 \tag{3.18}$$

However, the choice of $n=0,2,4,\ldots$ violates the constraint $A_i>0$, for $i=1,2$ and is therefore eliminated from the solution set. For $n=1,3,5,\ldots$, $\cos\left(n\pi\right)=-1$, applying the same constraint $A_1+A_2=1$ into Equation (3.18) and solving for A_1 and A_2, the following expressions are obtained:

$$A_1=\frac{1}{1+M_p^{\,n}}\ ,\quad A_2=\frac{M_p^{\,n}}{1+M_p^{\,n}} \tag{3.19}$$

where

$$M_p=e^{-\frac{\zeta_m\pi}{\sqrt{1-\zeta_m^{\,2}}}}\ \text{, and } n=1,3,5,\ldots. \tag{3.20}$$

Equation (3.19) constitutes the solution set that satisfies the constraint $A_i > 0$. To achieve high speed point-to-point movement, n is set to 1 for the ZV shaper design in positioning systems. If the ZV shaper is designed according to the nominal damping ratio and natural frequency:

$$\zeta_m = 0.03, \quad \omega_m = 100 \tag{3.21}$$

The amplitude and time of the impulses are achieved based on equation (3.17), (3.19), and (3.20) with $n = 1$.

$$\begin{aligned} A_1 &= 0.5236, \quad A_2 = 0.4764, \\ t_1 &= 0\,\text{sec}, \quad t_2 = 0.0314\ \text{sec} \end{aligned} \tag{3.22}$$

For most of positioning systems, the objective is to move the plant from its starting position to a desired location as accurately as possible. The reference command is step function that is defined as,

$$r(t) = r \cdot H(t) \tag{3.23}$$

in which r is the amplitude of the reference command, and $H(t)$ is the unit step function defined in equation (3.3). The shaped command filtered by the ZV shaper is represented as:

$$\tilde{r}(t) = r\left[A_1 \cdot H(t) + A_2 \cdot H(t - t_2)\right] \tag{3.24}$$

Figure 3.1 illustrates the general input shaping convolution scheme.

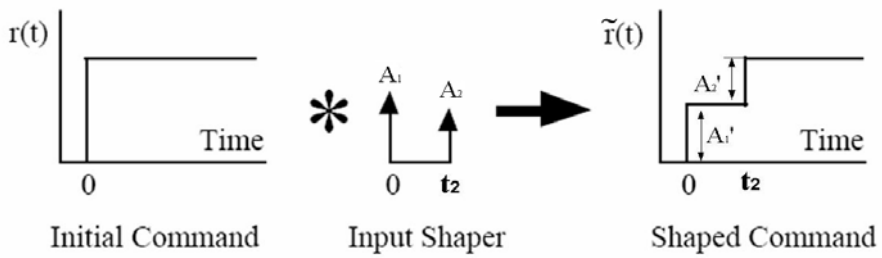

Figure 3.1 Input shaping a step to produce staircase command (Singer et al. in 1990).

3.2.2 ZV Design on Ultra-high Positioning Systems with Friction

For the ultra-high precision positioning system, friction is a common and un-ignorable phenomenon. Without loss of generality, it is assumed that the ultra-high precision system with feedback controller shown in Figure 2.2 can be modeled as a stable underdamped second-order system with friction. The feedforward controller, ZV shaper, is designed according to the model presented in equation (3.25).

$$\begin{aligned} \frac{dy}{dt} &= v \\ \frac{dv}{dt} &= -2\zeta\omega_n v - \omega_n^2 y + u\omega_n^2 - f \end{aligned} \tag{3.25}$$

In equation (3.25), u is the control command; ζ and ω_n represent the damping ratio and natural frequency of the second-order oscillator respectively without any friction; f represents the total friction force represented in equation (3.26); and for a positioning

system, y could represent the displacement of the actuator, and v represents the velocity of the actuator.

Friction is one of the common nonlinearities encountered in high precision applications. H.Olsson et al. (1998) has summarized the friction phenomenon and friction model. Considering the accuracy of the model, complexity of analysis, and efficiency of computation, the friction f in equation (3.25) can be adequately modeled as Coulomb friction plus viscous friction:

$$f = F_v v + F_c \operatorname{sgn}(v) \tag{3.26}$$

In equation (3.26), friction depends on the amplitude and the sign of the plant velocity: F_v is the positive viscous friction coefficient; F_c is the positive Coulomb friction coefficient; and sgn (.) is the signum function with respect to the relative speed of the linear movement defined as follows,

$$\operatorname{sgn}(v) = \begin{cases} 1, & v > 0 \\ 0, & v = 0 \\ -1, & v < 0 \end{cases} \tag{3.27}$$

However, because of the existence of friction the ZV shaper given by (3.17) and (3.19) ~ (3.20) doesn't result in zero residual vibration. The effects of Coulomb friction and viscous friction are discussed in this subsection separately.

Condition 1: If there is only viscous friction, which means that the Coulomb friction coefficient F_c equals to zero, the feedback positioning system (3.25) can be rewritten in the following form,

$$\begin{aligned} \frac{dy}{dt} &= v \\ \frac{dv}{dt} &= -2\left(\zeta + \frac{F_v}{2\omega_n}\right)\omega_n v - \omega_n^2 y + u\omega_n^2 \end{aligned} \tag{3.28}$$

It is assumed that the damping ratio and natural frequency are the same as the nominal ones, ζ_m and ω_m in equation (3.21), the ZV shaper designed in equation (3.22) is implemented on plant (3.25). Simulation data indicate that the presence of damping ratio variation introduced by viscous friction leads to nonzero residual vibration. Figure 3.2 illustrates the relationship between the amplitude of viscous friction and the residual vibration based on the simulation data of step response with amplitude 1×10^{-3}. The residual vibration increases with respect to the increase of the viscous friction.

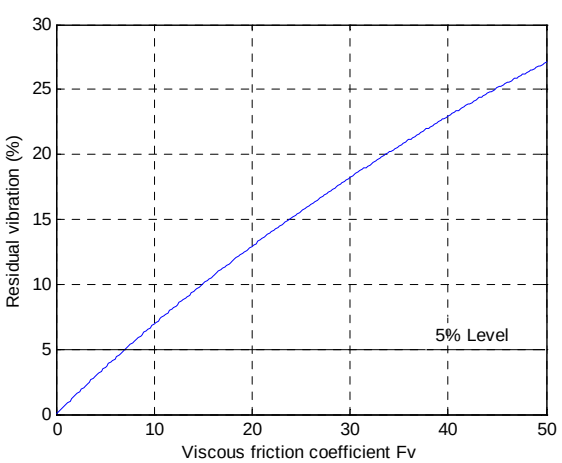

Figure 3.2 Residual vibration error versus viscous friction coefficient Fv (Fc=0).

Condition 2: If the viscous friction equals to zero while Coulomb friction still exists in the plant model (3.25), the step response of the plant with ZV shaper (3.22) shown in Figure 3.3 suffers from the steady state error. Figure 3.4 shows the relationship between the steady state error and the amplitude of Coulomb friction.

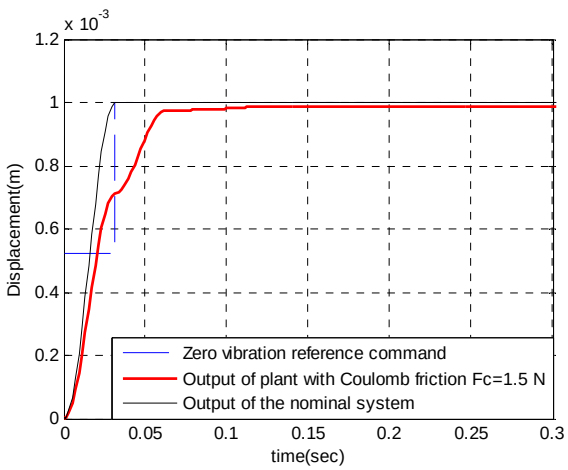

Figure 3.3 Simulated step response of the plant with ZV shaper ($r = 1 \times 10^{-3} m$, $F_c = 1.5N$, $F_v = 0Ns/m$)..

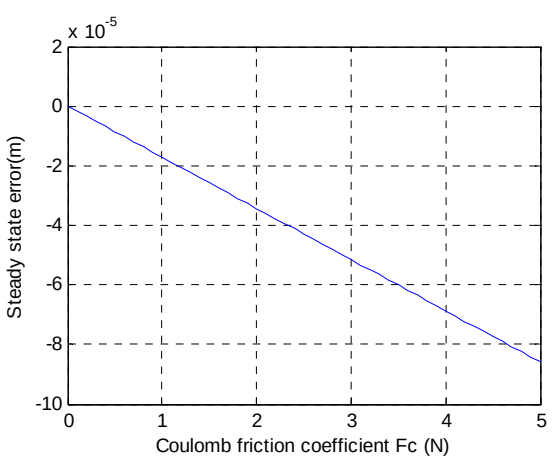

Figure 3.4 Coulomb friction coefficient Fc versus the steady state error ($r = 1 \times 10^{-3} m$, $F_c = 0 \sim 5N$, $F_v = 0Ns/m$)..

The sensitivity to the parameters of friction limits the application of ZV shaper. Although the ZV shaper can be modified to minimize the residual vibration of the plant

with friction (Hekman et al. 2004), the parameters of the friction model must be known. However the friction may change with the operation condition and time which has been confirmed in the experiments of the ultra-high precision positioning system presented in this work. Moreover, some adaptive algorithms can be utilized to estimate the parameters of the friction online. The drawback is those methods are sensitive to the accuracy of the friction. Therefore, a more robust controller which is able to supply desired nominal dynamics to the feedforward controller will be helpful. The model reference controller can make the plant behave like the reference model. Based on the idea of model reference control, the feedforward controller such as ZV shapers can be designed according to the transfer function of the reference model, if the behavior of the plant approaches the one of reference model in the model reference feedback loop. Combing ZV shaper with model reference control is the key idea of control design presented in this work.

3.3 Model Reference Control

In this section, the structure and design principle of the presented model reference control strategy are presented. Figure 3.5 shows a block diagram of a generic linear model reference control system (MRC).

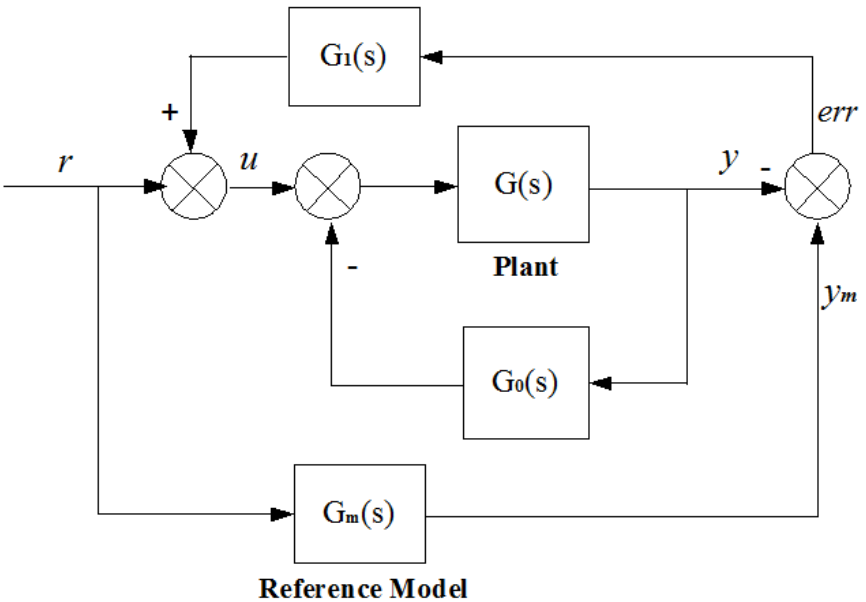

Figure 3.5 Block diagram of the linear model reference control.

The basic closed-loop feedback controller $G_0(s)$ is designed to stabilize the plant G(s). The transfer function of this basic feedback loop is shown in equation (3.29).

$$\frac{Y(s)}{U(s)} = \frac{G(s)}{1+G(s)G_0(s)} \tag{3.29}$$

With the controller $G_0(s)$ designed according to the nominal plant with fixed structures and parameters, the system $\frac{Y(s)}{U(s)}$ can obtain desired characteristics, such as stability, speed and accuracy of the response, and rejection of the disturbances. However, those performances may suffer from dependence on uncertainties, which are hard to model and even can not be modeled accurately. To further compensate the uncertainties, a reference model $G_m(s)$, which includes the linear part of the basic closed loop system

$\frac{Y(s)}{U(s)}$ with nominal parameters, is presented to let the plant follow the desired dynamic behavior.

The model reference controller $G_1(s)$ is used to force the plant output y to follow the trajectory of the reference model output y_m. Different from the previous model reference adaptive control (Senjyu et al. in 2002), $G_1(s)$ has a fixed structure and parameters which make it easy to implement in real time control (requires less memory and calculation time). The transfer function of the model reference control is represented in equation (3.30).

$$\frac{Y(s)}{R(s)} = \frac{\left[1 + G_1(s)G_m(s)\right]G(s)}{1 + G(s)G_0(s) + G_1(s)G(s)} \tag{3.30}$$

in which $R(s)$ represents the reference command. For Equation (3.30), the error between the model reference output y_m and the plant output y can be expressed as:

$$\begin{aligned} \frac{ERR(s)}{R(s)} &= \frac{Y_m(s) - Y(s)}{R(s)} \\ &= \frac{-G(s) + G_m(s) + G(s)G_0(s)G_m(s)}{1 + G(s)G_0(s) + G(s)G_1(s)} \end{aligned} \tag{3.31}$$

If the transfer function of basic feedback loop, the model reference controller, and the nominal model are redefined respectively as,

$$G_2(s) = \frac{G(s)}{1 + G(s)G_0(s)} = \frac{N_2(s)}{D_2(s)} \tag{3.32}$$

$$G_m(s) = \frac{N_m(s)}{D_m(s)} \tag{3.33}$$

$$G_1(s) = \frac{N_1(s)}{D_1(s)} \tag{3.34}$$

then Equation (3.30) can be rewritten as,

$$\frac{Y(s)}{R(s)} = \frac{G_2(s)\left[1 + G_1(s)G_m(s)\right]}{1 + G_1(s)G_2(s)} = \frac{N_2(s)\left(D_1(s)D_m(s) + N_1(s)N_m(s)\right)}{D_m(s)\left[D_1(s)D_2(s) + N_1(s)N_2(s)\right]} \tag{3.35}$$

Since the reference model and plant with feedback controller is stable, the stability of the system is determined by the model reference controller. Equation (3.35) implies that the system is stable by selecting a suitable structure of $G_1(s)$ that moves the poles of the transfer function in equation (3.35) to the left half of the s-plane.

Furthermore, for equation (3.35), if

$$\left|G_1(s)G_m(s)\right| >> 1 \tag{3.36}$$

and

$$\left|G_1(s)G_2(s)\right| >> 1 \tag{3.37}$$

Then the following approximation can be achieved,

$$1 + G_1(s)G_m(s) \approx G_1(s)G_m(s) \tag{3.38}$$

$$1 + G_1(s)G_2(s) \approx G_1(s)G_2(s) \tag{3.39}$$

Insert equation (3.38) and (3.39) into equation (3.35), the approximated transfer function of the plant with model reference control is,

$$\begin{aligned} \frac{Y(s)}{R(s)} &\approx \frac{G_2(s)G_1(s)G_m(s)}{G_1(s)G_2(s)} \\ &= G_m(s) \end{aligned} \tag{3.40}$$

The plant follows the dynamics of reference model almost perfectly. When conditions (3.36) and (3.37) are satisfied within the interested bandwidth, the system (3.30) behaves like the reference model.

If the plant behaves like the desired reference model, the feedforward controller can be designed according to the reference model G_m(s) to obtain fast and accurate response on ultra-high precision system. The robustness of the feedforward control is improved accordingly.

To further study the effectiveness of MRC on system with nonlinearities and uncertainties, the MRC is applied on a second-order plant with the nonlinearity of friction (3.25) presented in section 3.2, which occurs in almost all the mechanical systems in industry applications. Reference model is defined as the linear part of plant (3.25).

$$\begin{aligned} \frac{dy_m}{dt} &= v_m \\ \frac{dv_m}{dt} &= -2\zeta_m \omega_m v_m - \omega_m^2 y_m + \omega_m^2 r \cdot H(t) \end{aligned} \tag{3.41}$$

where y_m is the displacement of the second-order reference model; v_m is the velocity of the reference model; r is the amplitude of the step reference command; ζ_m represents the nominal damping ratio; and ω_m represents the nominal natural frequency. The model reference controller is designed based on the displacement error and velocity error between the reference model and the plant with Coulomb friction (3.25). The control command u in Figure 3.5 is described in the following form,

$$u(t) = r \cdot H(t) + k_{mp}\left(y_m - y\right) \tag{3.42}$$

in which k_{mp} is the proportional gain of the displacement error. The block diagram of the second-order system with viscous and coulomb friction controlled by the model reference controllers is shown in Figure 3.6.

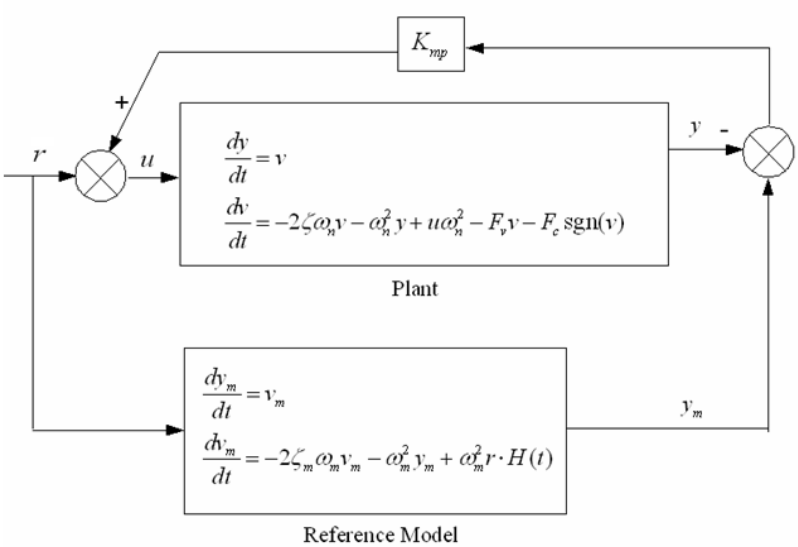

Figure 3.6 Block diagram of the model reference control toward the system with friction.

The positioning system (3.25) with MRC (3.42) is represented by equation (3.43):

$$\begin{aligned} \frac{dy}{dt} &= v \\ \frac{dv}{dt} &= -\left(2\zeta\omega_n + F_v\right)v - \left(1+k_{mp}\right)\omega_n^2 y + \omega_n^2 r \cdot H(t) - F_c \operatorname{sgn}\left(v\right) + k_{mp}\omega_n^2 y_m(t) \end{aligned} \tag{3.43}$$

Equation (3.43) implies that Coulomb friction can be viewed as a disturbance on the control force. Classical Zero Vibration input shapers discussed in section 3.2 are not designed to compensate for such disturbances. If the Zero Vibration input shaped staircase command is achieved from equation (3.19) ~ (3.21), the system would not settle at the desired final set point and there may be some residual vibration. This work primarily discusses the stability issue of the system with MRC control in the presence of model mismatch and parameter perturbations especially nonlinear perturbations, such as Coulomb friction in model (3.43).

Theorem 3.1: In the model reference control system, assume that

(1) The reference model in equation (3.41) is a stable under-damped second order system;

(2) The model of the plant (3.44) is a stable under-damped second order system with Coulomb friction. The damping ratio and natural frequency are exactly the same as the ones of reference model (3.41):

$$\begin{aligned} \frac{dy}{dt} &= v \\ \frac{dv}{dt} &= -2\zeta_m\omega_m v - \omega_m^2 y + u\omega_m^2 - F_c \operatorname{sgn}(v) \end{aligned} \tag{3.44}$$

(3) The model reference control strategy is defined as equation (3.42).

(4) Both the initial position and velocity equal to zero: $y(0) = 0, \quad v(0) = 0;$

And defining that

(1) $\{\overline{t}_i\}$ is the set of time instances when the speed of the positioning system (3.44) equals to zero:

$$\overline{t}_i \in T, \quad T = \{t : v(t) = 0\}, \qquad i = 0,1,2,... \tag{3.45}$$

(2) The error between the response of the plant with Coulomb friction uncertainty (3.44) and the response of the reference model (3.41), and the speed of the error are defined in equations (3.46) and (3.47) respectively:

$$e_y(t) = y_m(t) - y(t) \tag{3.46}$$

$$e_v(t) = v_m(t) - v(t) \tag{3.47}$$

The step response of the model reference controller on the plant with Coulomb friction is obtained in Equation (3.48).

$$\begin{aligned} y(t) = r & \left[1 - \frac{e^{-\zeta_m \omega_m t}}{\sqrt{1-\zeta_m^2}} \sin\left(\omega_m \sqrt{1-\zeta_m^2}\, t + \mathrm{tg}^{-1} \frac{\sqrt{1-\zeta_m^2}}{\zeta_m} \right) \right] \\ & - Amp_{err}(i) e^{-\zeta_m \omega_m (t-\overline{t}_i)} \sin\left[\omega_m \sqrt{1+k_{mp}-\zeta_m^2}\,(t-\overline{t}_i) + \theta(i) \right] \\ & - \frac{F_c \,\mathrm{sgn}(\overline{t}_i)}{(1+k_{mp})\omega_m^2} H(t-\overline{t}_i), \qquad t \in [\overline{t}_i, \overline{t}_{i+1}), \quad i = 0,1,2,... \end{aligned} \tag{3.48}$$

in which

$$Amp_{err}(i) = -\sqrt{\frac{F_c^2 + 2\zeta_m \omega_m F_c \operatorname{sgn}(t_i) v_{err}\left(\bar{t}_i^-\right) + 2F_c \operatorname{sgn}(\bar{t}_i)\left(1+k_{mp}\right)\omega_m^2 err\left(\bar{t}_i^-\right)}{\left(1+k_{mp}\right)\omega_m^4\left(1+k_{mp}-\zeta_m^2\right)} + err^2\left(\bar{t}_i^-\right) + \frac{\left[err\left(\bar{t}_i^-\right)\zeta_m\omega_m + v_{err}\left(\bar{t}_i^-\right)\right]^2}{\omega_m^2\left(1+k_{mp}-\zeta_m^2\right)}} \tag{3.49}$$

$$\theta(i) = tg^{-1}\left\{\frac{err\left(\bar{t}_i^-\right) + \frac{F_c \operatorname{sgn}(\bar{t}_i)}{\left(1+k_{mp}\right)\omega_m^2}}{\frac{err\left(\bar{t}_i^-\right)\zeta_m\omega_m + v_{err}\left(\bar{t}_i^-\right)}{\omega_m\sqrt{1+k_{mp}-\zeta_m^2}} + \frac{\zeta_m F_c \operatorname{sgn}(\bar{t}_i)}{\left(1+k_{mp}\right)\omega_m^2\sqrt{1+k_{mp}-\zeta_m^2}}}\right\} \tag{3.50}$$

Then the step response error between the reference model and plant with Coulomb friction is

$$e_y(t-\bar{t}_i) = Amp_{err}(i)e^{-\zeta_m\omega_m\left(t-\bar{t}_i\right)}\sin\left[\omega_m\sqrt{1+k_{mp}-\zeta_m^2}\left(t-\bar{t}_i\right)+\theta(i)\right] + \frac{F_c \operatorname{sgn}(\bar{t}_i)}{\left(1+k_{mp}\right)\omega_m^2}H(t-\bar{t}_i), \quad t\in\left[\bar{t}_i,\bar{t}_{i+1}\right), \quad i=0,1,2,... \tag{3.51}$$

Proof: Detailed proof is given in Appendix A.

As a verification, data from equation (3.51) and simulation are plotted in Figure 3.7 which indicates a relatively good match.

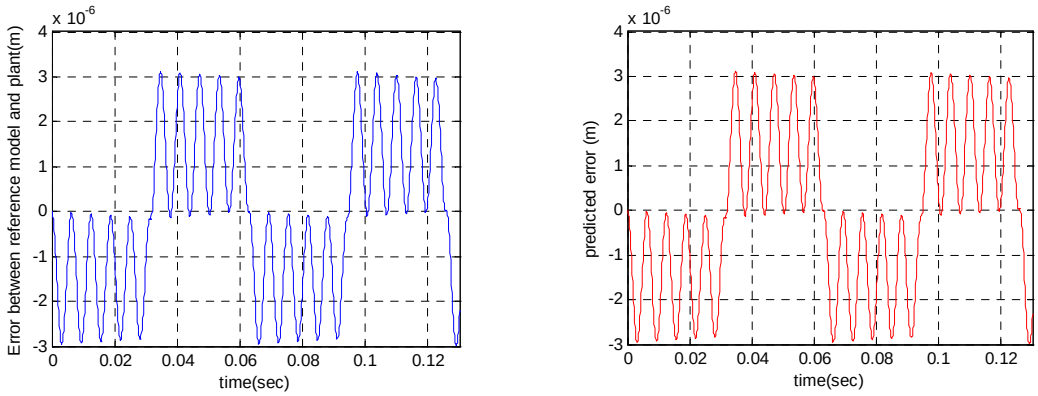

(a) Simulated error between the reference model response and the plant output;

(b) Predicted error $e_y(t)$ according to Equation (3.51).

Figure 3.7 Error between the reference model response and the plant output ($f = 1.5\,\mathrm{sgn}(v)$, $r = 1\times10^{-3} m$).

Theorem 3.2: Given the stable plant (3.44), MRC plant (3.41) and control (3.42) with one more assumption that the damping ratio ζ_m equals to zero. If the model reference controller gain k_{mp} satisfy the following constraint in Equation (3.52):

$$k_{mp} = 4n^2 - 1 >> \frac{F_c^2}{\omega_m^4 r^2} - 1, \quad n = 1, 2, 3... \tag{3.52}$$

Then for any given small real number ε > 0, there exists a positive integer $n_0 = \frac{1}{\omega_m}\sqrt{\frac{2F_c}{\varepsilon}}$ such that for all $n > n_0$, $|e_y| < \varepsilon$. The absolute value of the error between the response of the plant and reference model can reach any given small value by choosing appropriate model reference controller gain k_{mp}:

$$\lim_{n\to\infty} |e_y| = 0 \tag{3.53}$$

Proof: According to the assumption of the theorem, the reference model is an un-damped second order system. The step response of the reference model is

$$v_m(t) = \omega_m r \sin \omega_m t \tag{3.54}$$

With the errors defined in Equation (3.46) and (3.47), the dynamic behavior of the error between the reference model and the plant with uncertain friction parameter values is described in Equation (3.55).

$$\begin{aligned} \frac{de_y}{dt} &= e_v \\ \frac{de_v}{dt} &= -\omega_m^2 \left(1 + k_{mp}\right) e_y - F_c \operatorname{sgn}\left[e_v(t) + v_m(t)\right] \end{aligned} \tag{3.55}$$

Without the loss of generality, it is assumed that the amplitude of the reference command r is positive, thus $e_v(0^+) > -v_m(0^+)$. Figure 3.8 shows the corresponding phase diagram plotted as e_v against $\bar{e}_y$ to give circular paths in Equation (3.56).

$$e_v^2 + \left(\bar{e}_y + \frac{F_c}{\omega_m \sqrt{1 + k_{mp}}} \right)^2 = \bar{C} \tag{3.56}$$

$$\bar{e}_y = \omega_m \sqrt{1 + k_{mp}}\, e_y \tag{3.57}$$

In Equation (3.56), $\bar{C}$ is a constant.

Similarly, when $e_v(t) < -v_m(t)$, The phase plane diagram is a family of ellipses with the center at $\left(\frac{F_c}{\omega_m \sqrt{1 + k_{mp}}}, 0 \right)$ show in Figure 3.9 and Equation (3.58).

$$e_v^2 + \left(\bar{e}_y - \frac{F_c}{\omega_m \sqrt{1 + k_{mp}}} \right)^2 = \bar{C} \tag{3.58}$$

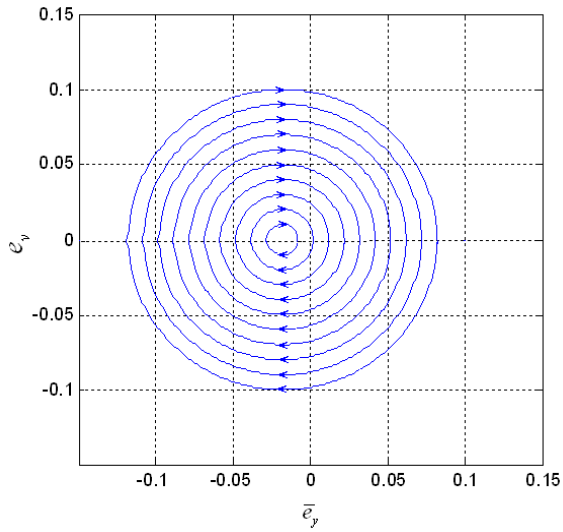

Figure 3.8 Phase diagram of error oscillator in Equation (3.57) ($e_v(t) \geq -v_m(t)$).

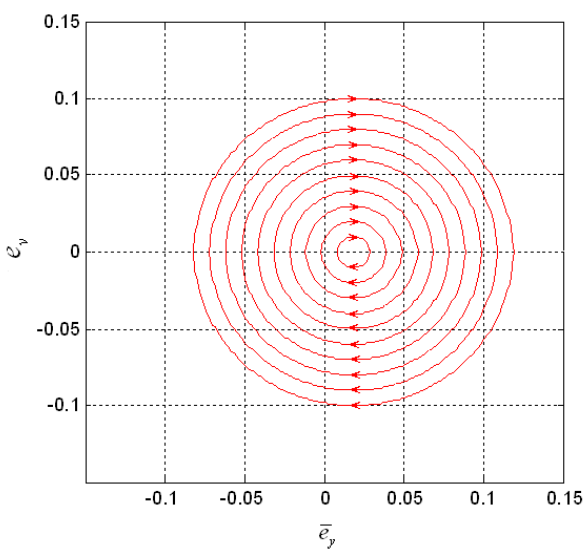

Figure 3.9 Phase diagram of oscillator in Equation (3.60) ($e_v(t) < -v_m(t)$).

Detailed derivation of phase diagram is described in Appendix B. The phase plane diagram of the plant with Coulomb friction and model reference controller switches between Figure 3.8 and Figure 3.9. The switching behavior depends on the sign of $e_v(t) + v_m(t)$ in Equation (3.55). Two constraints on the oscillatory behavior of the error

velocity $e_v(t)$ in Equation (3.51) have been made to simplify the proof. These constraints have been summarized in Equation (3.52):

(1) Frequency constraint: The oscillatory frequency of the error velocity $e_v(t)$ in Equation (3.51) is 2n times of the oscillatory frequency of $v_m(t)$ in Equation (3.54), i.e., $2n = \sqrt{1+k_{mp}}$, where n is positive integer;

(2) Amplitude constraint: The oscillatory amplitude of the error velocity $e_v(t)$ is much smaller than the amplitude of $v_m(t)$, i.e., $\frac{F_c}{\omega_m \sqrt{1+k_{mp}}} << \omega_m r$.

The above constraints could be summarized in Equation (3.52). Figure 3.10 shows a possible curve of velocity error which satisfy the above two assumptions compared to the velocity of the reference model.

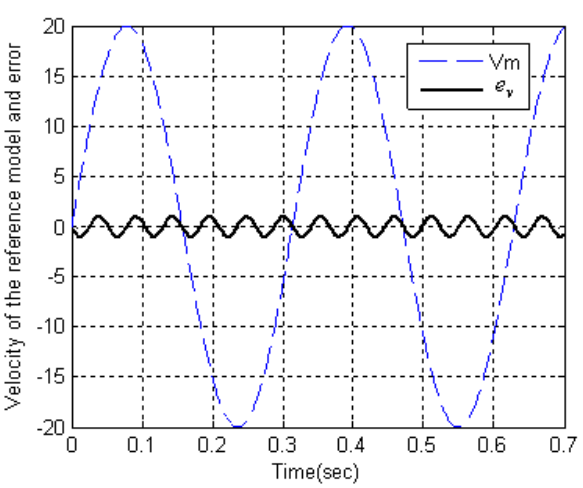

Figure 3.10 Velocity of error $e_v(t)$ compared to velocity of the reference model $v_m(t)$.

For the differential equation (3.55) with zero initial conditions, the phase curve is shown in Figure 3.11 in thick black. The phase plane diagram follows Equation (3.59). k is a nonnegative integer.

$$e_v^2(t)=\begin{cases}\dfrac{F_c^2}{\omega_m^2\left(1+k_{mp}\right)}-\left(\overline{e}_y(t)+\dfrac{F_c}{\omega_m\sqrt{1+k_{mp}}}\right)^2, & t\in\left[\dfrac{2k\pi}{\omega_m},\ \dfrac{(2k+1)\pi}{\omega_m}\right)\\ \dfrac{F_c^2}{\omega_m^2\left(1+k_{mp}\right)}-\left(\overline{e}_y(t)-\dfrac{F_c}{\omega_m\sqrt{1+k_{mp}}}\right)^2, & t\in\left[\dfrac{(2k+1)\pi}{\omega_m},\ \dfrac{2(k+1)\pi}{\omega_m}\right)\end{cases} \tag{3.59}$$

The absolute value of the error is limited in Equation (3.60).

$$0\le\left|\overline{e}_y(t)\right|\le\frac{2F_c}{\omega_m n} \tag{3.60}$$

Combining Equation (3.57) and (3.60) gets

$$\lim_{n\to\infty}0\le\lim_{n\to\infty}\left|e_y(t)\right|\le\lim_{n\to\infty}\frac{2F_c}{\omega_m^2 n^2} \tag{3.61}$$

Since

$$\lim_{n\to\infty}\frac{2F_c}{\omega_m^2 n^2}=0 \tag{3.62}$$

the response of the plant with Coulomb friction approaches the behavior of the reference model when *n* goes to infinity, as expressed in Equation (3.53), where *n* depends on the model reference control gain k_{mp} which satisfy constraints in Equation (3.52). The proof is completed on observing the convergence of the trajectories towards the origin as n goes to infinity (proof end).

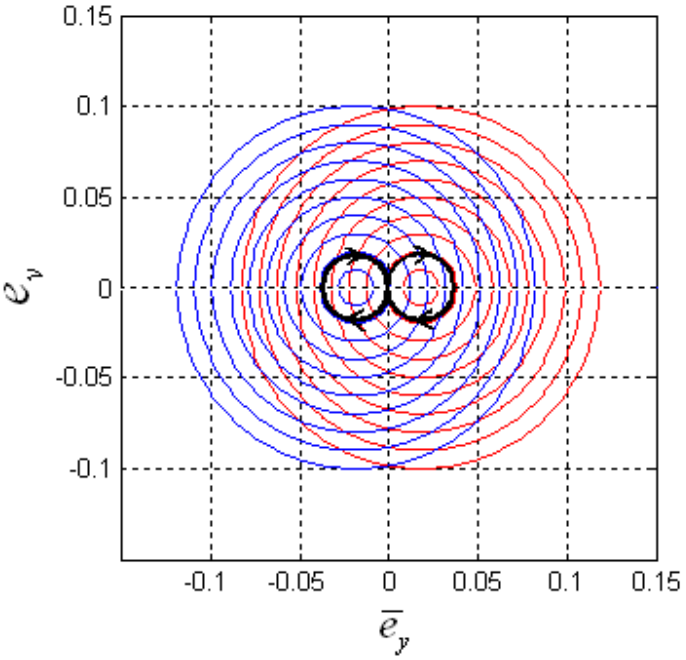

Figure 3.11 Phase diagram of oscillator in Equation (3.57).

Theorem 3.3: Given the stable plant (3.44), MRC plant (3.41) and control (3.42). If the model reference controller gain k_{mp} satisfy constraint in Equation (3.63),

$$k_{mp} = \left(4n^2 - 1\right)\left(1-\zeta^2\right) >> \left(\frac{F_c^2}{\omega_m^4 r^2} - 1\right)\left(1-\zeta^2\right) \tag{3.63}$$

n is a positive integer. Then for any given small real number ε > 0, there exists a positive integer $n_0 = \frac{1}{2\omega_m}\sqrt{\frac{3F_c - \zeta^2\omega_m^2\varepsilon}{\varepsilon\left(1-\zeta^2\right)}}$ such that for all $n > n_0$, $\left|e_y\right| < \varepsilon$ .The error between the response of the plant and reference model can reach any given small value by choosing appropriate model reference controller gain k_{mp}: $\lim_{n\to\infty}\left|e_y(t)\right| = 0$.

Proof: The proof is similar to that of Theorem 3.2. The step response of the reference model is

$$v_m(t) = \frac{\omega_m r}{\sqrt{1-\zeta^2}} e^{-\zeta\omega_m t} \sin\left(\omega_m \sqrt{1-\zeta^2}\, t\right) \tag{3.64}$$

The dynamic behavior of the error is described by Equation (3.65).

$$\begin{aligned} \frac{de_y}{dt} &= e_v \\ \frac{de_v}{dt} &= -2\zeta\omega_m e_v - \omega_m^2 \left(1 + k_{mp}\right) e_y - F_c \operatorname{sgn}\left[e_v(t) + v_m(t)\right] \end{aligned} \tag{3.65}$$

If $e_v(t) \geq -v_m(t)$, the phase plane diagram is shown in Figure 3.12; while if $e_v(t) < -v_m(t)$, the phase plane diagram is shown in Figure 3.13. It is assumed that the amplitude of the reference command r is positive, thus $e_v(0^+) > -v_m(0^+)$. The velocity of the error is in Equation (3.66) before the sign changes.

$$e_v(t) = -\frac{F_c}{\omega_m \sqrt{1 + k_{mp} - \zeta^2}} e^{-\zeta\omega_m t} \sin\left(\omega_m \sqrt{1 + k_{mp} - \zeta^2}\, t\right) \tag{3.66}$$

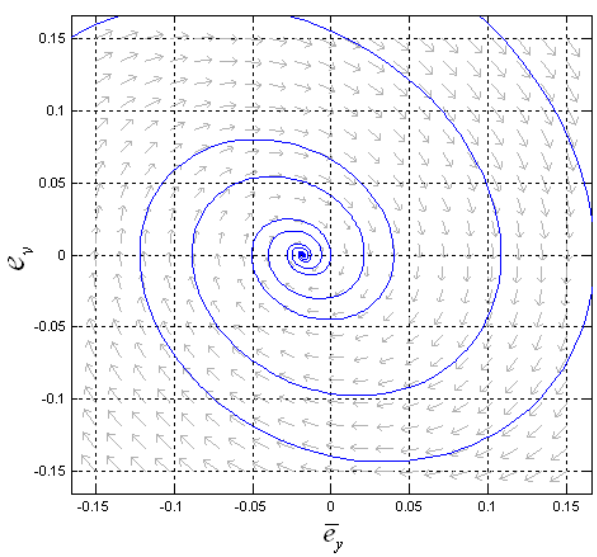

Figure 3.12 Phase diagram of oscillator in Equation (3.65) ($e_v(t) > -v_m(t)$).

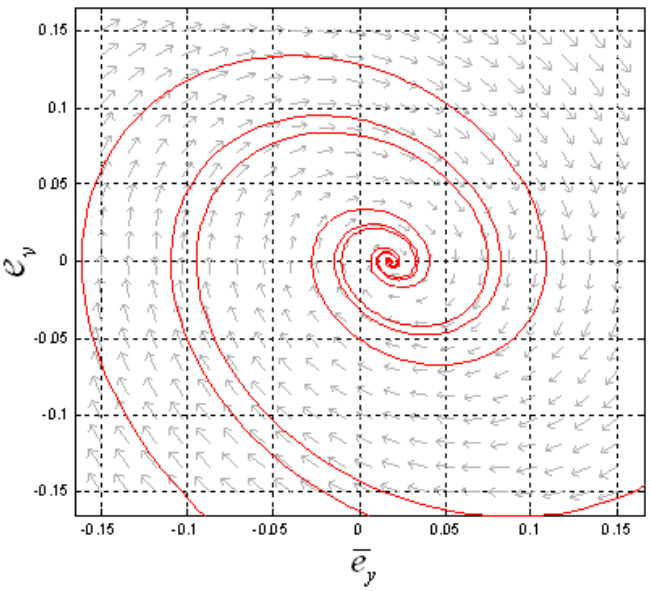

Figure 3.13 Phase diagram of oscillator in Equation (3.65) ($e_v(t) < -v_m(t)$).

The phase plane diagram of the plant with Coulomb friction and model reference controller switches between Figure 3.12 and Figure 3.13 depending on the sign of $e_v(t)+v_m(t)$. Similar to Theorem 3.2, the following assumptions summarized in Equation (3.63) are made:

(1) Frequency constraint: The oscillatory frequency of the error velocity $e_v(t)$ in Equation (3.51) is 2n times of the oscillatory frequency of $v_m(t)$ in Equation (3.64) in Equation (3.54), i.e., $n = \frac{1}{2}\sqrt{\frac{1+k_{mp}-\zeta^2}{1-\zeta^2}}$, where n is positive integer;

(2) Amplitude constraint: The oscillatory amplitude of the error velocity $e_v(t)$ is much smaller than the amplitude of $v_m(t)$, i.e., $\frac{F_c}{\omega_m\sqrt{1+k_{mp}-\zeta^2}} << \frac{\omega_m r}{\sqrt{1-\zeta^2}}$

The above two assumptions are summarized in Equation (3.63). If $t \in \left[\frac{2k\pi}{\omega_m \sqrt{1-\zeta^2}}, \frac{(2k+1)\pi}{\omega_m \sqrt{1-\zeta^2}} \right)$, the phase plane diagram follows Figure 3.12; if $t \in \left[\frac{(2k+1)\pi}{\omega_m \sqrt{1-\zeta^2}}, \frac{2(k+1)\pi}{\omega_m \sqrt{1-\zeta^2}} \right)$, the phase plane diagram follows Figure 3.13. For the differential equation (3.65) with zero initial conditions, the phase plane curve crosses the $\overline{e}_y(t)$ axis and switches between Figures 3.12 and Figure 3.13 at time instant sequence $\{t_k\}$.

$$t_k = \frac{(2k+1)\pi}{\omega_m \sqrt{1-\zeta^2}}, \quad k \geq 0, \text{ and } k \text{ is an integer.} \tag{3.67}$$

The phase curve is shown in Figure 3.14 in black.

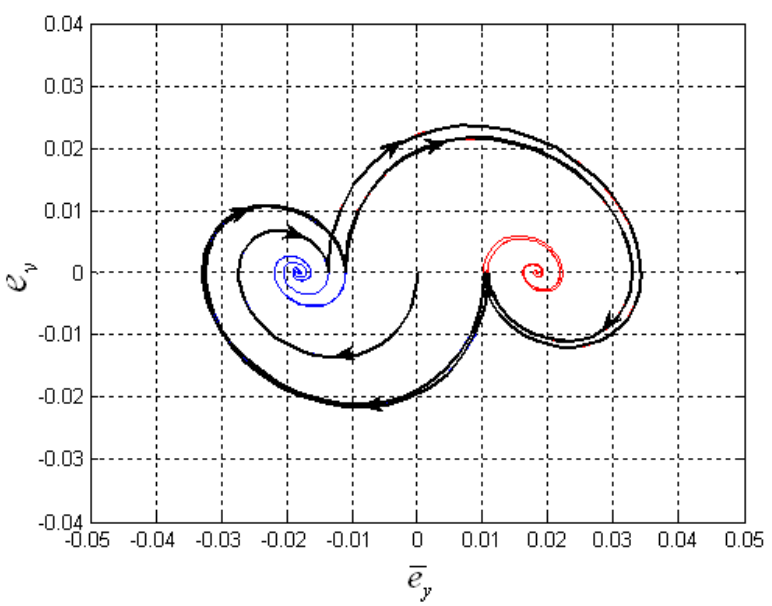

Figure 3.14 Phase diagram of oscillator in Equation (3.65).

Since $e_y(t_k) \in \left[-\frac{F_c}{\omega_m^2\left(1+k_{mp}\right)}, \frac{F_c}{\omega_m^2\left(1+k_{mp}\right)} \right]$, the maximum amplitude of the error is achieved when meeting any of the following two conditions is met as show in Figure 15.

$$\begin{cases} \dfrac{de_y}{dt} = e_v \\ \dfrac{de_v}{dt} = -2\zeta\omega_m e_v - \omega_m^2\left(1+k_{mp}\right)e_y - F_c \\ e_y(0) = \dfrac{F_c}{\omega_m^2\left(1+k_{mp}\right)}, \quad e_v(0) = 0 \end{cases} \tag{3.68}$$

$$\begin{cases} \dfrac{de_y}{dt} = e_v \\ \dfrac{de_v}{dt} = -2\zeta\omega_m e_v - \omega_m^2\left(1+k_{mp}\right)e_y + F_c \\ e_y(0) = -\dfrac{F_c}{\omega_m^2\left(1+k_{mp}\right)}, \quad e_v(0) = 0 \end{cases} \tag{3.69}$$

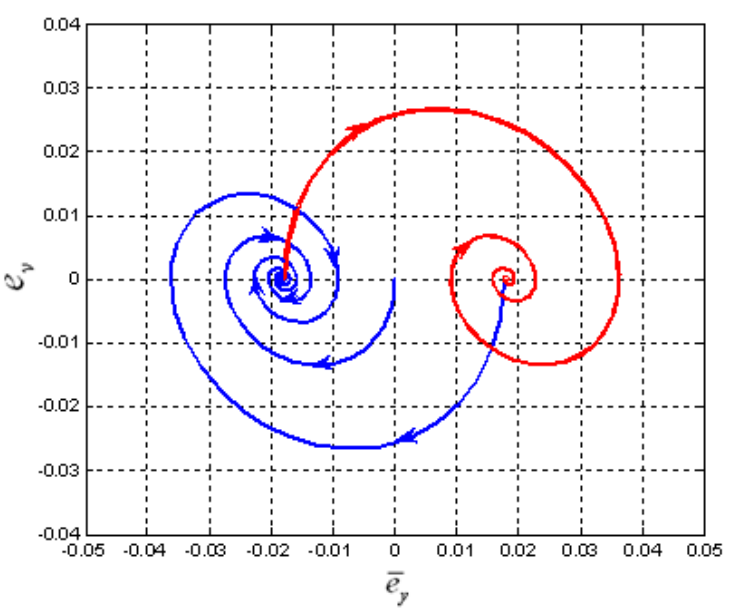

Figure 3.15 Phase diagram of oscillator in Equation (3.68) and (3.69).

The error between the reference model and the plant with Coulomb friction is limited in Equation (3.70).

$$0 \le \left|e_y(t)\right| \le \frac{F_c\left(2e^{-\frac{\zeta\pi}{\sqrt{1+k_{mp}-\zeta^2}}}+1\right)}{\omega_m^2\left(1+k_{mp}\right)} < \frac{3F_c}{\omega_m^2\left(1+k_{mp}\right)} \tag{3.70}$$

$$\lim_{n\to\infty} 0 \le \lim_{n\to\infty}\left|e_y(t)\right| \le \lim_{n\to\infty}\frac{3F_c}{\omega_m^2\left(1+k_{mp}\right)} \tag{3.71}$$

Insert Equation (3.63) into Equation (3.71),

$$\frac{3F_c}{\omega_m^2\left(1+k_{mp}\right)} = \frac{3F_c}{\omega_m^2\left[4\left(1-\zeta^2\right)n^2+\zeta^2\right]} \tag{3.72}$$

Since $\lim_{n\to\infty}\frac{3F_c}{\omega_m^2\left[4\left(1-\zeta^2\right)n^2+\zeta^2\right]} = 0$ and $\lim_{n\to\infty} 0 = 0$, the response of the plant with Coulomb friction approaches the behavior of the reference model when *n* goes to infinity, i.e. $\lim_{n\to\infty}\left|e_y(t)\right| = 0$, where *n* depends on the model reference control gain k_{mp} which satisfy constraints in Equation (3.63). For any given small real number ε > 0, if $\left|e_y\right| < \varepsilon$, n must satisfy Equation (3.73):

$$\frac{3F_c}{\omega_m^2\left[4\left(1-\zeta^2\right)n^2+\zeta^2\right]} < \varepsilon \tag{3.73}$$

Thus if $n > \frac{1}{2\omega_m}\sqrt{\frac{3F_c-\zeta^2\omega_m^2\varepsilon}{\varepsilon\left(1-\zeta^2\right)}}$, $\left|e_y\right| < \varepsilon$. (proof end).

Theorem 3.4 implies that dynamics of the plant with Coulomb friction can track the ones of reference model if appropriate model reference control gain is chosen. Figure

3.16 indicates the simulated results of MRC on the plant (3.44) with various model reference gain k_{mp}.

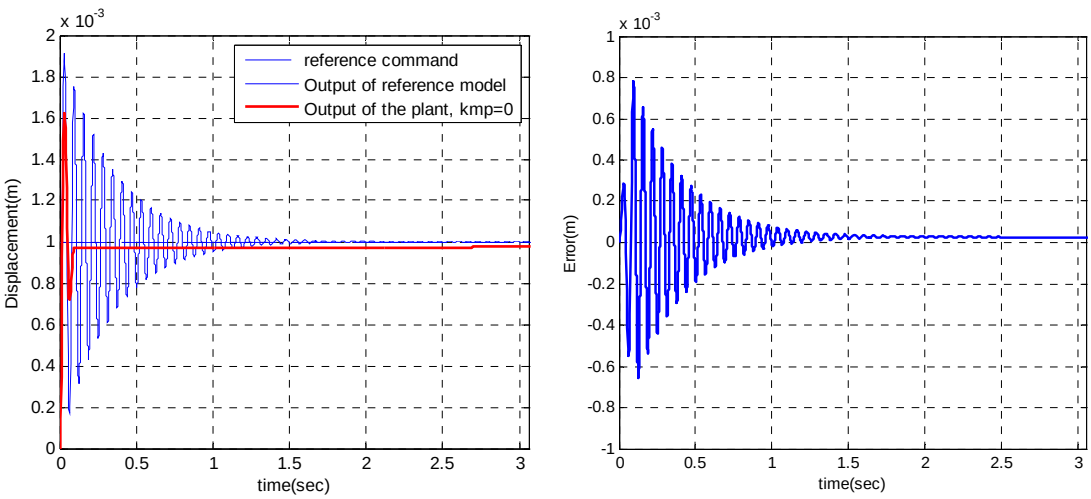

(a) Step response of the plant with Coulomb friction;

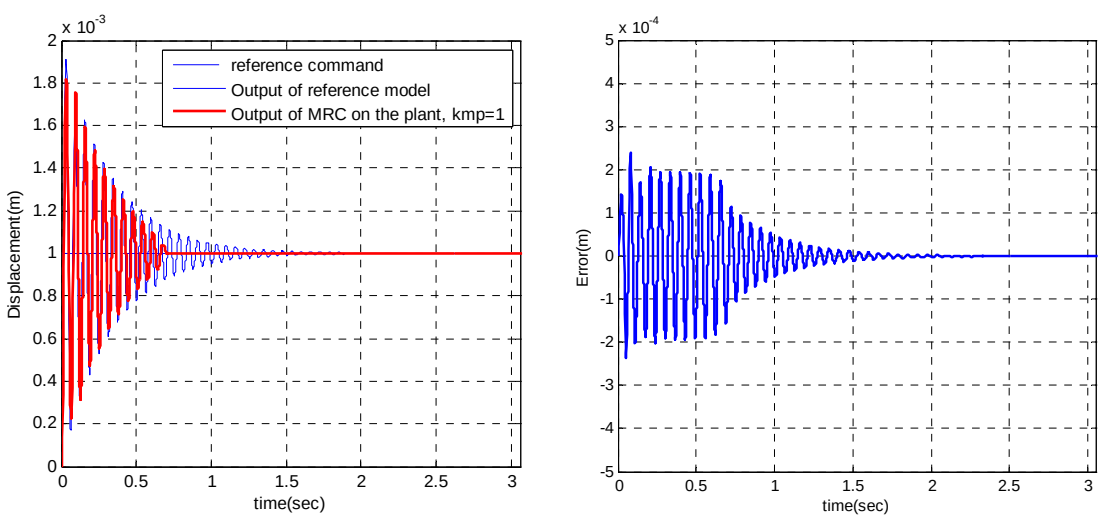

(b) Step response of MRC on plant with $k_{mp} = 1$;

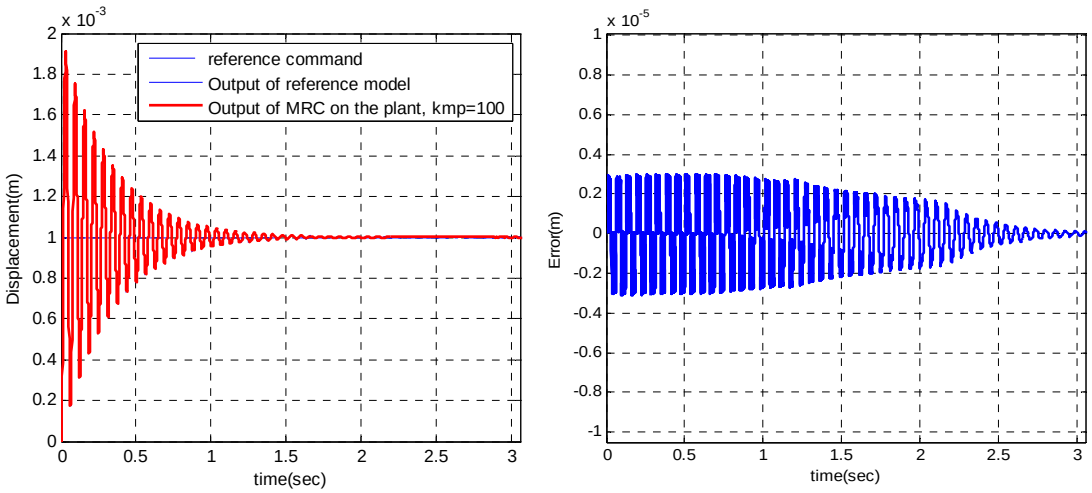

(c) Step response of MRC on plant with $k_{mp} = 100$;

Figure 3.16 Step response of model reference control on plant wit h friction ($f = 1.5\,\mathrm{sgn}(v)$ $r = 1\times10^{-3} m$).

Define $\left|e_y(t)\right|_2$ as the l^2-norm of the error between the plant response and the reference model response. Figure 3.17 shows the effects of increasing the MRC gain on the l^2-norm this error which decreases monotonically as the MRC gain goes to infinity.

$$\left|e_y(t)\right|_2 = \sqrt{\int_0^\infty \left|y(t) - y_m(t)\right|^2 dt} \tag{3.74}$$

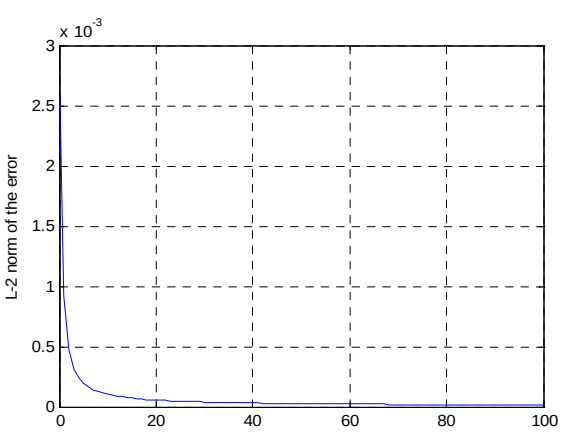

Figure 3.17 l^2-norm of the error with various model reference controller gain k_{mp}.

3.4 Variable Model Reference Zero Vibration Control

ZV shaper offers fast response and low vibration at the nominal working condition in motion control. However, it is sensitive to parameter variation. If the plant with feedback controller has uncertainties such as friction, ZV feedforward controller can not achieve good performance. Theorem 3.2 in section 3.3 indicates that the model reference controller presented in Figure 3.5 is capable of compensating the effect of the Coulomb friction in a high precision positioning system. If the response of system tracks the one of ideal reference model with nominal parameters and no friction, the feedforward ZV shaper can be designed according to the reference model. This so called Model Reference Zero Vibration (MRZV) control is easy to implement and reduces the effect of friction significantly. The block diagram of Model Reference Zero Vibration (MRZV) Control method is proposed, as shown in Figure 3.18. The desired reference command is fed into a feedforward controller. The feedforward controller transforms the desired motion into a series of shaped command, which is represented by $\tilde{r}(t)$.

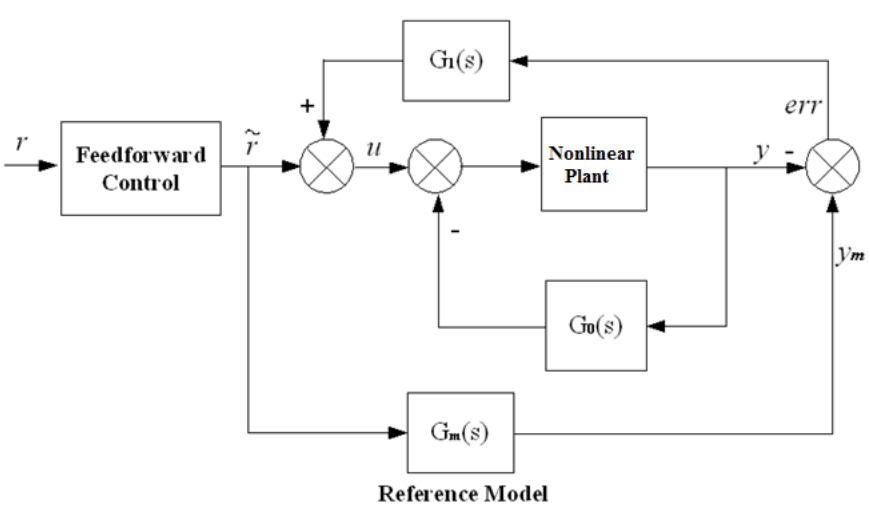

Figure 3.18 Block diagram of MRZV control.

The system with MRZV is represented in equation (3.75).

$$\begin{aligned}\frac{dy}{dt} &= v \\ \frac{dv}{dt} &= -\left(2\zeta\omega_n + F_v\right)v(t) - \left(1+k_{mp}\right)\omega_n^2 y(t) - F_c\,\mathrm{sgn}\left(v\right) + k_{mp}\omega_n^2 y_m(t) \\ &\quad + \omega_n^2 A_1 r \cdot H(t) + \omega_n^2 A_2 r \cdot H(t-t_2)\end{aligned} \tag{3.75}$$

Figures 3.19 and 3.20 verifies the effeteness of the proposed MRZV control method. The steady state error and residual vibration is reduced significantly compared with using ZV shaper only (Figure 3.2~3.4).

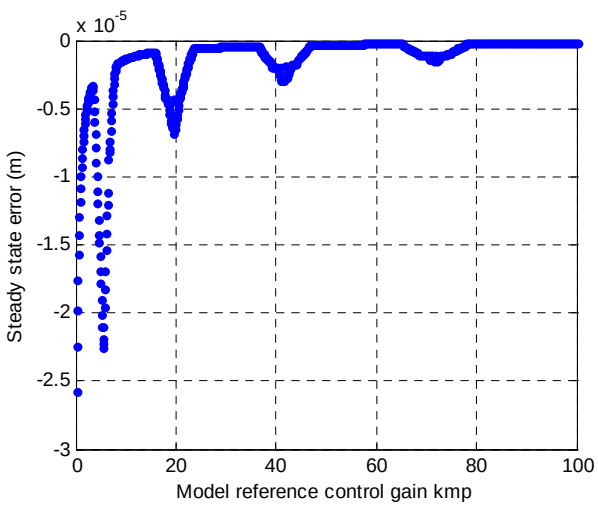

Figure 3.19 Model reference control gain k_{mp} versus steady state error of step response using MRZV $\left(r = 1\times10^{-3}m,\ F_c = 1.5N,\ F_v = 0Ns/m\right)$.

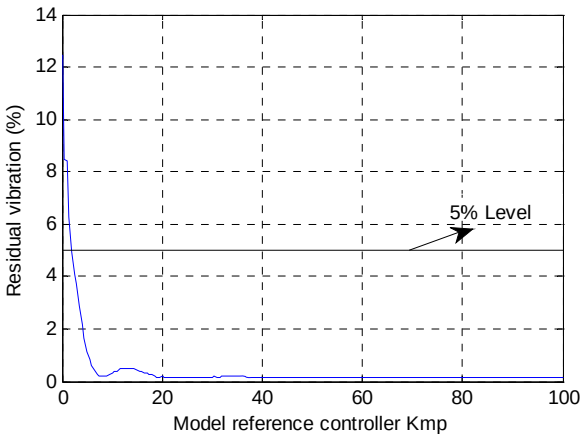

Figure 3.20 Model reference control gain k_{mp} versus vibration error of unit step response using MRZV $\left(r = 1\times10^{-3}m,\ F_c = 0N,\ F_v = 20Ns/m\right)$.

To further supress the transient characteristics of the ultra-high precision positioning systems, it is possible to vary the linear reference model whose properties and subsequent control design are well understood. The relative ZV shaper is designed based on the variable reference model. This control methodology is called Variable Zero Vibration Model Reference control (VMRZV). For example, the settling time of the system with MRZV (3.51) can be quantitatively adjusted by systematically varying the reference model to meet the requirement of fast and accurate positioning.

CHAPTER 4

MODELING AND CONTROL OF DUAL SOLENOID MICRO-POSITIONER

This chapter deals with the modeling and control design of the dual solenoid micro-positioner. A simplified mathematic model of a commercial single solenoid actuator is derived in section 4.1. Based on the model of single solenoid, the model of dual solenoid micro-positioner proposed in this work is presented in section 4.2. Several basic feed back control strategies are designed in section 4.3 to stabilize the micro-positioner. To improve the transient performance of the micro-positioner, the feedforward controllers associated with the actuator with the designed feedback controllers are presented in section 4.4. A more robust design, Model Reference Zero Vibration (MRZV) combining with Balance control is derived in section 4.5. Finally, Variable Model Reference Zero Vibration Balance (VMRZVB) control, which aims to achieve fast response, is introduced in section 4.6. The relative simulation results are also given.

4.1 Modeling of Single Solenoid Actuator

The cross section of a typical industrial push-pull solenoid is shown in Figure 4.1. When a voltage u is applied on the solenoid, the resulting current i flows through the coils wrapped around a metallic core, and a magnetic flux circuit is then generated through the core, the movable plunger and the air gap between them. The plunger that can be moved back and force in the center is used to provide a mechanical force to other mechanism.

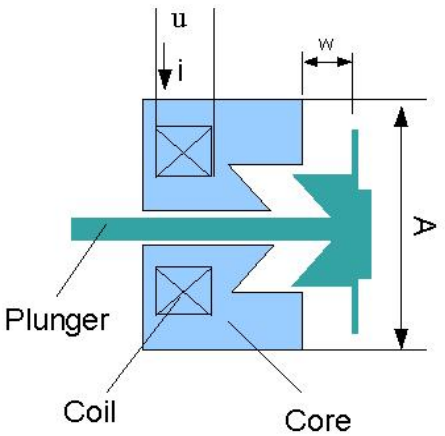

Figure 4.1 Cross section of single solenoid.

A typical solenoid comprises of electric, magnetic and mechanical subsystems, which are complicated to model and analyze. To build a control-based model of the dual solenoid actuator, some simplifications are necessary. Each solenoid has a resistive and inductive component. The voltage equation is given as (Y. Xu and B. Jones, 1997):

$$u = Ri + \frac{d\lambda}{dt} \tag{4.1}$$

In Equation (4.1), R is the resistance of the coils of the solenoid; λ is the flux linkage variable which depends on the current of the coil i and the air gap length w:

$$\lambda = \frac{\beta i}{w + d_0} \tag{4.2}$$

In which w is the air gap distance shown in Figure 4.1; and d_0 and β are constants depending on the material and geometry of the solenoid.

$$\beta = \mu_0 A \lambda_\phi^2 N^2 \tag{4.3}$$

$$d_0 = A\mu_0 \int \frac{1}{\tilde{A}(l)\tilde{\mu}(l)} dl \tag{4.4}$$

In equation (4.3), λ_ϕ is the flux leakage coefficient; *N* is the number of turns in the coil; μ_0 is the permeability in free space; and *A* is area of the gap. In equation (4.4), $\tilde{A}(l)$ and $\tilde{\mu}(l)$ are the area and permeability of the segment along the magnetic circuit. Combing (4.1) and (4.2) produces:

$$u = Ri + \frac{\beta}{d_0 + w} \cdot \frac{di}{dt} - \frac{i\beta}{(d_0 + w)^2} \cdot \frac{dw}{dt} \tag{4.5}$$

When the coil is energized, the density of the stored energy in the gap is given by (N. Mohan, 2003):

$$C = \frac{B^2}{2\mu_0} \tag{4.6}$$

In which *B* is the magnetic flux density that can be approximated as:

$$B = \frac{\lambda_\phi N i}{\frac{w}{\mu_0} + \int \frac{A}{\tilde{A}(l)\tilde{\mu}(l)} dl} \tag{4.7}$$

Because the air gap distance *w* is small, *B* can be assumed to be uniform and the energy stored in the gap *w* is given by (Q. Yuan in 2004):

$$e(w,i) = AwC \tag{4.8}$$

Insert equation (4.4), (4.6) and (4.7) into equation (4.8), the total energy is calculated as:

$$e(w,i) = \frac{\beta i^2 w}{2(w+d_0)^2} \tag{4.9}$$

When d_0 is very small compared to gap *w*, equation (4.9) can be simplified as

$$e(w,i) \approx \frac{\beta i^2}{2\left(w+d_0\right)} \tag{4.10}$$

The magnetic force *F* that tends to move the plunger in a direction that increases the inductance of the coils:

$$F = \frac{\partial e(w,i)}{\partial w} \tag{4.11}$$

Combining equation (4.10) and (4.11), the dynamic model of a single solenoid is

$$F = \frac{\beta i^2}{2(w+d_0)^2} \tag{4.12}$$

The simplified model of a single solenoid actuator can be represented by equation (4.5) and (4.12).

4.2 Modeling of Dual Solenoid Positioner

Single DC solenoid is able to generate a unidirectional force, which is only push or pull. In this work, two solenoids are connected together in opposite position to achieve "push-pull" force. To simplify the model, it is assumed that the two solenoids are identical. As shown in Figure 4.2, let *x* represent the displacement of the plunger of dual solenoid micro-positioner along *x* direction: *x* equals to zero when the movable plunger stays in the middle position; *x* increases when the plunger moves toward the Fotonic sensor; x decreases when it moves far away from the sensor. The total travel range of the plunger is limited between $-x_{max}$ (left end) and x_{max} (right end).

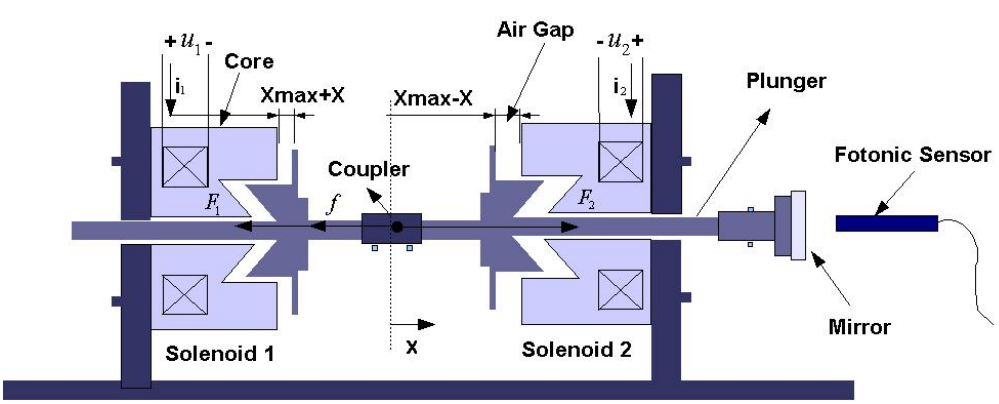

Figure 4.2 Cross section of dual solenoid actuator.

The air gap for solenoid 1 (left) and solenoid 2 (right) are:

$$w_1(t) = x_{\max} + x(t) \tag{4.13}$$

$$w_2(t) = x_{\max} - x(t) \tag{4.14}$$

The electrical equations can be expressed as,

$$u_1 = Ri_1 + \frac{\beta}{d+x} \cdot \frac{di_1}{dt} - \frac{i_1\beta}{(d+x)^2} \cdot \frac{dx}{dt} \tag{4.15}$$

$$u_2 = Ri_2 + \frac{\beta}{d-x} \cdot \frac{di_2}{dt} - \frac{i_2\beta}{(d-x)^2} \cdot \frac{dx}{dt} \tag{4.16}$$

For simplicity, the constant *d* is set as:

$$d = x_{\max} + d_0 \tag{4.17}$$

All the symbols with subscript 1 and 2 represent the corresponding terms of solenoid 1 and solenoid 2 respectively.

On the mechanical side, the dynamic equation of dual solenoid positioner can be expressed as

$$\frac{dv}{dt} = \frac{F_2 - F_1 - f}{m} \tag{4.18}$$

In (4.18), F_1 and F_2 are the magnetic forces produced by magnetic field of coils of solenoid 1 and 2 respectively; f is the total friction in the push-pull solenoid; *m* is the mass of the plunger. The model is built up under the assumption that the friction is

adequately modeled as classical Coulomb friction plus viscous friction. The dynamic equation of the dual solenoid is given by:

$$\frac{dv}{dt} = \frac{\beta i_1^2}{2m(d-x)^2} - \frac{\beta i_2^2}{2m(d+x)^2} - (F_v v + F_c \operatorname{sgn}(v)) \tag{4.19}$$

Thus the nonlinear state space model of dual solenoid is derived as:

$$\begin{aligned}
\frac{dx}{dt} &= v \\
\frac{dv}{dt} &= \frac{\beta i_2^2}{2m(d-x)^2} - \frac{\beta i_1^2}{2m(d+x)^2} - F_v v - F_c \operatorname{sgn}(v) \\
\frac{di_1}{dt} &= \frac{(u_1 - Ri_1)(d+x)}{\beta_0} + \frac{i_1 v}{d+x} \\
\frac{di_2}{dt} &= \frac{(u_2 - Ri_2)(d-x)}{\beta_0} - \frac{i_2 v}{d-x}
\end{aligned} \tag{4.20}$$

The state space vector is defined as $X = [x, v, i_1, i_2]'$ so that

$$\dot{X} = f(X, u_1, u_2) \tag{4.21}$$

A closed-form solution of the set of coupled partial differential equations (4.21) is hard to obtain at present, thus simplification is necessary.

For the dual solenoid system defined by the equation (4.20), it is assumed that dual solenoid system operates around the equilibrium point $\bar{X} = [\bar{x},\ \bar{v},\ \bar{i}_1,\ \bar{i}_2]'$. The linearization technique is based on the expansion of the nonlinear function in to a Taylor

series about the operating point. The closest linear system when X is close to linearized model of the nonlinear model (4.21) is given by:

$$\dot{X} = Df(\bar{X})(X - \bar{X}) \tag{4.22}$$

In equation (4.22), $\bar{X}$ is the equilibrium point of interest and $Df(\bar{X})$ is the Jacobian matrix of $f(\bar{X})$ evaluated at $\bar{X}$. Ignore the Coulomb friction $F_c \operatorname{sgn}(v)$, a linearized dual solenoid model is given in (4.23).

$$\begin{bmatrix} \frac{d\delta x}{dt} \\ \frac{d\delta v}{dt} \\ \frac{d\delta i_1}{dt} \\ \frac{d\delta i_2}{dt} \end{bmatrix} = \left[\begin{array}{cccc} 0 & 1 & 0 & 0 \\ \frac{\beta \bar{i}_2^2}{m(d-\bar{x})^3} + \frac{\beta \bar{i}_1^2}{m(d+\bar{x})^3} & -F_v & -\frac{\beta \bar{i}_1}{m(d+\bar{x})^2} & \frac{\beta \bar{i}_2}{m(d-\bar{x})^2} \\ \frac{\bar{u}_1 - R_1 \bar{i}_1}{\beta} - \frac{\bar{i}_1 \bar{v}}{(d+\bar{x})^2} & \frac{\bar{i}_1}{d+\bar{x}} & \frac{v}{d+\bar{x}} - \frac{R_1(d+\bar{x})}{\beta} & 0 \\ -\frac{\bar{u}_2 - R_2 \bar{i}_2}{\beta} - \frac{\bar{i}_2 \bar{v}}{(d-\bar{x})^2} & -\frac{\bar{i}_2}{d-\bar{x}} & 0 & -\frac{\bar{v}}{d-\bar{x}} - \frac{R_2(d-\bar{x})}{\beta} \end{array} \right]_{\substack{\bar{x} \\ \bar{v} \\ \bar{i}_1 \\ \bar{i}_2 \\ \bar{u}_1 \\ \bar{u}_2}} \begin{bmatrix} \delta x \\ \delta v \\ \delta i_1 \\ \delta i_2 \end{bmatrix}$$

$$+ \left[\begin{array}{cc} 0 & 0 \\ 0 & 0 \\ \frac{d+\bar{x}}{\beta_0} & 0 \\ 0 & \frac{d-\bar{x}}{\beta_0} \end{array} \right]_{\bar{x}} \begin{bmatrix} \delta u_1 \\ \delta u_2 \end{bmatrix} \tag{4.23}$$

In which $\bar{X} = \begin{bmatrix} \bar{x} & \bar{v} & \bar{i}_1 & \bar{i}_2 \end{bmatrix}'$ is the equilibrium point of interest, $\bar{x} \in [-1.5mm, 1.5mm]$.

It should be noted that given a commercial solenoid, manufacturers only supply geometric dimensions and basic static performance data of commercial solenoids, such as resistance, number of turns, and force-stroke characteristics, other than magnetic flux reluctance and parameters in equation (4.6)~(4.8), thus some identification techniques are

necessary to achieve accurate parameters of the dynamic model. The parameter identification is based on the closed loop experimental data. The parameters in equation (4.20) are identified as:

$$\begin{aligned} d &= 3.85\times10^{-3} m, \qquad & R &= 100\Omega \\ \beta_0 &= 4.4\times10^{-4} Nm^2/A^2, \qquad & m &= 0.015kg \\ F_v &= 18.5N\cdot s/m \end{aligned} \tag{4.24}$$

The Coulomb friction coefficient F_c varies from time to time.

4.3 Inner Feedback Loop Design on Dual Solenoid Micro-positioner

The primary control objective of this work is to obtain fast speed of position response with smooth transient characteristics for the dual solenoid position actuator. This section deals with two types of feedback controllers: On-off control and Zero Vibration On-off (ZVOO) control.

4.3.1 On-off Control on Dual Solenoid Micro-positioner

To achieve high speed response, control signals must be large enough to produce a strong magnetic force. An on-off type of control is most suited for this purpose. The basic operation is to drive the actuator with maximum voltage (full forward) if the position is less than the set point, otherwise go full reverse, which makes On-off control to be a nonlinear control method (R. Wai, 2003). An error tolerance range $[-a, a]$ is introduced so that for error falling with in this range, both control signals are set to zero. Rules of operation are shown in Figure 4.3 and summarized as follows:

If $x > a$, turn off solenoid 1, turn on solenoid 2;

Else if $x < -a$, turn on solenoid 1, turn off solenoid 2;

Else ($-a \le x \le a$), turn off both solenoids.

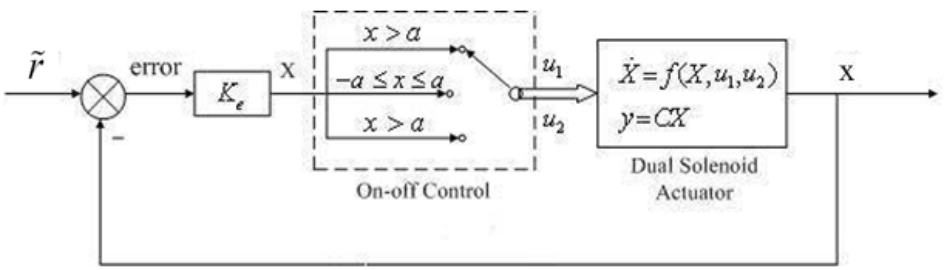

Figure 4.3 Block diagram of on-off control.

There are three parameters for the on-off control: threshold a, gain K_e, and on-amplitude u_0. Thus the control signals for solenoids 1 and 2 can be summarized as follows:

$$u_1 = u_0 \cdot H(a - K_e\tilde{r} + K_e x) \tag{4.25}$$

$$u_2 = u_0 \cdot H(K_e\tilde{r} - K_e x - a) \tag{4.26}$$

The proposed on-off control is simulated in Simulink and the results are plotted in Figure 4.4 where the control parameters are set to u_0 = 6 volts, $a = 0.02 \times 10^{-3} m$, and $K_e = 0.5$.

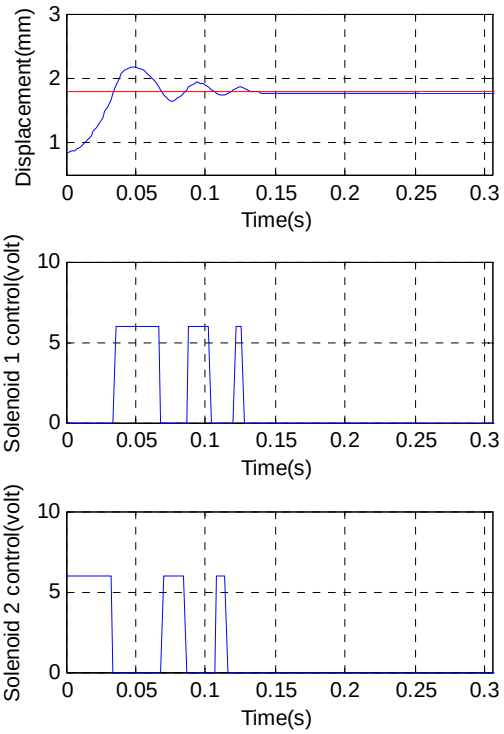

Figure 4.4 Step response of on-off control system with 1.8*mm* set point. (top) Step response of on-off control system; (middle) Control signal for solenoid 1; (bottom) Control signal for solenoid 2.

4.3.2 Balance Control on Dual Solenoid Micro-positioner

The control signals to solenoid 1 and solenoid 2 are designed based on the difference between the reference command and current position measured by Fotonic sensor. Because each solenoid is essentially unipolar (i.e. the force generated is unidirectional), the solenoids only respond with the absolute values of u_1 and u_2. A balance voltage *Bal* is necessary to keep both control signals positive. The basic operation of balance controller is designed as follows,

$$u_1 = Bal - K[K_{MO}\tilde{r} - x] \tag{4.27}$$

$$u_2 = Bal + K[K_{MO}\tilde{r} - x] \tag{4.28}$$

In which Bal is a balance level, K is the gain to the error, and K_{MO} is the modify gain to let position x track the reference command precisely. The block diagram of dual solenoid position system with balance control is shown in Figure 4.5.

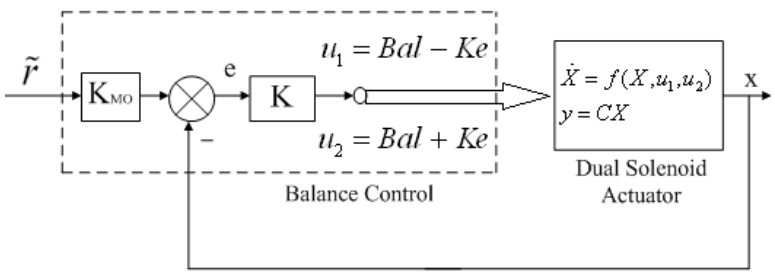

Figure 4.5 Block diagram of Balance control.

To get the linear model of balance control system, define equilibrium point as

$$\bar{i}_1 = \frac{\bar{u}_1}{R} \tag{4.29}$$

$$\bar{i}_2 = \frac{\bar{u}_1}{R} \tag{4.30}$$

$$\bar{v} = 0, \quad \bar{x} = 0 \tag{4.31}$$

$$\bar{u}_1 = \bar{u}_2 = Bal\sqrt{2} \tag{4.32}$$

It is noted that

$$\delta u_1 = u_1 - \bar{u}_1 \tag{4.33}$$

$$\delta u_2 = u_2 - \bar{u}_2 \tag{4.34}$$

$$x = \bar{x} + \delta x \tag{4.35}$$

The control signals for linear system (4.23) are calculated from equations (4.27) ~ (4.35).

$$\delta u_1 = -K\left[K_{MO}\tilde{r} - \delta x\right] \tag{4.36}$$

$$\delta u_2 = K\left[K_{MO}\tilde{r} - \delta x\right] \tag{4.37}$$

Insert (4.36) and (4.37) into (4.25), and let

$$\begin{aligned} x_1 &= \delta x \\ x_2 &= \delta v \\ x_3 &= -\delta i_1 + \delta i_2 \end{aligned} \tag{4.38}$$

The simplified 3rd-order linear state space model of closed loop dual solenoid position system is given in (4.39).

$$\begin{bmatrix} \frac{dx_1}{dt} \\ \frac{dx_2}{dt} \\ \frac{dx_3}{dt} \end{bmatrix} = \begin{bmatrix} 0 & 1 & 0 \\ \frac{2\beta_0 Bal^2}{md^3R^2} & -F_v & \frac{\beta_0 Bal}{md^2R} \\ -K\frac{2d}{\beta_0} & -\frac{2Bal}{dR} & -\frac{Rd}{\beta_0} \end{bmatrix} \begin{bmatrix} x_1 \\ x_2 \\ x_3 \end{bmatrix} + \begin{bmatrix} 0 \\ 0 \\ \frac{2KK_{MO}d}{\beta_0} \end{bmatrix} \tilde{r} \tag{4.39}$$

If the parameter of Balance control is set as *Bal*=4 volts, *K*=7500, and $K_{MO} = 0.8615$, the eigenvalues of system (4.39) are –886.63 , -3.43 ± 100.41i respectively so the linear dynamics are underdamped. Now define that

$$C = [1 \quad 0 \quad 0], \text{ D=0} \tag{4.40}$$

Then the dual solenoid positioner impulse response is calculated as:

$$G(s) = \frac{11.33}{s + 886.63} + \frac{-11.33s + 99.66}{(s + 3.43)^2 + 100.41^2} \tag{4.41}$$

Although the close loop solenoid position system is stable, the transient vibrations may affect the performance of the system. In the next section, a typical input shaping technique-Zero Vibration is designed to reduce the transient vibrations.

4.4 Feedforward Control Design on Dual Solenoid Micro-positioner

4.4.1 Zero Vibration On-off Control on Dual Solenoid Micro-positioner

Figure 4.6 shows the block diagram of Zero Vibration On-off (ZVOO) control.

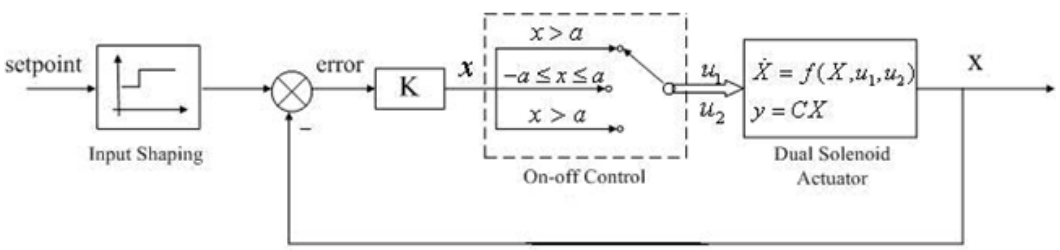

Figure 4.6 Block diagram of ZVOO control.

For the dual solenoid actuator with On-off controller (4.27) and (4.28), the transfer function can be written as:

$$G(s) = \bar{G}_1(s) + \bar{G}_2(s) \tag{4.42}$$

In which $\bar{G}_1(s)$ accounts for the oscillatory dynamics which can be simplified as a second order system, and $\bar{G}_2(s)$ represents the parasitic dynamics. The overshoot K can be easily calculated or measured from Figure 4.4 as K= 0. 4079, and the two impulses of the ZV shaper are calculated from equation (3.17) ~ (3.19):

$$A_1 = 0.7103,\ A_2 = 0.2897 \tag{4.43}$$

$$t_1 = 0, \qquad t_2 = 0.052 \text{ sec} \tag{4.44}$$

For different set points r and initial position x_0, the ZV command amplitudes can be calculated as follows,

$$A_1^{'} = A_1 \cdot (r - x_0) + x_0, \tag{4.45}$$

$$A_2^{'} = r - A_1^{'} \tag{4.46}$$

Presence of the parasitic term $G_2(s)$ in the model leads to a change in peak time t_p, to further reduce the residual vibration, t_2 should be adjusted based on the peak time as shown in Figure 4.7 where it is observed a small offset is present due to the parasitic dynamics:

$$t_2 = t_p - 0.008 \tag{4.47}$$

In the simulation verification, the sampling rate of the controller is set to 500Hz which is the same as the actual experimental conditions.

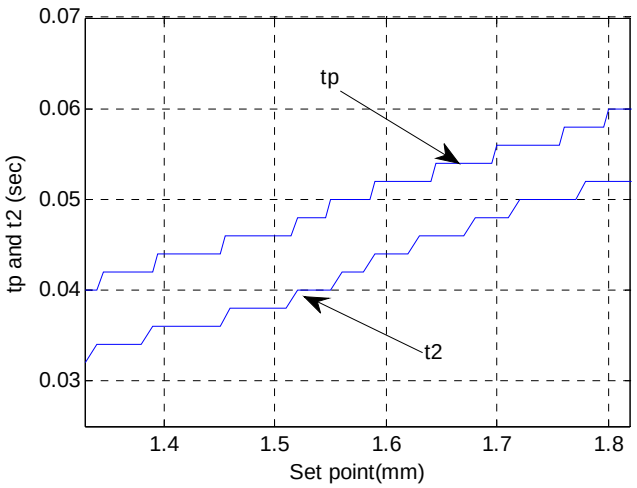

Figure 4.7 Comparison of peak time t_p and tuned t_2 by simulation.

The on-off control with ZV shaper is summarized as follows,

$$u_1 = \begin{cases} 0, & t < 0 \\ u_0 \cdot H(a - K_e \cdot A_1^{'} + K_e \cdot x), & 0 \le t \le t_2 \\ u_0 \cdot H(a - K_e \cdot r + K_e \cdot x), & t > t_2 \end{cases} \tag{4.48}$$

$$u_2 = \begin{cases} 0, & t < 0 \\ u_0 \cdot H(K_e \cdot A_1^{'} - K_e \cdot x - a), & 0 \le t \le t_2 \\ u_0 \cdot H(K_e \cdot r - K_e \cdot x - a), & t > t_2 \end{cases} \tag{4.49}$$

A list of ZV control parameters is given in Table 4.1 below, and corresponding simulation results are shown in Figure 4.8 and 4.9.

Table 4.1 ZV Shaper Parameters (Simulation)

Set Point (mm)	**A_1** (mm)	**A_2** (mm)	**t_2** (s)
1.5	1.3117	0.1883	0.038
1.65	1.4182	0.2318	0.046
1.8	1.5248	0.2752	0.052

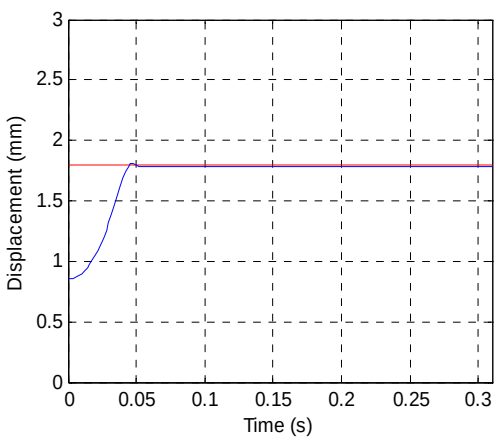

Figure 4.8 Simulated Step response of ZVOO control system with 1.8mm set point.

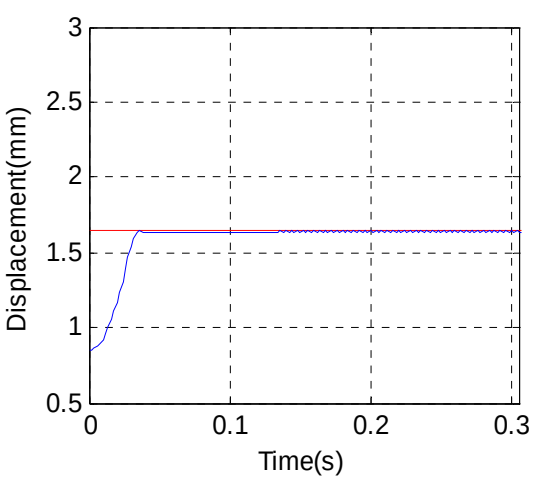

Figure 4.9 Simulated Step response of ZVOO control system with 1.65mm set point.

Parameters of on-off control remain the same as ones in the regular on-off control described in section 4.3.1. Compared with On-off control alone (Figure 4.4), the ZVOO control (Figure 4.8) suppresses both overshoot and residual vibration significantly.

4.4.2 Zero Vibration Balance Control on Dual Solenoid Micro-positioner

The ZV command is obtained by convolving the reference command with a sequence of two impulses. For step inputs, the result is a staircase command. To obtain zero vibration for the linearized dual solenoid system (4.23), the ZV shaper is listed in Table 4.2.

Table 4.2 ZVB Parameters

t_1	t_2	A_1	A_2
0	0.0313	0.5268	0.4732

4.5 Model Reference Zero Vibration Balance Control

It is well known that the ZV shaper is not sufficiently robust with respect to variations in system parameters as well as the nonlinear dynamics and Coulomb friction present in the actual system. To compensate for the Coulomb friction and to increase the robustness of the system, a model reference controller is designed in this paper.

Model Reference Zero Vibration Balance (MRZVB) control consists of a ZV shaper as the feed forward control, model reference feedback and balance control feedback. The Balance controller described in equation (4.27) ~ (4.28) is applied to the

dual solenoid actuator as the basic position feedback to stabilize the system. A standard ZV input shaper is derived based on the reference model. The parameters of ZV shaper are listed in Table 4.2. The block diagram of model reference controller is shown in Figure 4.10. The control strategy to solenoid 1 and solenoid 2 is summarized in (4.50) ~ (4.53).

$$\bar{u} = -k_{mp}(x - x_m) \tag{4.50}$$

$$e = K_{MO}(\tilde{r} + \bar{u}) - x \tag{4.51}$$

$$u_1 = Bal - Ke \tag{4.52}$$

$$u_2 = Bal + Ke \tag{4.53}$$

where k_{mp} is the model reference feedback gain, $\tilde{r}$ is the reference signal pre-filtered by ZV shaper, and x_m is the displacement of reference model along x direction.

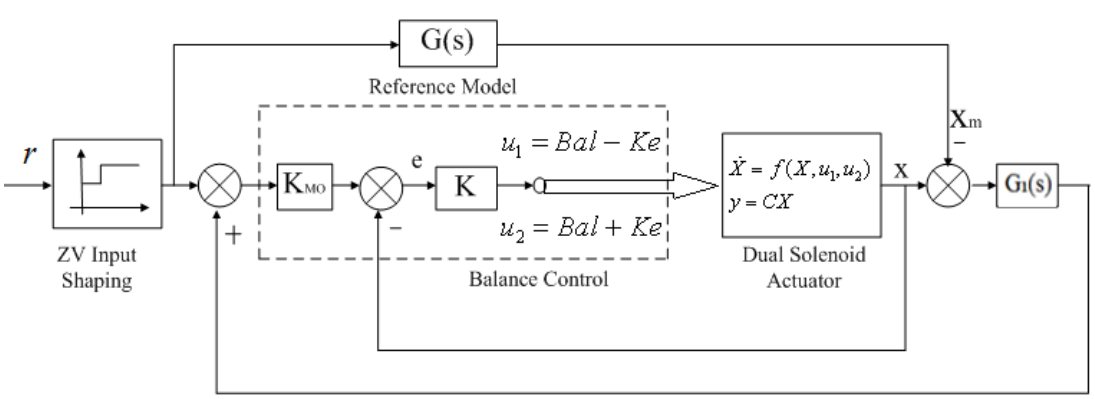

Figure 4.10 Block diagram of dual solenoid system with MRZVB.

4.6 Variable Model Reference Zero Vibration Balance Control

To further effect the transient characteristics of MRZVB, it is possible to vary the linear reference model whose properties and subsequent control design are well understood. For linear reference model (4.23), different Balance control gain K results in different peak time, thus the settling time of the reference model with ZV shaper varies correspondingly. The settling time of the system (4.20) with MRZVB can also be quantitatively adjusted by systematically varying the reference model. Table 4.3 lists the settling time of reference model with various control gain K.

Table 4.3 Settling Time of Reference Model with Various Gain K

Balance gain K	**Settling time of reference model** ($\pm 2\%$) (s)
6000	0.0337
7500	0.0298
9000	0.0276

CHAPTER 5

MODELING AND CONTROL OF CRUCIFORM PIEZOELECTRIC NANO-POSITIONER

This chapter deals with the modeling and control design of monolithic cruciform piezoelectric nano-positioner.

5.1 Modeling of Monolithic Cruciform Piezoelectric Positioning Stage

The piezoelectric ceramic has the characteristics of high resolution, fast transient response and potential low cost, so it can be applied in many fields of precision control and precision instrument, such as microscopes, medical and optics. Among the piezoelectric actuators invented and applied recently, the monolithic cruciform nano-actuator studied in this work has the advantages of wide bandwidth, high resolution, and low cost, which make it valuable in applications and worthy of studying.

The 2-axis monolithic piezoelectric positioner studied in this work is part of a 6-DOF manipulator patented by Dr. Timothy Chang. The cruciform structure is shown in Figure 5.1. The actuator is a positioning device capable of providing 2- degree-of-freedom (DOF): x and y axes. This 2- DOF actuator is constructed from a single piezoelectric plate with the material of lead zirconate-lead titanate (PZT). The top and bottom faces of the piezoelectric actuator have the same structure: the four shadow parts are covered by silver, an electric conductive material to form the electrodes. In order to measure the displacements in x and y axes, a cubic target is attached in the middle of the top face as a contact surface of the capacitive sensor. A plastic frame clamps the four edges of the cruciform to restrict the deformation on the four edges. The capacitance

sensor and the nano-positioner are fixed on a metal fixture which was mounted on a vibration isolation table. Four micrometers are designed to align the probe of capacitance sensor: one is on the base of the PZT and one locates on the fixture of the sensor for each axis.

However, some inherent nonlinearities in piezoelectric ceramic such as friction, hysteresis may lead to undesirable performance, including loss of robustness and steady state error, especially when the electric field strength or the piezoelectric sensitivity of the material increases. X. Sun and T. Chang (2001) have studied and formulated the hysteresis behavior and nonlinear scale factor.

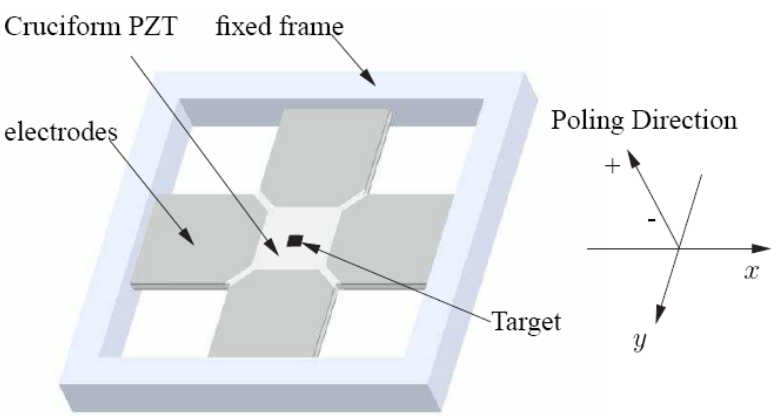

Figure 5.1 Draft of monolithic cruciform nano-actuator.

Figure 5.2 shows the wiring of electrodes which correspond to the linear motion along x axis. When driving voltage V_x is applied to the electrode pair in shadow section I, the deformation effect is expansion; while $-V_x$ is simultaneously applied to the electrode pair in section II, the corresponding deformation is contraction. In this way, a linear motion of the target in positive x direction is accomplished.

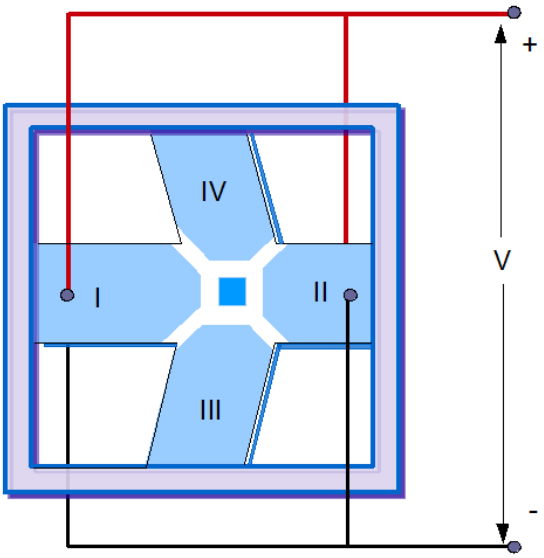

Figure 5.2 Wiring of electrode and deformation effect of cruciform nano-positioner.

The displacement along x direction is given by X. Sun (2001):

$$\Delta x = d_{31}\frac{l}{h}V_x \tag{5.1}$$

Where l and h describe the length and thickness of the section respectively, d_{31} represents the piezoelectric voltage constant with typical value of $-250\times10^{-12}\ m/V$, P_x is the pressure produced by the deformation, Y_{11}^E is the Young's modulus with typical value of $6\times10^{10}\,N/m^2$.

$$P_x = d_{31}Y_{11}^E\frac{V_x}{h} \tag{5.2}$$

Many prior studies have been done to model the piezoelectric actuators (Chang et al. in 2001, and Adriaens et al. in 2000). Due to the orthogonal geometry, the cross coupling effect between the two axes is relatively low. The position of the two axes can therefore be modeled and controlled independently. In this work, a proportional feedback controller is applied on the piezoelectric actuator during the system identification procedure. The cruciform piezoelectric actuator with such feedback loop is identified as a forth-order linear system as shown in equation (5.3).

$$\begin{aligned}
\frac{dx_1}{dt} &= v_1 \\
\frac{dx_2}{dt} &= v_2 \\
\frac{dv_1}{dt} &= -2\zeta_1\omega_1 v_1 - \omega_1^2 x_1 + D_1\omega_1^2 r \\
\frac{dv_2}{dt} &= -2\zeta_2\omega_2 v_2 - \omega_2^2 x_2 + D_2\omega_2^2 r \\
y &= x_1 + x_2
\end{aligned} \tag{5.3}$$

In which r is the set point on x axis; x_1 is the displacement of the first harmonic mode of the truncated distributed spatial model in microns; x_2 is the displacement of the third harmonic mode of the truncated distributed spatial model in microns; y represents the displacement of the actuator along x axis; ω_1 is the natural frequency of the first harmonic vibration mode; ω_2 is the natural frequency of the third harmonic vibration mode, i.e., it is three times of ω_1; ζ_1 and ζ_2 are the damping ratios of each vibration mode; D_1 and D_2 are the gains of the drive voltage of each vibration mode; v_1 and v_2 are the speed of the first and third harmonic modes respectively.

According to the model (5.3), the displacement along x axis can be regarded as the superposition of x_1 and x_2. The equivalent linear model (5.3) doesn't consider any nonlinearity, such as friction, hysteresis, and creep. The parameters in model (5.3) may vary with the amplitude of the set point and the proportional gain with the existence of its inherent nonlinearities. Under the general operating conditions $r = 1\mu m,$ and proportional gain $K_p = 0.3$, the parameters of model (5.3) are identified in Equation (5.4).

$$\begin{bmatrix} \frac{dx_1}{dt} \\ \frac{dx_2}{dt} \\ \frac{dv_1}{dt} \\ \frac{dv_2}{dt} \end{bmatrix} = \begin{bmatrix} 0 & 0 & 1 & 0 \\ 0 & 0 & 0 & 1 \\ -1.18\times10^{7} & 0 & -549.9 & 0 \\ 0 & -1.06\times10^{8} & 0 & -103.11 \end{bmatrix} \begin{bmatrix} x_1 \\ x_2 \\ v_1 \\ v_2 \end{bmatrix} + \begin{bmatrix} 0 \\ 0 \\ 1.12\times10^{7} \\ 3.02\times10^{7} \end{bmatrix} \mathrm{r} \tag{5.4}$$

$$y = \begin{bmatrix} 1 & 1 & 0 & 0 \end{bmatrix} [x_1 \quad x_2 \quad v_1 \quad v_2]' \tag{5.5}$$

In Equation (5.4), the parameters are identified as in Table 5.1, where the frequencies are expressed in rad/s.

Table 5.1 Experimental Identified Parameters of Piezoelectric Nano-positioner

	First harmonic vibration mode	**Third harmonic vibration mode**
Natural frequency	$\omega_1 = 3436.9$	$\omega_2 = 10264$
Damping ratio	$\zeta_1 = 0.08$	$\zeta_1 = 0.0046$
Drive voltage gain	$D_1 = 4.3332$	$D_2 = 1.3$

5.2 Control Design on Piezoelectric Nano-actuator

The primary control objective of high precision positioning systems is to obtain fast speed of position response with smooth transient characteristics and low steady state error for the cruciform piezoelectric actuator. Three types of control are considered: PI control, 2-mode ZV control, and MRZV control.

5.2.1 PI Control on Piezoelectric Nano-positioner

PI control is widely used in motion control systems for its simplicity and robust performance at low frequencies. It is generally effective on overcoming creep and hysteresis effects (Devasia et al. in 2007). The following PI control strategy is applied to the cruciform piezoelectric actuator:

$$u = K_p\left(\tilde{r} - x\right) + K_i\int\left(\tilde{r} - x\right)dt \tag{5.6}$$

In Equation (5.6), K_p and K_i represent the proportional and integral gains respectively. To further evaluate the control performance, the root mean square error (RMSE) of the transient response with various proportional and integral gains is utilized.

$$y_{rms} = \sqrt{\frac{\sum_{i=1}^{n}\left(y_i - r\right)^2}{n}} \tag{5.7}$$

In Equation (5.7), n represents the number of sampled data and y_i represents the ith sampled data. Table 5.2 lists the simulated RMSE of the transient response of nanopositioner with various proportional and integral gains. The reference command is

set as 1 micron, and the evaluation time is 0.2 second. It is observed that the optimal PI control parameters based on the simulation results are $K_p = 0.3,$ and $K_i = 333.$

Table 5.2 RMSE of Simulated Step Response of Nanopositioner with Various PI Gaines (Set Point =1 μm)

		Proportional gain K_p				
		-0.5	**0.1**	**0.3**	**0.5**	**5**
Integral gain K_i	**125**	Unstable	0.3666	0.3284	0.3092	0.3802
	333	Unstable	0.2753	0.2557	0.2561	0.4022
	1000	Unstable	Unstable	Unstable	Unstable	0.5036
	3000	Unstable	Unstable	Unstable	Unstable	Unstable

5.2.2 2-mode ZV Control on Piezoelectric Nano-positioner

Input shaping is a feedforward technique to suppress command–induced vibrations. A brief mathematical overview of input shaping is presented in Chapter 3. In this section, a 2-mode zero vibration input shaping is designed based on the fourth order system model in Equations (5.4) and (5.5).

Consider the following transfer function with first harmonic mode:

$$G_1(s) = \frac{\omega_1^2}{s^2 + 2\zeta_1\omega_1 s + \omega_1^2} \tag{5.8}$$

The amplitude and time of the impulses of the ZV shaper are calculated based on equations (5.9), and (5.10).

$$A_{11} = \frac{1}{1+e^{\frac{-\pi\zeta_1}{\sqrt{1-\zeta_1^2}}}}, \qquad A_{12} = \frac{e^{\frac{-\pi\zeta_1}{\sqrt{1-\zeta_1^2}}}}{1+e^{\frac{-\pi\zeta_1}{\sqrt{1-\zeta_1^2}}}} \tag{5.9}$$

$$t_{11} = 0, \qquad t_{12} = \frac{\pi}{\omega_1\sqrt{1-\zeta_1^2}} \tag{5.10}$$

Similarly, the shaper to eliminate the second vibration mode $G_2(s) = \frac{\omega_2^2}{s^2 + 2\zeta_2\omega_2 s + \omega_2^2}$ can be designed in the same way. Based on the I/O characteristics of the nanopositioner with Proportional control, the corresponding single mode shaper parameters are listed in Table 5.3.

Table 5.3 Single Mode ZV Shaper Parameters

Switching time (second)	**Pulse amplitude**
$t_{11} = 0$	$A_{11} = 0.5627$
$t_{12} = 9.17\times10^{-4}$	$A_{12} = 0.4373$
$t_{21} = 0$	$A_{21} = 0.5036$
$t_{22} = 3.05\times10^{-4}$	$A_{22} = 0.4961$

For a multi-mode system, a single-mode shaper is computed for each mode, and the multi-mode shaper is obtained by convolving all single-mode shapers. A multi-mode input shaping command is designed for model (5.4) and (5.5) with parameters defined in Table 5.1, is listed in Table 5.4. The ZV command is obtained by convolving the reference command with a sequence of four impulses, and is shown in Figure 5.3.

Table 5.4 2-mode ZV Shaper Parameters

Switching time t_i (second)	**Pulse amplitude C_i**
$t_1 = 0$	$C_1 = 0.2834$
$t_2 = 3.05\times10^{-4}$	$C_2 = 0.2792$
$t_3 = 9.17\times10^{-4}$	$C_3 = 0.2202$
$t_4 = 12.22\times10^{-4}$	$C_4 = 0.2169$

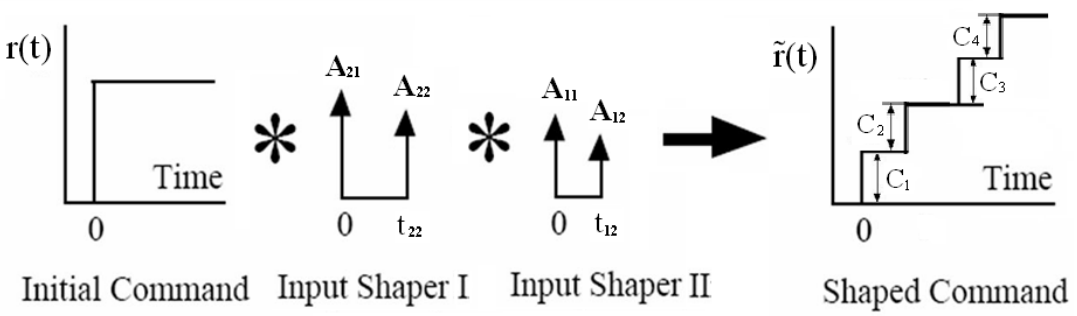

Figure 5.3 Input shaping of a step command to produce 2-mode input shaping staircase command.

The 2- mode ZV shaper is a staircase command given in Equation (5.11).

$$\tilde{r}(t) = r\sum_{i=1}^{4} C_i \cdot H(t - t_i) \tag{5.11}$$

5.2.3 MRZV Control on Piezoelectric Nano-positioner

MRZV control consists of a ZV shaper as the feed forward control, model reference feedback and proportional control feedback. A proportional controller in Equation (5.3) is

applied to the PZT actuator as the basic position feedback to stabilize the system. A standard ZV input shaper is derived based on the reference model in Equation (5.3). The parameters of this 2-mode ZV shaper are listed in Table 5.3. The block diagram of model reference controller is shown in Figure 5.4. The reference model is a fourth-order linear system, which is a linear approximation of the PZT actuator under certain circumstances. The parameters of the reference model come from the experimental test.

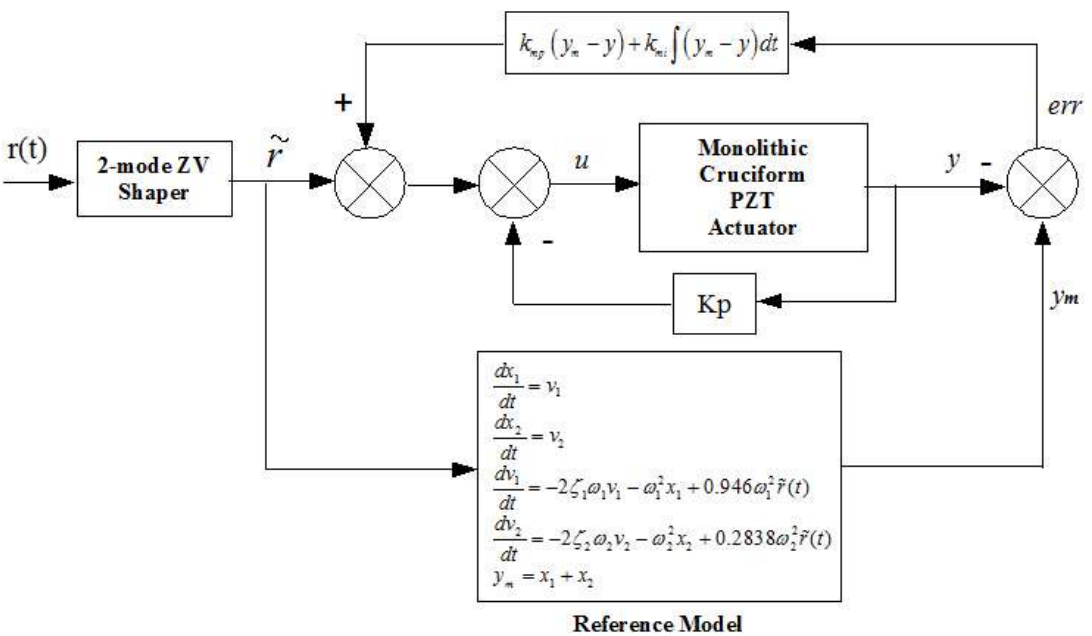

Figure 5.4 Block diagram of MRZV control on piezoelectric nano-actuator.

The digitized form of control strategy to the PZT actuator with sampling rate of 10K Hz is presented in Equations (5.12) and (5.13).

$$
\begin{aligned}
u(n) &= 0.1918K_{mp}\tilde{r}(n-1) - 0.1172K_{mp}\tilde{r}(n-2) - 0.1217K_{mp}\tilde{r}(n-3) + 0.1825K_{mp}\tilde{r}(n-4) \\
&\quad + 2.855K_{mp}y_m(n-1) - 3.81K_{mp}y_m(n-2) + 2.782K_{mp}y_m(n-3) - 0.9368K_{mp}y_m(n-4) \\
&\quad - (K_{mp}+0.3)y(n) + \tilde{r}(n) + 0.0001K_{mi}\sum_{i=0}^{n}\begin{bmatrix} 0.1918\tilde{r}(i-1) - 0.1172\tilde{r}(i-2) \\ -0.1217\tilde{r}(i-3) + 0.1825\tilde{r}(i-4) \\ +2.855y_m(i-1) - 3.81y_m(i-2) \\ +2.782y_m(i-3) - 0.9368y_m(i-4) \\ -y(i) \end{bmatrix}
\end{aligned} \tag{5.12}
$$

$$
\tilde{r}(n) = \begin{cases} 0, & \text{if } n \in (-\infty, 0); \\ 0.2836r, & \text{if } n \in [0,3); \\ 0.5627r, & \text{if } n \in [0,9); \\ 0.7831r, & \text{if } n \in [0,12); \\ r, & \text{if } n \in [12,\infty). \end{cases} \tag{5.13}
$$

In Equation (5.12), $K_{mp} = 0.3$ and $K_{mi} = 1000$ represent the proportional and integral gains of the model reference controller respectively; y_m is the displacement of reference model in microns; $\tilde{r}(n)$ is the discrete time ZV shaper command designed in Equation (5.11). Sampling rate is set to 10k Hz.

CHAPTER 6

EXPERIMENTAL SETUP

This chapter deals with the experimental setup of the ultra-high precision positioning system studied in this work. The whole setup of the positing stage is introduced first in section 6.1. The detailed descriptions of the dual solenoid micro-positioner and the cruciform piezoelectric nano-positioner, which consist of the working principles and characteristics of the relative actuators and displacement measurement devices, hardware configurations for the control systems, and description of software realization, are given in section 6.2 and section 6.3 respectively.

6.1 Ultra-high Precision Actuators

The sketch of the two-axis ultra-high precision positioning system driven by the dual solenoid micro-positioner and cruciform piezoelectric nano-positioner is shown in Figure 6.1. Along each axis, there is one dual solenoid micro-positioner with displacement range of 0mm~3mm and resolution of 6 micrometers as coarse positioning actuator. One pair of the solenoid cores can be fixed to a heavy base which is mounted on the vibration isolation table to actuate the movable stage attached on the plunger of the solenoid pair; while the other pair of solenoid cores are fixed on the movable stage. In this way, the PZT frame attached on the push-pull plunger of the later dual solenoid positioner can be driven by both dual solenoid positioners in x- and y- directions. The target in the center of the cruciform piezoelectric nano-poaitioner is a platform for the components or particles to be moved or to be manipulated.

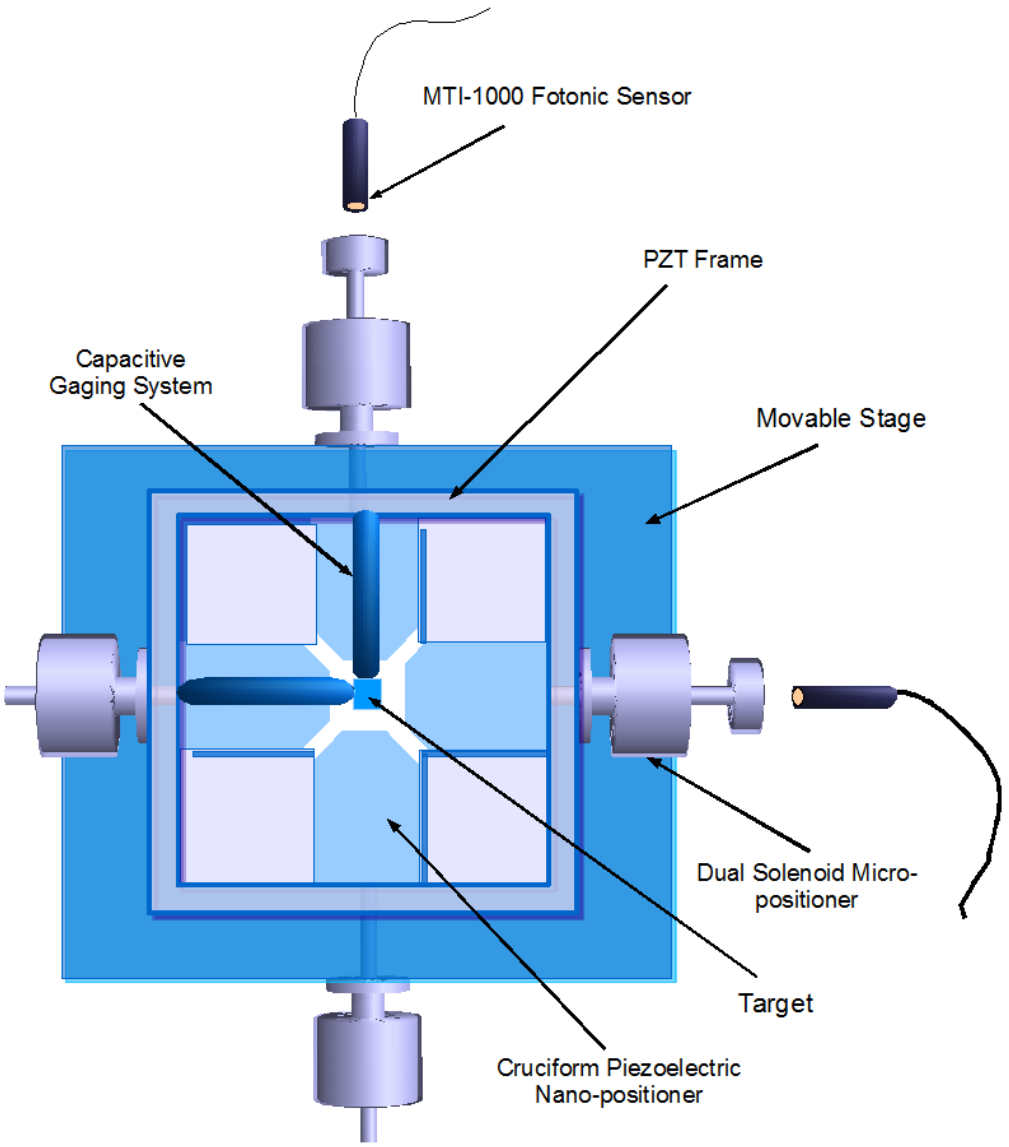

Figure 6.1 Sketch of ultra-high precision system.

This hybrid design of electromagnetic-piezoelectric-nanopositioner combines the potentials of large travel range at low operating voltages for dual solenoid micro-positioner and high resolution for cruciform monolithic piezoelectric nano-positioner. The overall resolution can be sub-nanometer while the moving range is in millimeters, a three order of magnitude increase from using piezoelectric positioner alone, namely from

10^{-6} m to 10^{-3} m. There is no component coupling effects among the two dual solenoid positioners, and the monolithic piezoelectric actuators. It is possible to separate the designing task of meeting performance specifications, resolution requirement and travel range into two types of actuators.

6.2 Dual Solenoid Micro-positioner

Figure 6.2 and 6.3 are the physical system of dual solenoid positioning actuator and experimental setup for the control system of dual solenoid micro-positioner respectively. The dual solenoid actuator is composed of two identical commercial push-pull solenoids SMT. The cores of the two solenoids are held in place with the plunger axes aligned. The plungers are connected by a metal coupler in the axial direction. At one end of the plunger, a mirror is fixed as the reflection surface of the Fotonic^{TM} Sensor, which is a fiber-optic system that performs non-contact displacement measurements. The travel range of the dual solenoid micro-positioner is 0~3mm, and the resolution is of the positioning system is 6 μm.

To implement the proposed control method on the dual solenoid actuator, a real-time operating system is composed by a personal computer (PC) with National Instruments LabVIEW 8.0 software and a PCI-6024E data acquisition (DAQ) card which is able to monitor analog inputs from the Fotonic^{TM} Sensor and to drive analog voltage outputs to the power amplifier.

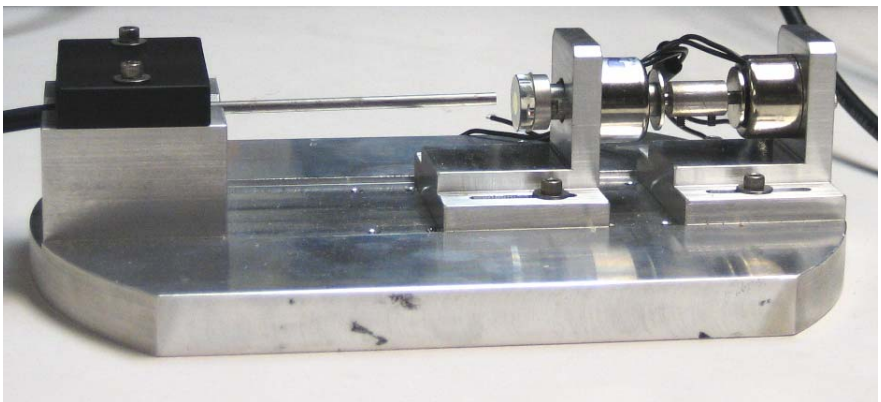

Figure 6.2 Picture of dual solenoid positioning actuator.

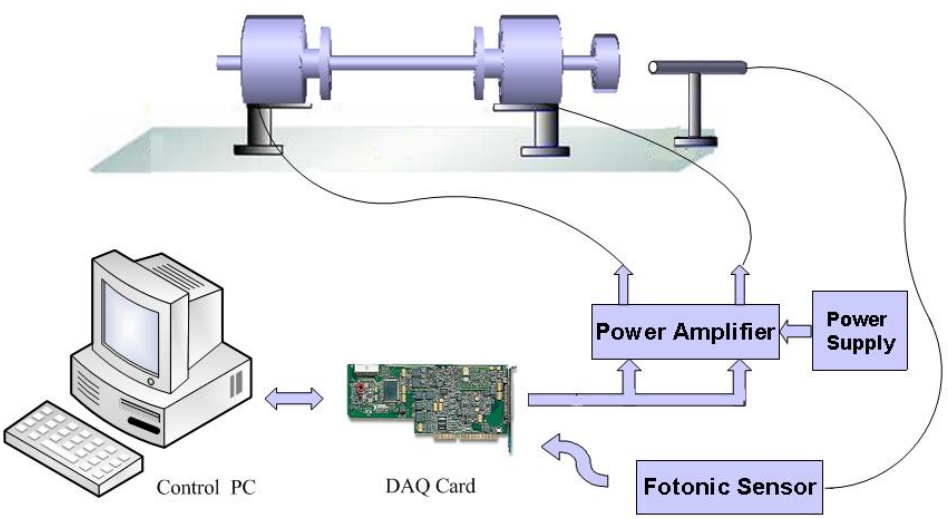

Figure 6.3 Experimental setup for control system of dual solenoid micro- positioner.

6.2.1 MTI-1000 Fotonic Sensor

To measure the displacement in ultra-high precision positioning system accurately, sensors which are able to offer non-contact measurement are suggested. Since the sensing systems never makes contact with the part, there are no force and parts distortion. The MTI-1000 Fotonic sensor is such a high precision, high bandwidth, non contact

displacement/vibration measurement unit. This subsection describes the characteristics, principles of operation, and performance characteristics of Fotonic^{TM} sensors.

In this work, the Fotonic^{TM} Sensor is utilized as a contactless fiber-optic displacement sensor. The probe of Fotonic module contains two types of optical fibers, light-transmitting fibers and light receiving fibers. The distribution of the transmitting and receiving fibers at the probe tip is in random manner as shown in Figure 6.4 (a). The operating principle of Fotonic probe is shown in Figure 6.4 (b). The collimated light beam generated by a controlled light source is carried by the transmitting fibers toward the probe tip and the target, while the reflected light from the target is carried back to a photo-detector through the receiving fibers. The light intensity is proportional to the distance between the target and the tip of the probe in the limited ranges: range 1 and range 2 shown in Figure 6.4 (b). The MTI-1000 Fotonic sensor is able to measure displacement motion ranging from 0.25 nm to 5.08 mm at frequencies ranging from DC to over 150 kHz.

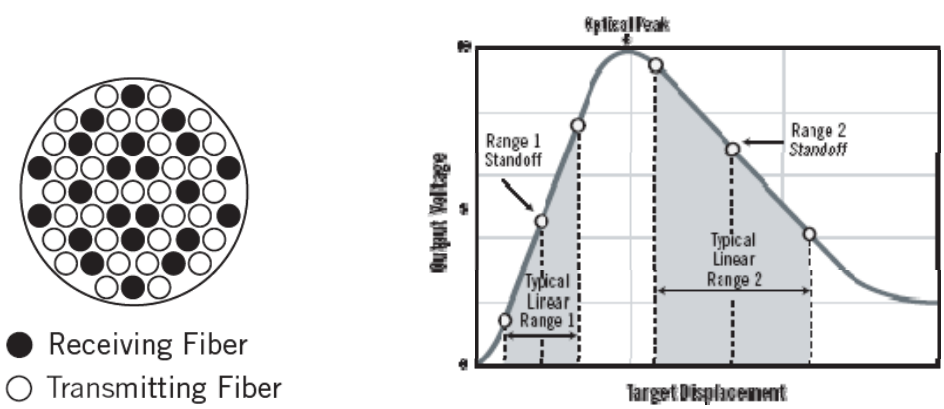

(a) Fiber distribution (b) Linear measure range

Figure 6.4 Operating principle of Fotonic sensor (MTI Instruments Inc., 2007).

In this work, range 1 is chosen based on the consideration of travel range of dual solenoid actuator. The corresponding recalibration curve (see Figure 6.5) can be modeled by a 3rd-order polynomial:

$$y' = 0.0166y^3 + 0.1266y^2 + 0.5276y + 1.5445 \qquad (6.1)$$

in which y represents the displacement of the dual solenoid actuator in millimeters: y equals to zero when the plunger stays on the left end, and y equals to 3mm when the plunger is on the right end; y' represents the output voltage of the sensor in volts. For the experimental range of operation, an inverse function is determined as:

$$y = -3.715 + 3.263y' - 0.623y'^2 + 0.05y'^3 \qquad (6.2)$$

From this inverse function, the displacement output can be linearized.

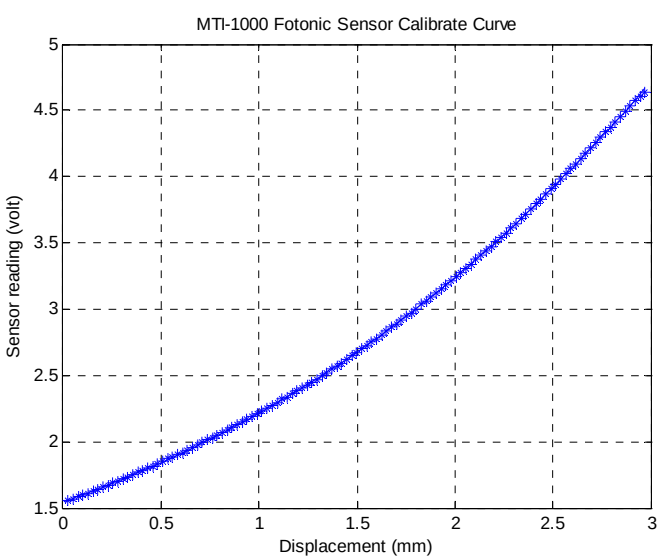

Figure 6.5 Calibration curve in the experiment.

6.2.2 NI PCI-6024E Data Acquisition Card

The National Instrument PCI-6024E Data Acquisition (DAQ) card is plug and play compatible multifunction analog, digital, and timing I/O card for the Peripheral Component Interconnect (PCI) bus computers. It features 12-bit analog-to-digital converters (ADCs) with 16 single-ended or 8 differential analog inputs, 12-bit DACs with 2 analog outputs, 8 digital I/O lines, and two 24-bit counter/timers for timing I/O. The maximum input signal range of the 12-bit cards is -10V to 10 V in bipolar mode. The maximum sampling rate that can be guaranteed is 200kS/s. The voltage output ranges from -10V to 10V. The maximum update rate is 1kHz and system dependent (National Instrument Corp., 2005).

The displacement of solenoid plunger measured by the fiber-optic probe is read and stored in LabVIEW by an analog input channel with range $\pm 10V$. LabVIEW generates the control signals for each solenoid and drives the power amplifier via two analog voltage outputs. The dual solenoids are driven by these control commands after power amplifiers. The sampling rate is set to 500Hz for all of the experiments on the dual solenoid positioning system because of the limitation of update rate of analog output of PCI-6024E DAQ card.

6.2.3 LabVIEW

LabVIEW, which is short for Laboratory Virtual Instrument Engineering Workbench produced by National Instrument, is a graphical programming language that uses icons instead of lines of text to create applications. A LabVIEW program is called a virtual instrument (VI) since it imitates the physical instrument. Each VI consists of the front

panel which simulates the user interface of the instrument, and the block diagram which includes the graphical source code of the program. The front panel is composed of a set of tools and objects, and the block diagram resembles a data flowchart, as shown in Figure 6.6.

Utilizing LabVIEW programs have many advantages such as: the status of the dual solenoid system can be monitored in real time on the front panel, the graphical user interface, in real time; various controllers designed for the micro-positioner can be switched to each other quickly and easily while the system is running; and the corresponding parameters of feedforward and feedback controller can be tuned using keyboard and mouse on time.

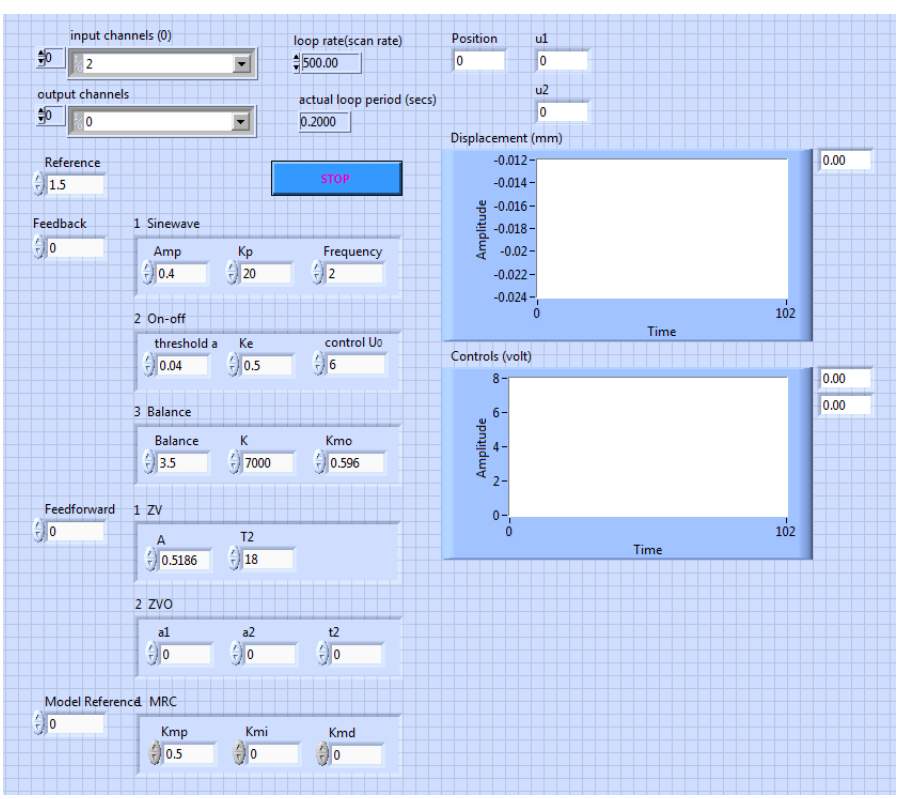

(a) Front panel

Figure 6.6 VI for dual solenoid positioning system.

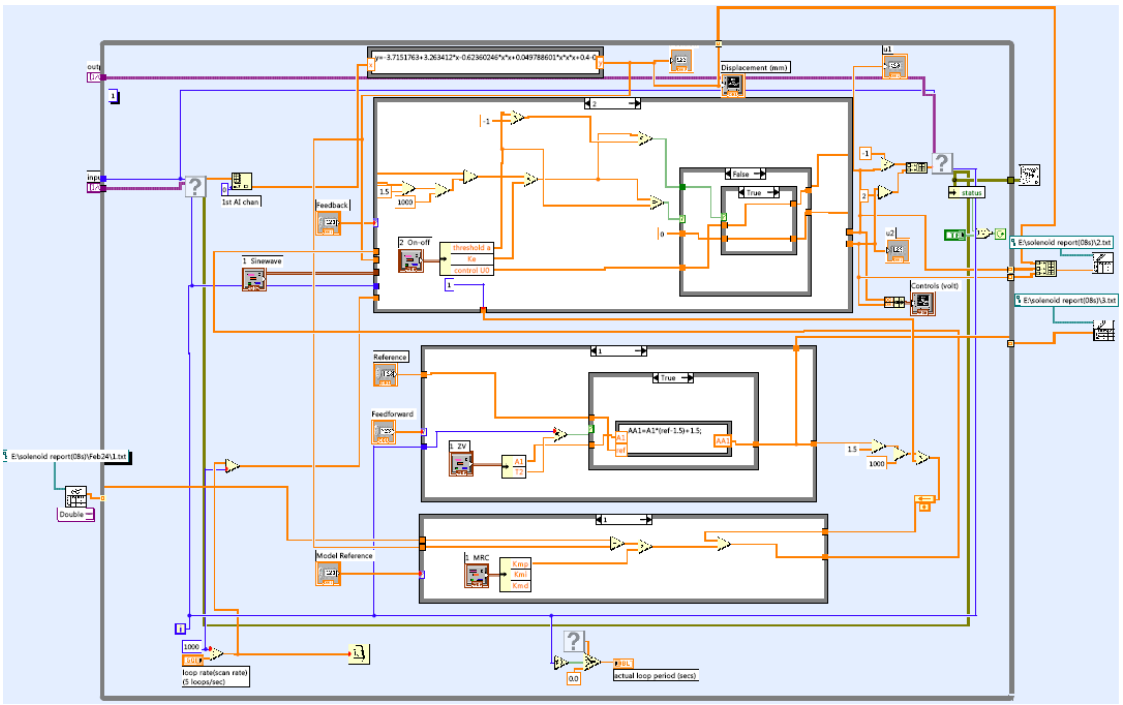

(b) Block diagram

Figure 6.6 VI for dual solenoid positioning system. (continued)

6.3 Cruciform Piezoelectric Nano-positioner

Figure 6.7 shows the 2-DOF cruciform piezoelectric actuator. The four edges of the cruciform PZT is fixed by a frame that is mounted on the heavy metal platform. To isolate vibration, the whole nano-positioner platform is mounted on an air floating table. The motions in x and y axes are represented by the change of distance between the target glued in the center of the piezoelectric actuator and the probes of the two ADE 3800 capacitance sensors respectively. Both of the positions of actuator and sensors can be tuned coarsely by the fixture.

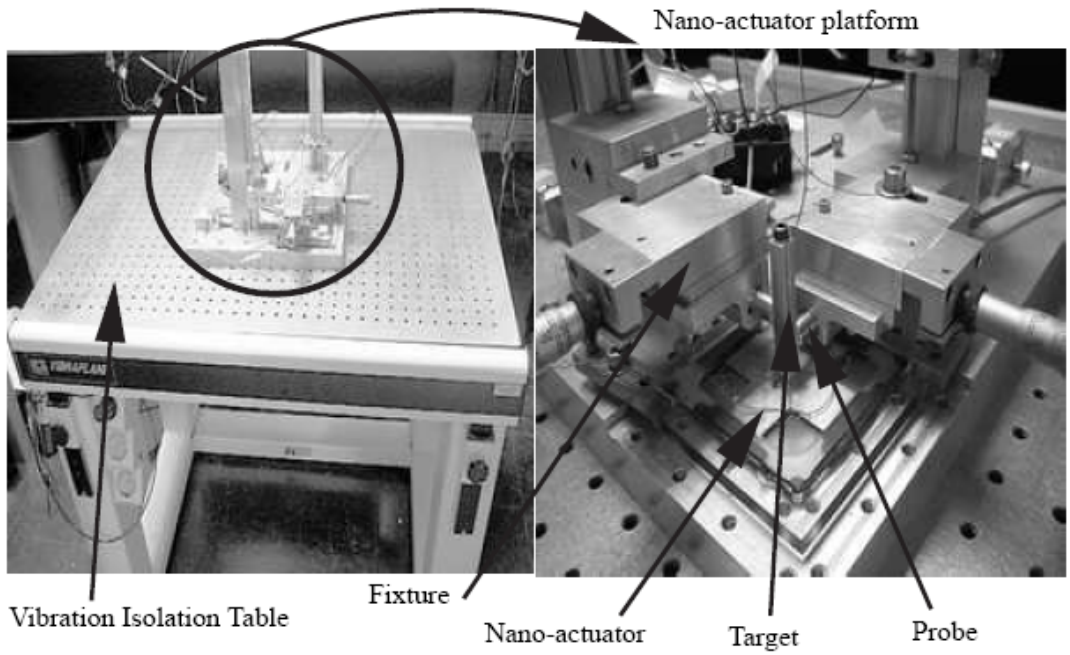

Figure 6.7 Picture of cruciform monolithic piezoelectric nano-actuator.

To implement the proposed control methods on the piezoelectric nano-positioner, the experimental setup which is composed by one 2-chanel Model 601C amplifiers, two ADE 3800 capacitance sensors and a real time operating system including TMS320C6416 DSK board, and PC, is shown in Figure 6.8.

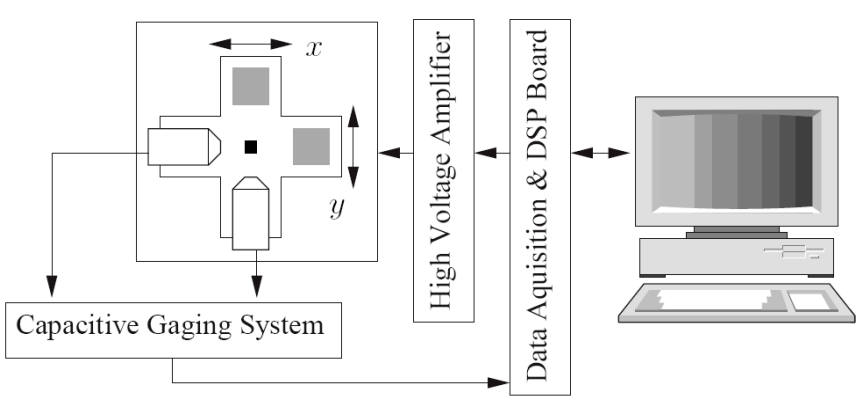

Figure 6.8 Experimental setup of piezoelectric nano-positioner.

6.3.1 Model 601C High Voltage Power Amplifiers

Model 601C dual channel high voltage amplifier produced by TREK Incorporated has the properties listed in Table 6.1. In this work, the output voltage is chosen in bipolar mode. The input voltage is DC. The detailed information is described in the Operator's Manual (2005).

Table 6.1 Properties of Model 601C High Voltage Amplifier

Input voltage range	$[0, \pm 10]$ VDC, or peak AC
DC voltage gain	100V/V
Output voltage range	$[0, \pm 1000]$ volts in unipolar mode; $[-500, 500]$ volts in bipolar mode;
Output current range	$[0, \pm 10]$ *mA* DC, or $[0, \pm 20]$ *mA* peak AC
Bandwidth	30kHz

6.3.2 Capacitance Sensor

The ADE capacitance sensor measures and transfers the displacement into voltage. The linear ratio between the displacement and the voltage is $2.5 \mu m / volt$ (X. Sun in 2001). The resolution is 1nm, and the bandwidth can be changed among 10 Hz, 100 Hz, 1000 Hz, and 5000 Hz by plugging in proper jumpers. In the experimental setup, the bandwidth is 1000 Hz.

6.3.3 TMS320C6416 DSP Starter Kit

The TMS320C6416T DSP Starter Kit (DSK) is a low-cost standalone development platform that enables users to evaluate and develop applications for the TMS320C6416 Digital Signal Processor (DSP) produced by Texas Instruments. It also serves as a hardware reference design for the TMS320C6416T DSP. The key features of

TMS320C6416T DSK include: a Texas Instruments TMS320C6416T DSP operating at 1 GHz;16 Mbytes of SDRAM; 512 Kbytes of non-volatile Flash memory; 4 user accessible LEDs and DIP switches, and standard expansion connectors for daughter card use (Spectrum Digital Incorporated, 2003).

6.3.4 Code Composer Studio

Code Composer Studio software is a fully integrated development environment (IDE) supporting Texas Instruments DSP platforms. It integrates all host and target tools in a unified environment to simplify DSP system configuration and application design.

Code Composer Studio extends the basic code generation tools with a set of debugging and real-time analysis capabilities. Code development flow involves utilizing the C6000 code generation tools to aid in optimization rather than coding by hand in assembly. These advantages allow the compiler to do all the laborious work of instruction selection, parallelizing, pipelining, and register allocation (Texas Instrument, 2005).

CHAPTER 7

EXPERIMENTAL RESULTS

In this chapter, the control methods discussed previously are implemented in the ultra-high precision positioning system, which consists of dual solenoid micro-positioner and the PZT nano-positioner. The experimental data and relative analysis on dual solenoid positioning system and cruciform piezoelectric positioning system are given in section 7.1 and section 7.2 respectively.

7.1 Experimental Results on Dual Solenoid Micro-positioner

Two types of inner loop feedback controllers are considered for the dual solenoid actuator: on-off control and balance control whose experimental data are listed in subsections 7.1.1 and 7.1.2 respectively. To reduce the vibration, the feedforward controllers, called Zero Vibration input shaping, are designed according to the basic feedback loops. The relative experimental analyses are presented in subsections 7.1.3 and 7.1.4. To further improve the performance, such as the steady state error and the settling time, the experimental results of MRZVB and VMRZVB on the dual solenoid actuator are shown in 7.1.5 and 7.1.6. Finally, a summary is given in subsection 7.1.7.

As shown in Figure 4.2, the total travel range is $x = -1.5\times10^{-3} m \sim 1.5\times10^{-3} m$. For convenience, the displacement in this chapter is redefined as,

$$x' = x + 1.5\times10^{-3} m \tag{7.1}$$

Based on this new definition, the displacement equals to zero when the plunger touches the left end; while the displacement gets its maximum when the plunger touches the right end. In each experiment, the initial position is arbitrarily chosen as 0.85mm and the set point *r* is set as 1.80mm. Each test in this section is repeated three times to show the consistency. All the controllers mentioned above are implemented to dual solenoid micro-positioner using LabVIEW 8.0. The sampling rate is set as 500 Hz.

7.1.1 Experimental Results of On-off Control

The parameters of on-off controller in Equation (4.25) and (4.26) are chosen the same as the one in simulation:

$$a = 0.02 \times 10^{-3} m, \quad K_e = 0.5, \quad u_0 = 6 \text{ volts} \tag{7.2}$$

The step response of on-off control for a set point of 1.8mm is shown in Figure 7.1. It is noted that the repeatability of the response is not good. According to Figure 7.1, the Coulomb friction coefficient is identified as $F_c = 1.3N$.

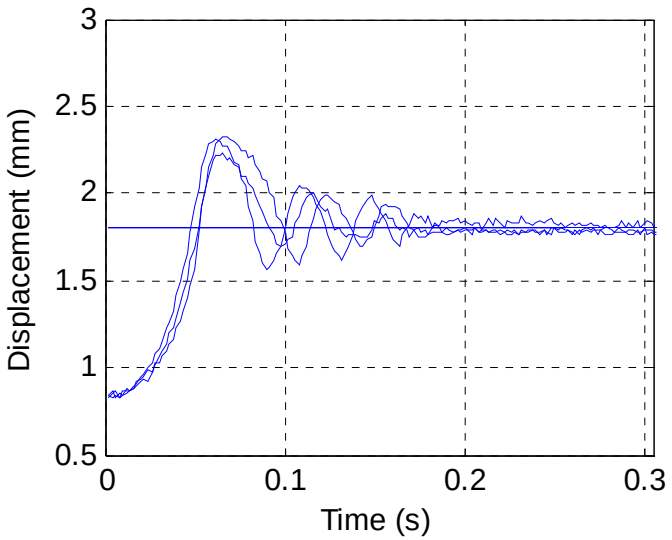

Figure 7.1 Step response of on-off control with 1.8mm set point (repeated 3 times).

7.1.2 Experimental Results of Zero Vibration On-off Control

Shown in Figure 7.2 is the step response of ZVOO control with a 1.8mm set point. Due to a slight mismatch between the model and the actual device, the ZV parameters are re-tuned for best results. The retuned parameters are shown in Table 7.1 where it is observed that except for t_2, parameters A_1 and A_2 are the same as the ones listed in Table 4.7. The slight increase in t_2 is due to a change of the experimental rise time.

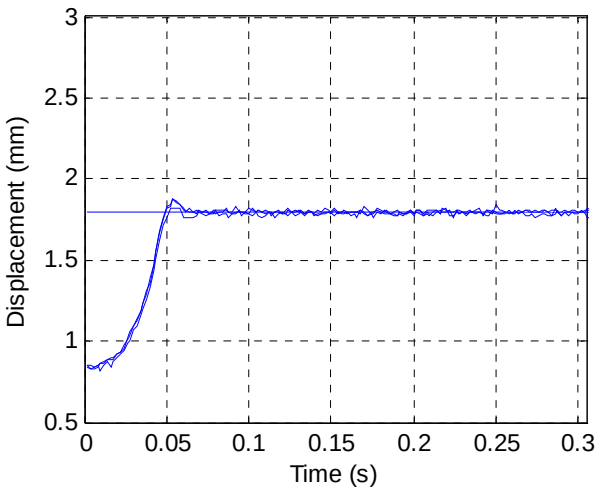

Figure 7.2 Step response of ZVOO control with 1.8mm set point (repeated 3 times).

Table 7.1 ZV Shaper Parameters (Experimental)

Set Point (mm)	**A_1** (mm)	**A_2** (mm)	**t_2** (s)
1.5	1.3117	0.1883	0.034
1.65	1.4182	0.2318	0.048
1.8	1.5248	0.2752	0.058

From Figure 7.2, it is observed that the ZVOO yields a settling time of 0.048 second while the steady error is 8 microns in average and 10 microns in standard deviation. It is found that the ZVOO control results in a ten fold reduction of overshoot and a three fold reduction of settling time compared to on-off control alone in subsection 7.1.1. Performance comparison between the on-off control and ZVOO control are summarized in Table 7.2 where it is observed that the ZVOO design produces better responses by reducing the vibration, overshoot, and steady state error significantly.

Table 7.2 Experimental Data Analysis (On-off Control and ZVOO)

	Overshoot (%)	**Settling time** (±10%) (s)	**Steady state** (mm)	**Mean of settling time** (±10%) (s)	**Mean of steady state** (mm)	**Deviation of steady state** (mm)
On-off	54.21	0.164	1.783	0.151	1.795	0.020
	55.79	0.165	1.823			
	46.00	0.124	1.780			
ZVOO	8.63	0.047	1.800	0.048	1.792	0.010
	8.00	0.049	1.790			
	2.32	0.048	1.785			

However, on-off feedback control introduces the parasitic term in the model (4.42), which leads to the changes of impulse time in ZVOO design compared with the conventional Zero Vibration shaper design. The control strategy changes according to the reference command and the initial conditions. The on-off control can not offer a consistent desired dynamic behavior for the feed forward controller.

7.1.3 Experimental Results of Balance Control

Figure 7.3 shows the experimental curves for the solenoid actuator with Balance controller (4.27), (4.28). The parameters of Balance control are set as

$$\text{Bal} = 4 \text{ volts}, \quad K = 7500, \quad K_{MO} = 0.8615 \tag{7.3}$$

The Coulomb friction is identified as $F_c = 0.72N$ which confirms that the friction may change with operating conditions and time.

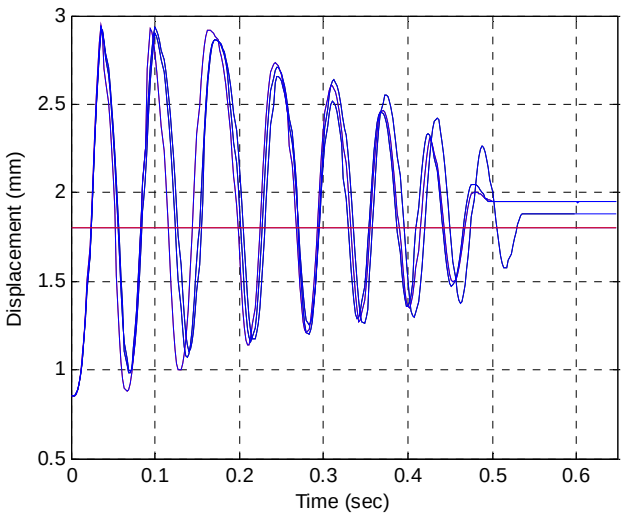

Figure 7.3 Step response of Balance control with 1.8 mm set point (repeated 3 times).

The solenoid system with balance controller is stable, but there is large vibration and overshoot in the step response. Large steady state error caused by the Coulomb friction in the dual solenoid system is another issue to be considered. For the dual solenoid micro-positioner with Balance control, further control actions are necessary to reduce the vibration and to compensate the Coulomb friction.

7.1.4 Experimental Results of Zero Vibration Balance Control

Figure 7.4 shows the experimental curves of the dual solenoid position system with ZV Balance control (Table 4.8, (4.27) ~ (4.28)). The parameters of Balance control are the same as section 7.1.3. It is noted that the levels of vibration and overshoot are reduced significantly compared to using Balance control only (Figure 7.3).

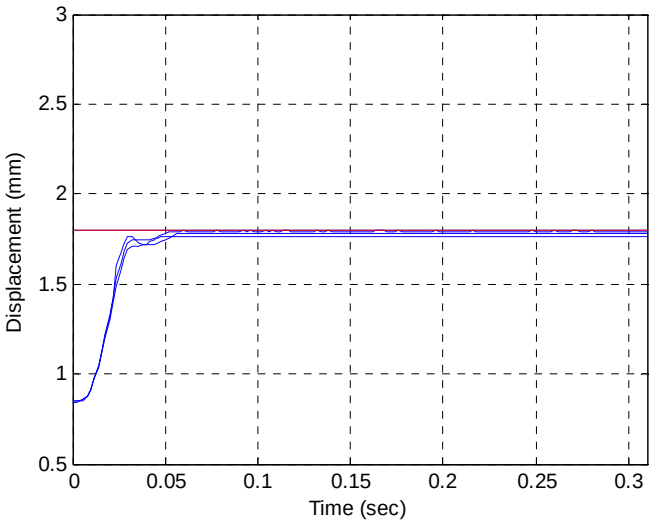

Figure 7.4 Step response of Zero Vibration Balance control with 1.8 mm set point (repeated 3 times).

Zero Vibration Balance control improves the performance of transient response. However, the steady state error, 23 microns on average introduced by the Coulomb friction, needs to be reduced for a high precision positioning system. It should be noted that the coulomb friction coefficient has been changed from 1.3N in Figure 7.1 to 0.72N in Figure 7.3. Therefore a more robust controller is necessary to compensate this nonlinear friction.

7.1.5 Experimental Results of Model Reference Zero Vibration Balance Control

The step response of MRZVB control is shown in Figure 7.5. The parameter of model reference control (4.50) is set to $k_{mp} = 0.2$, and the Balance control parameters and Zero vibration shaper parameters are listed in (7.3) and Table 4.8 respectively. Model reference feedback is applied to increase the robustness of the controller, and to compensate Coulomb friction.

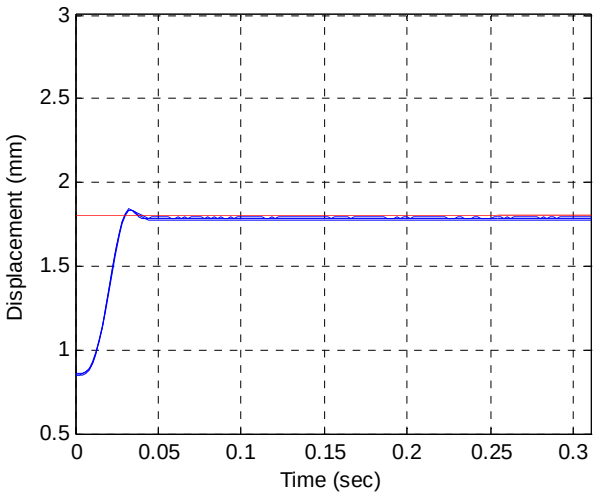

Figure 7.5 Step response of Model Reference Zero Vibration Balance control with 1.8 mm set point (repeated 3 times)..

Improvements on steady error, vibration suppression, and transient are quite visible. Table 7.3 is a summary of control performance analysis of the three controllers, Balance control, ZVB and MRZVB with set point 1.8mm. It is observed that the proposed MRZVB control produces the best overall performances.

Table 7.3 Experimental Data Analysis (Balance Control, ZVB and MRZVB, K=7500)

	Overshoot (%)	**Settling time (±2%)** (s)	**Steady state error** (mm)	**Mean of settling time** (±2%) (s)	**Mean of steady state error** (mm)	**Deviation of steady state error** (mm)
Balance	99.71	0.536	-0.084	0.5067	-0.1287	0.0316
	89.99	0.492	-0.149			
	89.85	0.492	-0.153			
ZVB	0.53	0.052	0.008	0.0393	0.0230	0.0122
	0.55	0.034	0.038			
	0.54	0.032	0.023			
MRZVB	4.67	0.032	0.008	0.0313	0.0163	0.0062
	6.33	0.032	0.018			
	6.36	0.030	0.023			

7.1.6 Experimental Results of Variable Model Reference Zero Vibration Balance Control

For this experiment, two additional cases are considered: slow and fast reference models. The relative speed of the linear reference model is obtained by varying K, as listed in Table 4.9. The experimental results are illustrated in Figure 7.6 ~ Figure 7.9. The performances of MRZVB control with fast and slow linear reference models are summarized in Table 7.4 and Table 7.5 respectively.

The linear reference model can be adjusted to obtain desired settling time systematically. Although the Zero Vibration shapers are not designed according to the identified plant, the model reference controller is able to drive the plant to track the desired dynamic behavior of the linear reference model. It is evident that in each case

(slow and fast) the VMRZVB design follows the reference model response and result in a 20% change in settling time from the slow to fast models.

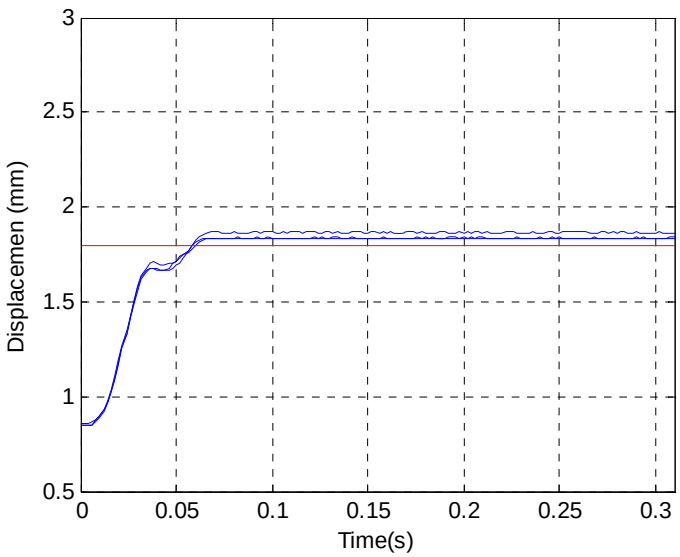

Figure 7.6 Step response of ZVB with slow reference model (K=6000, repeated 3 times).

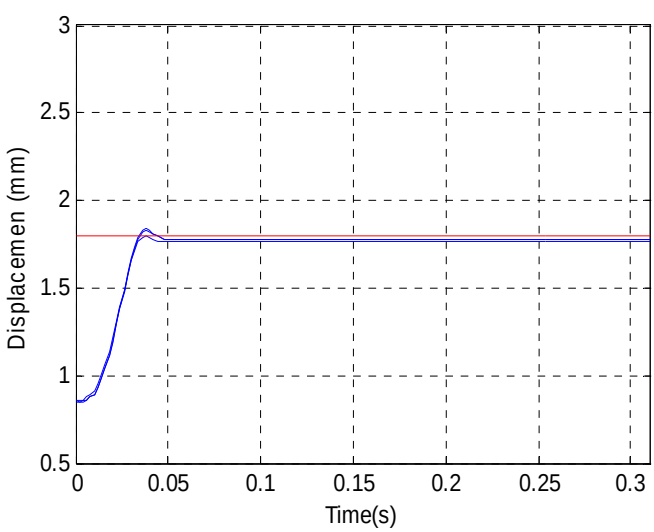

Figure 7.7 Step response of VMRZVB with slow reference model (K=6000, repeated 3 times).

Table 7.4 Experimental Data Analysis (ZVB and VMRZVB, K=6000).

	Overshoot (%)	**Settling time** (±2%) (s)	**Steady state error** (mm)	**Mean of settling time** (±2%) (s)	**Mean of steady state error** (mm)	**Deviation of steady state error** (mm)
ZVB	0.51	0.066	-0.036	0.0653	-0.045	0.0169
	0	0.066	-0.069			
	0	0.064	-0.031			
VMRZVB	5.29	0.036	0.023	0.0360	0.0247	0.0062
	5.79	0.036	0.018			
	3.27	0.036	0.033			

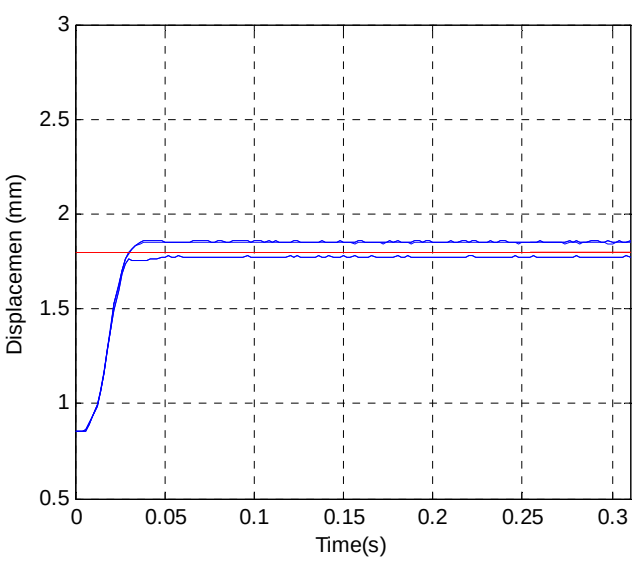

Figure 7.8 Step response of ZVB with fast reference model (K=9000, repeated 3 times).

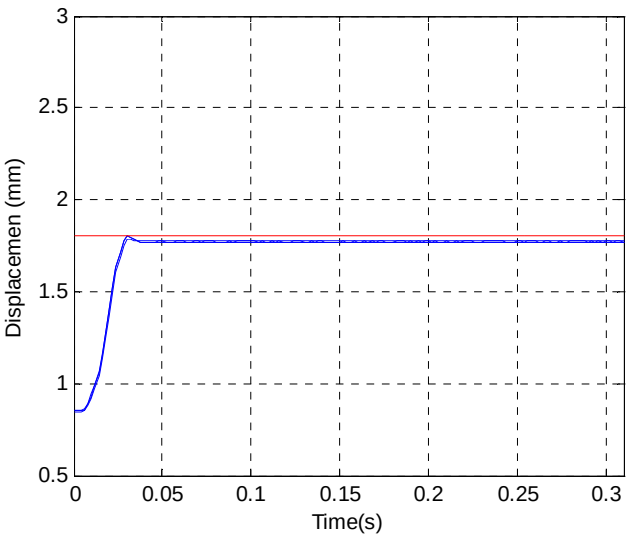

Figure 7.9 Step response of VMRZVB with fast reference model (K=9000, repeated 3 times).

Table 7.5 Experimental Data Analysis (ZVB and VMRZVB, K=9000)

	Overshoot (%)	**Settling time** ($\pm 2\%$) (s)	**Steady state error** (mm)	**Mean of Settling time** ($\pm 2\%$) (s)	**Mean of Steady state error** (mm)	**Deviation of steady state error**
ZVB	0.50	0.036	-0.046	0.0347	-0.023	0.0361
	0.50	0.036	-0.051			
	0.54	0.032	0.028			
VMRZVB	3.25	0.030	0.028	0.0307	0.0263	0.0024
	0.54	0.032	0.023			
	3.80	0.030	0.028			

7.2 Experimental Results on Piezoelectric Nano-positioner

Proportional control is considered as the inner loop feedback controller for piezoelectric nano-actuator. To reduce the vibration, a feedforward controller called Zero Vibration

input shaping is designed according to the basic feedback loop. The relative experimental analyses are presented in subsection 7.2.2. The experimental result of PI control is described in subsection 7.2.1 as comparison. To further improve the performance, such as the steady state error, the experimental results of MRZV on the cruciform piezoelectric nano-actuator are shown in subsection 7.2.3. Finally, a summary is given in subsection 7.2.4.

7.2.1 Experimental Results of PI Control

Table 7.6 lists the RMSE of the transient response of nanopositioner with various proportional and integral gains. The reference command and evaluation time are the same as simulation ones in subsection 5.2.1. Figure 7.10 indicates that the optimal-tuned PI control parameters based on the experimental results are $K_p = 0.3,$ and $K_i = 1000$, which differ from the simulated optimal parameters in Table 5.1. The difference could be induced by the existing un-modeled nonlinearities, and a mismatch between the linear model in Equation (5.3) and the actual device. Figure 7.11 is the step response of the actuator with optimal-tuned PI controller.

Table 7.6 RMSE of Step Response of Nano-positioner with Various PI Gains (Set Point $=1\ \mu m$)

		Proportional gain Kp				
		-0.5	0.1	0.3	0.5	5
Integral gain Ki	125	Unstable	0.4453	0.3912	0.4224	0.9839
	333	1.0072	0.2695	0.2415	0.2551	Unstable
	1000	0.6744	0.1645	0.1570	0.1573	Unstable
	3000	0.4668	0.4046	0.3957	0.4210	Unstable

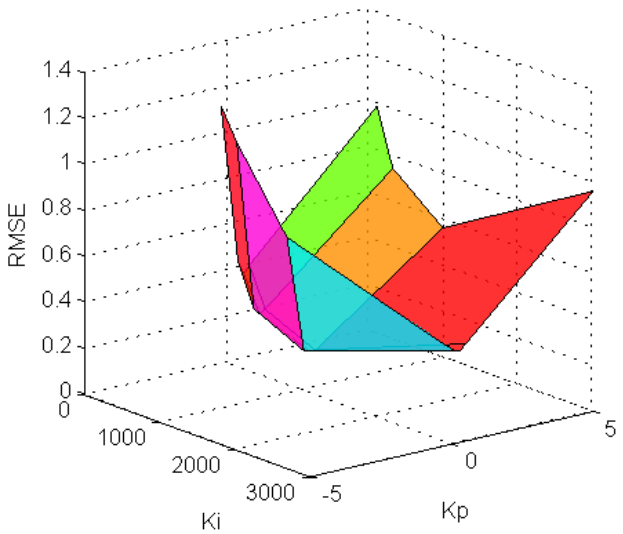

Figure 7.10 RMSE of piezoelectric nano-positioner response vs. various PI gains.

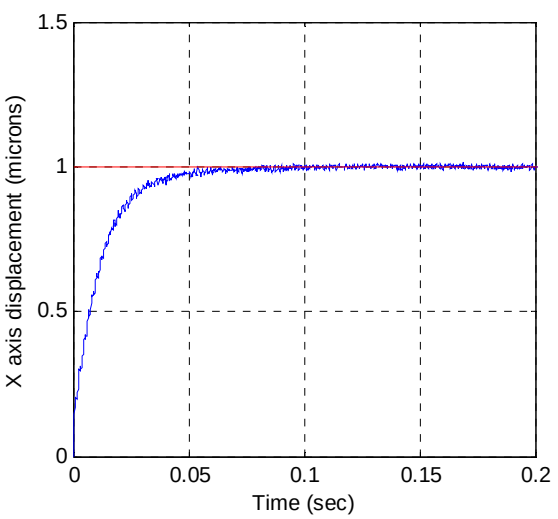

Figure 7.11 Step response of PI control on piezoelectric nano-positioner ($K_p = 0.3,\ K_i = 1000$, set point $= 1\ \mu m$).

7.2.2 Experimental Results of Zero Vibration Control

Figure 7.12 shows the experimental response of the piezoelectric actuator with single-mode ZV shaper designed according to the first vibration mode (Table 5.2, Equation (5.9)

and Equation (5.10)). It is observed that significant residual vibration is induced by the second vibration mode.

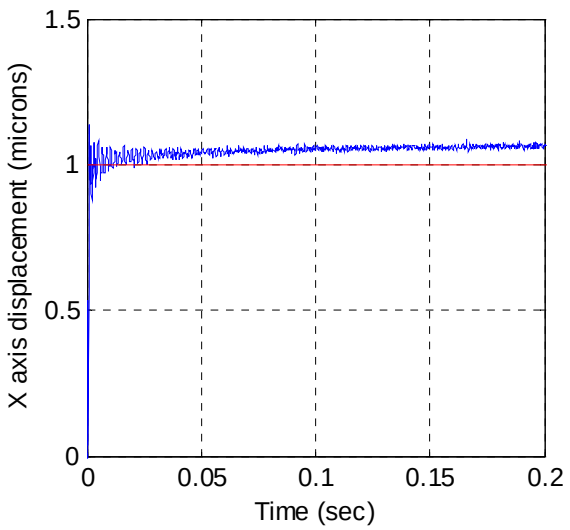

Figure 7.12 Step response of single mode ZV control on piezoelectric nano-positioner (set point= 1 μm).

Figure 7.13 shows the experimental response of the piezoelectric actuator with the 2-mode ZV control (Table 5.3, Equation (5.11)). The parameter of proportional control is the same as the one in model identification in Equation (5.4). It is noted that the levels of vibration and overshoot are reduced significantly compared to using single mode ZV shaper only (Figure 7.12). The settling time and RMSE are reduced compared to using optimal-tuned PI controller (Figure 7.11).

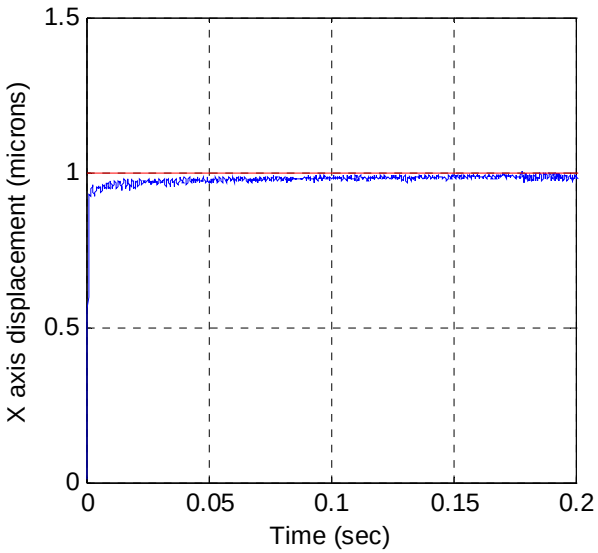

Figure 7.13 Step response of 2-mode ZV control on piezoelectric nano-positioner (set point= 1 μm).

However, the step response curves of 2-mode ZV control with set point 0.5 μm (Figure 7.14) and 1.2 μm (Figure 7.15) show larger steady state errors and residual vibration compared to the one with set point 1 μm shown in Figure 7.13. This is because the current ZV shaper is designed based on the linear model in Equation (5.4) identified with set point 1 μm. The nonlinearity exists in the cruciform piezoelectric nano-actuator such as hysteresis effect may change with the amplitude of the drive voltage. The mismatch between the plant and linear model (5.4) leads to the deterioration of performance.

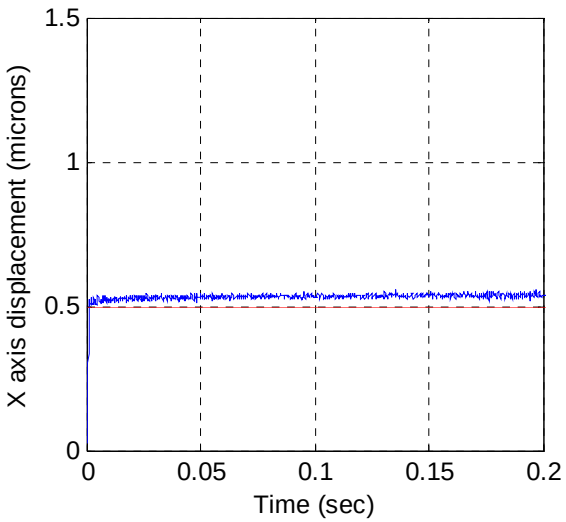

Figure 7.14 Step response of 2-mode ZV control on piezoelectric nano-positioner (set point=0.5 μm).

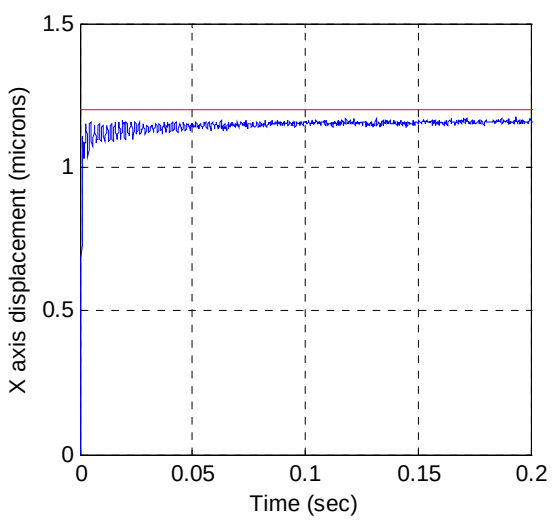

Figure 7.15 Step response of 2-mode ZV control on piezoelectric nano-positioner (set point= 1.2 μm).

7.2.3 Experimental Results of Model Reference Zero Vibration Control

Shown in Figure 7.16 and 7.17 are the step response curves of MRZV control with various set points. Performance comparison among PI control, 2-mode ZV control, and MRZV control are summarized in Table 7.7. The settling time, RMSE, and steady state

error of the step response are chosen as the performance evaluation parameters. Each test was repeated three times to evaluate the corresponding control strategy statistically. The Standard Deviation (Std. Dev.) of RMSE is calculated according to Equation (7.4).

$$Std.Dev.(y_{rms}) = \sqrt{\frac{\sum_{i=1}^{3}(y_{rms}(i) - \overline{y}_{rms})^2}{3}} \tag{7.4}$$

In Equation (7.4), $\overline{y}_{rms}$ is the mean of RMSE y_{rms} achieved by the applied control method with specified set point. It is observed that the MRZV control improves the robustness and produces the best overall performances by reducing the RMSE, settling time, vibration and steady state error significantly. Take experimental data of set point $0.5\,\mu m$ as example, it is observed that 2-mode ZV yields an average settling time of 1.5 millisecond, which is a twenty fold reduction of settling time compared with conventional PI control. However, the mean of steady state error, 23.2 nanometers, needs to be improved for a nanopositioner. This may be caused by the existing un-modeled nonlinearities of this ultrahigh precision nanopositioner, and a slight parameter mismatch between the linear model and the actual device. MRZV introduces the model reference controller to improve the robustness of existing shaping method. The steady state error is 0.2 nanometer in average, and 0.4 nanometer in standard deviation; while the settling time is even shorter than 2-mode ZV shaper alone. It is also found that the MRZV control results in a four fold reduction of RMSE vs. PI. Table 7.7 indicates that the MRZV control improves the robustness and produces the best overall performances by reducing the RMSE, settling time, vibration and steady state error significantly.

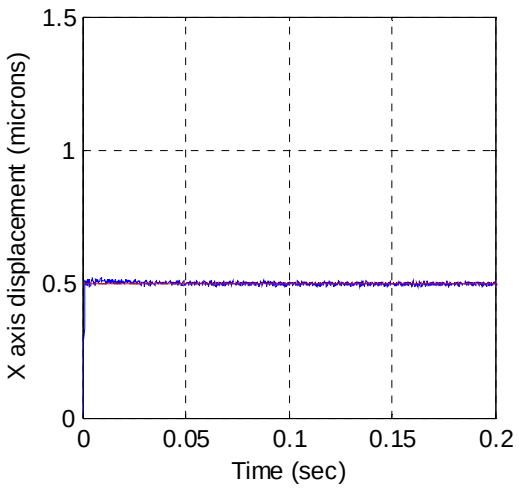

Figure 7.16 Step response of MRZV control Step response of 2-mode ZV control on piezoelectric nano-positioner (set point= $0.5\,\mu m$).

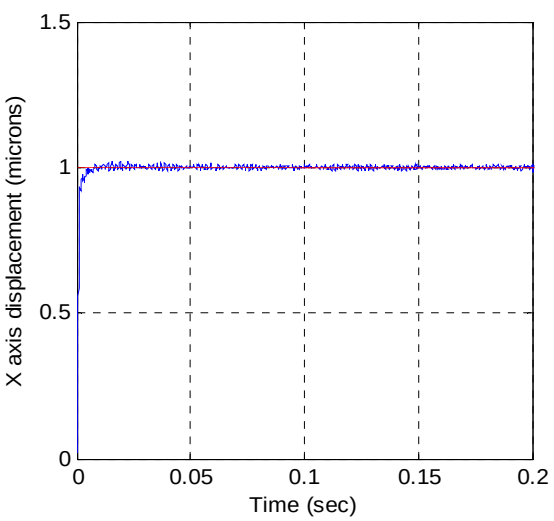

Figure 7.17 Step response of MRZV control on piezoelectric nano-positioner (set point=$1\,\mu m$).

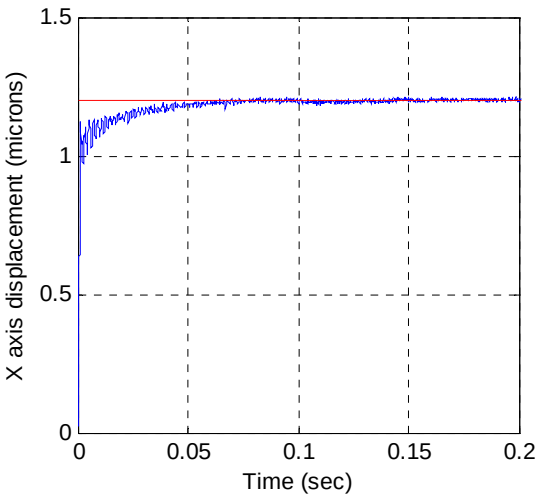

Figure 7.18 Step response of MRZV control on piezoelectric nano-positioner (set point=1.2 μm).

Table 7.7 Experimental Data Analysis on Piezoelectric Nano-positioner

Set point (μm)	**Control method**	**Mean of RMSE (μm)**	**Mean of settling time ($\pm 5\%$)** (s)	**Mean of steady state error** (μm)	**Deviation of steady state error**	**Deviation of RMSE**
0.5	PI	0.0821	0.0355	0.0002	0.0007	0.0004
	2-mode ZV	0.0384	0.0015	0.0232	0.0002	0.0066
	MRZV	0.0273	0.0013	0.0002	0.0004	0.0003
1	PI	0.1645	0.0416	0.0005	0.0019	0.0037
	2-mode ZV	0.0577	0.0025	-0.0165	0.0005	0.0027
	MRZV	0.0485	0.0020	-0.0002	0.0008	0.0003
1.2	PI	0.2010	0.0495	-0.0021	0.0080	0.0036
	2-mode ZV	0.1125	0.0188	-0.0473	0.0071	0.0392
	MRZV	0.0751	0.0318	0.0044	0.0024	0.0062

Figure 7.19 shows the hysteresis effect when driving the open loop nanopositioner. Compared to the similar test results MRZV control shown in Figure 7.20, the adverse effect of hysteresis has been reduced significantly.

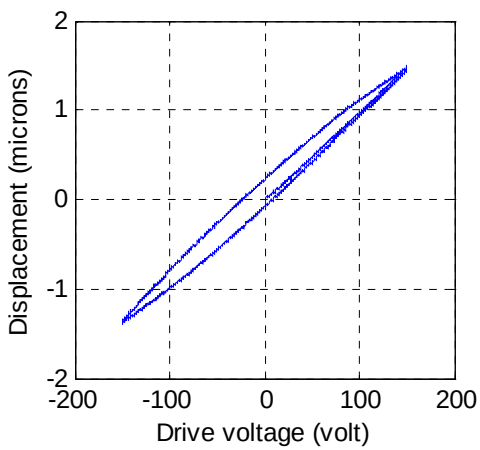

Figure 7.19 Hysteresis effect on the open loop nanopositioner.

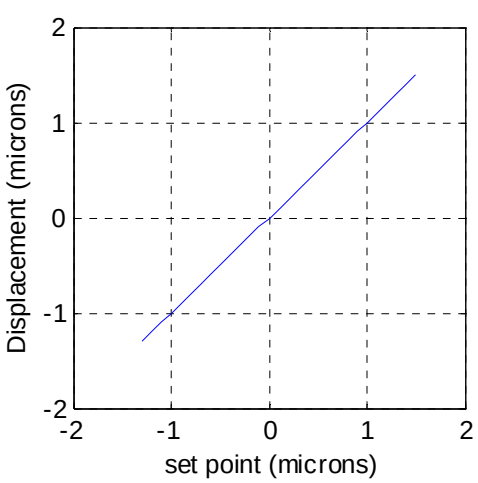

Figure 7.20 Steady state of MRZV control with various set points on piezoelectric nano-positioner.

CHAPTER 8

SUMMARY AND FUTURE WORK

This work presents a controller design approach Variable Model Reference Zero Vibration (VMRZV) for improving the speed and accuracy of the positioning system by attenuating the adverse effects of micro-/nano-positioning actuator's uncertainties and oscillatory command-induced transients.

The proposed positioner comprises of two push-pull dual solenoid actuators and a cruciform piezoelectric actuator. It is capable of meeting multiple DOF high precision positioning requirements with a wide range of applications. In this work, dynamic models of the dual solenoid actuator and piezoelectric nano-positioner are first derived. Basic feedback strategies, Balance control and On-off control are designed to realize positioning control of the dual solenoid micro-positioner. The parameters of the high nonlinear dynamics of the dual solenoid actuator are identified correspondingly based on the experimental data of solenoid actuator with the inner feedback algorithms. Similarly, Proportional control and PI control are designed to control the cruciform piezoelectric nano-positioner. The parameters of this equivalent 4^{th} order linear model of such piezoelectric nano-positioner are defined according to the step response of the plant with proportional feedback. However, the primary nonlinear parasitic existed in both actuators include Coulomb friction which is time varying and uncertain. The presence of friction affects the further feedforward controller design, ZV shaper in this work, which can be confirmed in the experimental data of ZVB and ZVOO on the dual solenoid micro-positioner, and ZVP on the piezoelectric nano-positioner.

Conventional friction compensation methods based on estimation or cancellation tend to experience performance limitations. Using the proposed Variable Model Reference Zero Vibration control, it is shown that the effects of friction can be asymptotically attenuated, resulting in better steady state accuracy and repeatability. Combined with the zero vibration command shaper, significant improvement on the speed of response can be obtained. For the dual solenoid system, a novel balance control strategy is introduced to obtain an equivalent linear model through which the VMRZV control is based on. Simulation results and experimental data confirm that the control method proposed is effective and practical. Dynamic structure of the nano-positioner is similar: oscillatory dynamics along with nonlinear characteristics that can hardly be modeled precisely enough at the nanometer scale, for example, solid friction and other parasitics. The same design methodology based on MRZV which combines the advantages of model reference and input shaping is also applied to obtain the necessary performance improvement. MRZV improves the transient response and steady state error of this cruciform piezoelectric actuator without requiring the explicit knowledge of an accurate model of the parasitic nonlinearities. Experimental results confirm the effectiveness and practicality of high precision positioning actuator with proposed model reference control method.

Analytical development to-date includes: the piecewise analytical solution of the step response of model reference controller on the plant with Coulomb friction is obtained in equations (3.49) ~ (3.51); the error between the plant with MRC and the reference model is presented in equation (3.48). Furthermore, it is proven that under the MRZV control, the error between the reference model and plant with nonlinear friction

can be reduced successfully with increase of model reference control gain k_{mp} as shown in equation (3.63). The residual vibration exhibits a cyclic characteristics which may be exploited as performance enhancement without the use of extremely high gain k_{mp}.

Based on the current studies, the near future work of interest is testing the performance of integrated ultra-high precision positioning system, which consists of dual solenoid micro-positioner and PZT nano-positioner in Figure 6.1.

APPENDIX A

PROOF OF THEOREM 3.1

Theorem 3.1: See Chapter 3.

Proof: Substituting reference model (3.41) into (3.44), the response of positioning system with MRZV controller can be solved piece wisely.

$$\frac{dv}{dt}=\begin{cases}-2\zeta_m\omega_m v(t)-\left(1+k_{mp}\right)\omega_m^2 y(t)+\left(\omega_m^2 r-F_c\right)\cdot H(t)+k_{mp}\omega_m^2 y_m(t), & v>0;\\ -2\zeta_m\omega_m v(t)-\left(1+k_{mp}\right)\omega_m^2 y(t)+\omega_m^2 r\cdot H(t)+k_{mp}\omega_m^2 y_m(t), & v=0;\\ -2\zeta_m\omega_m v(t)-\left(1+k_{mp}\right)\omega_m^2 y(t)+\left(\omega_m^2 r+F_c\right)\cdot H(t)+k_{mp}\omega_m^2 y_m(t), & v<0.\end{cases} \tag{a.1}$$

(1) It is assumed that the system has positive speed in the time interval $\left[\overline{t}_i,\overline{t}_{i+1}\right)$, the system is rewritten as shown in equation (a.2) ~ (a.4) based on superposition property.

$$\frac{d^2x_1\left(t-\overline{t}_i\right)}{dt^2}=-2\zeta_m\omega_m\frac{dx_1\left(t-\overline{t}_i\right)}{dt}-\left(1+k_{mp}\right)\omega_m^2 x_1(t-\overline{t}_i)-F_c\cdot H(t-\overline{t}_i) \tag{a.2}$$

$$\begin{aligned}\frac{d^2x_2(t-\overline{t}_i)}{dt^2}=&-2\zeta_m\omega_m\frac{dx_2(t-\overline{t}_i)}{dt}-\left(1+k_{mp}\right)\omega_m^2 x_2(t-\overline{t}_i)+\omega_m^2 r\cdot H(t-\overline{t}_i)\\&+k_{mp}\omega_m^2 y_m(t-\overline{t}_i)\end{aligned} \tag{a.3}$$

$$y(t-\overline{t}_i)=x_1(t-\overline{t}_i)+x_2(t-\overline{t}_i) \tag{a.4}$$

In which $x_1(t)$ represents the system response which is related to the Coulomb friction; $x_2(t)$ represents the system response related to the reference command. The initial conditions at time zero can be set as follows without loss of generality, since the initial conditions of the whole system are all zero.

$$\begin{aligned} x_1(0) &= 0, \qquad & v_1(0) &= \frac{dx_1(0)}{dt} = 0, \\ x_2(0) &= 0, \qquad & v_2(0) &= \frac{dx_2(0)}{dt} = 0. \end{aligned} \tag{a.5}$$

If the initial conditions $x_1(\bar{t}_{i+1}),$ and $v_1(\bar{t}_{i+1})$ are known, the solution of differential equation (a.2) is shown in equation (a.6).

$$\begin{aligned} x_1(t-\bar{t}_i) = &\sqrt{\frac{F_c^2 + 2\zeta_m\omega_m F_c v_1(\bar{t}_i^-) + 2F_c(1+k_{mp})\omega_m^2 x_1(\bar{t}_i^-)}{(1+k_{mp})\omega_m^4(1+k_{mp}-\zeta_m^2)} + x_1^2(\bar{t}_i^-) + \frac{\left[x_1(\bar{t}_i^-)\zeta_m\omega_m + v_1(\bar{t}_i^-)\right]^2}{\omega_m^2(1+k_{mp}-\zeta_m^2)}} \\ &\times e^{-\zeta_m\omega_m(t-\bar{t}_i)}\sin\left[\omega_m\sqrt{1+k_{mp}-\zeta_m^2}\,(t-\bar{t}_i)+\theta(i)\right] - \frac{F_c}{(1+k_{mp})\omega_m^2}H(t-\bar{t}_i), \\ &\qquad\qquad t\in[\bar{t}_i,\bar{t}_{i+1}), \quad i=0,1,2,... \end{aligned} \tag{a.6}$$

in which

$$\theta(i) = tg^{-1}\left\{\frac{x_1(\bar{t}_i^-) + \dfrac{F_c\,\mathrm{sgn}(\bar{t}_i)}{(1+k_{mp})\omega_m^2}}{\dfrac{x_1(\bar{t}_i^-)\zeta_m\omega_m + v_1(\bar{t}_i^-)}{\omega_m\sqrt{1+k_{mp}-\zeta_m^2}} + \dfrac{\zeta_m F_c\,\mathrm{sgn}(\bar{t}_i)}{(1+k_{mp})\omega_m^2\sqrt{1+k_{mp}-\zeta_m^2}}}\right\} \tag{a.7}$$

The corresponding velocity is

$$\frac{dx_1}{dt}(t-\bar{t}_i)=\frac{F_c}{\omega_m\sqrt{1+k_{mp}-\zeta_m^2}}e^{-\zeta_m\omega_m(t-\bar{t}_i)}\sin\left[\omega_m\sqrt{1+k_{mp}-\zeta_m^2}\,(t-\bar{t}_i)\right]$$
$$+\frac{\sqrt{1+k_{mp}}\sqrt{v_1(\bar{t}_i^{-})^2+2\zeta_m\omega_m x_1(\bar{t}_i^{-})v_1(\bar{t}_i^{-})+x_1^2(\bar{t}_i^{-})\left(1+k_{mp}\right)\omega_m^2}}{\sqrt{1+k_{mp}-\zeta_m^2}}e^{-\zeta_m\omega_m(t-\bar{t}_i)} \quad \text{(a.8)}$$
$$\times\sin\left[\omega_m\sqrt{1+k_{mp}-\zeta_m^2}\,(t-\bar{t}_i)+tg^{-1}\frac{x_1(\bar{t}_i^{-})\omega_m\sqrt{1+k_{mp}-\zeta_m^2}}{\zeta_m\omega_m x_1(\bar{t}_i^{-})+v_1(\bar{t}_i^{-})}-tg^{-1}\frac{\sqrt{1+k_{mp}-\zeta_m^2}}{\zeta_m}\right],$$
$$t\in\left[\bar{t}_i,\bar{t}_{i+1}\right),\qquad i=0,1,2,3...$$

(2) Assume that the system has negative speed in the time interval $\left[\bar{t}_{i+1},\bar{t}_{i+2}\right)$, the system is rewritten as the summation of differential equations (a.9) ~ (a.11).

$$\frac{d^2x_1(t-\bar{t}_{i+1})}{dt^2}=-2\zeta_m\omega_m\frac{dx_1(t-\bar{t}_{i+1})}{dt}-\left(1+k_{mp}\right)\omega_m^2x_1(t-\bar{t}_{i+1})+F_c\cdot H(t-\bar{t}_{i+1}) \quad \text{(a.9)}$$

$$\frac{d^2x_2(t-\bar{t}_{i+1})}{dt^2}=-2\zeta_m\omega_m\frac{dx_2}{dt}(t-\bar{t}_{i+1})-\left(1+k_{mp}\right)\omega_m^2x_2(t-\bar{t}_{i+1})+\omega_m^2r\cdot H(t-\bar{t}_{i+1})$$
$$+k_{mp}\omega_m^2x_m(t-\bar{t}_{i+1}) \quad \text{(a.10)}$$

$$y(t-\bar{t}_{i+1})=x_1(t-\bar{t}_{i+1})+x_2(t-\bar{t}_{i+1}) \quad \text{(a.11)}$$

Similar to condition (1), differential equations (a.9) is solved with known initial conditions $x_1(\bar{t}_{i+1})$, and $v_1(\bar{t}_{i+1})$.

$$
\begin{aligned}
x_1(t-\overline{t}_{i+1}) = & \sqrt{\frac{F_c^2 - 2\zeta_m\omega_m F_c v_1\left(\overline{t}_{i+1}^-\right) - 2F_c\left(1+k_{mp}\right)\omega_m^2 x_1\left(\overline{t}_{i+1}^-\right)}{\left(1+k_{mp}\right)\omega_m^4\left(1+k_{mp}-\zeta_m^2\right)} + x_1{}^2\left(t_i^-\right)} \\
& + \frac{\left[x_1\left(\overline{t}_{i+1}^-\right)\zeta_m\omega_m + v_1\left(\overline{t}_{i+1}^-\right)\right]^2}{\omega_m^2\left(1+k_{mp}-\zeta_m^2\right)} \\
& \times e^{-\zeta_m\omega_m\left(t-\overline{t}_{i+1}\right)}\sin\left[\omega_m\sqrt{1+k_{mp}-\zeta_m^2}\left(t-\overline{t}_{i+1}\right)+\theta(i+1)\right] \\
& + \frac{F_c}{\left(1+K_{mp}\right)\omega_m^2}H(t-\overline{t}_{i+1}), \\
& \qquad\qquad t\in\left[\overline{t}_{i+1},\overline{t}_{i+2}\right), \quad i=0,1,2,...
\end{aligned}
\tag{a.12}
$$

In which

$$
\theta(i+1) = tg^{-1}\left\{\frac{x_1\left(\overline{t}_{i+1}^-\right)+\dfrac{F_c\,\mathrm{sgn}(\overline{t}_{i+1})}{\left(1+k_{mp}\right)\omega_m^2}}{\dfrac{x_1\left(\overline{t}_{i+1}^-\right)\zeta_m\omega_m + v_1\left(\overline{t}_{i+1}^-\right)}{\omega_m\sqrt{1+k_{mp}-\zeta_m^2}} + \dfrac{\zeta_m F_c\,\mathrm{sgn}(\overline{t}_{i+1})}{\left(1+k_{mp}\right)\omega_m^2\sqrt{1+k_{mp}-\zeta_m^2}}}\right\}
\tag{a.13}
$$

And the speed is

$$
\begin{aligned}
\frac{dx_1(t-\overline{t}_{i+1})}{dt} = & -\frac{F_c}{\omega_m\sqrt{1+k_{mp}-\zeta_m^2}}e^{-\zeta_m\omega_m(t-\overline{t}_{i+1})}\sin\left[\omega_m\sqrt{1+k_{mp}-\zeta_m^2}\left(t-\overline{t}_{i+1}\right)\right] \\
& + \frac{\sqrt{1+k_{mp}}\sqrt{v_1(\overline{t}_{i+1}^-)^2 + 2\zeta_m\omega_m x_1(\overline{t}_{i+1}^-)v_1(\overline{t}_{i+1}^-) + x_1^2(\overline{t}_{i+1}^-)\left(1+k_{mp}\right)\omega_m^2}}{\sqrt{1+k_{mp}-\zeta_m^2}}e^{-\zeta_m\omega_m(t-\overline{t}_{i+1})} \\
& \times\sin\left[\omega_m\sqrt{1+k_{mp}-\zeta_m^2}\left(t-\overline{t}_{i+1}\right)+tg^{-1}\frac{x_1(\overline{t}_{i+1}^-)\omega_m\sqrt{1+k_{mp}-\zeta_m^2}}{\zeta_m\omega_m x_1(\overline{t}_{i+1}^-)+v_1(\overline{t}_{i+1}^-)}-tg^{-1}\frac{\sqrt{1+k_{mp}-\zeta_m^2}}{\zeta_m}\right], \\
& \qquad\qquad t\in\left[\overline{t}_{i+1},\overline{t}_{i+2}\right), \qquad i=0,1,2,3...
\end{aligned}
\tag{a.14}
$$

$x_2(t)$ is solved according to equation (a.3) and (a.10) which is the same as the step response of reference model:

$$x_2(t) = r\left[1 - \frac{e^{-\zeta_m \omega_m t}}{\sqrt{1-\zeta_m^2}} \sin\left(\omega_m \sqrt{1-\zeta_m^2}\, t + \mathrm{tg}^{-1} \frac{\sqrt{1-\zeta_m^2}}{\zeta_m}\right)\right] \tag{a.15}$$

$$v_2(t) = \frac{r\omega_m}{\sqrt{1-\zeta_m^2}} e^{-\zeta_m \omega_m t} \sin\left(\omega_m \sqrt{1-\zeta_m^2}\, t\right) \tag{a.16}$$

Equation (a.15) further implies that the error between the system with model reference controller and the reference model is represented by equation (a.17).

$$\begin{aligned} err(t) &= y_m(t) - x_1(t) - x_2(t) \\ &= -x_1(t) \end{aligned} \tag{a.17}$$

$$v_{err}(t) = -v_1(t) \tag{a.18}$$

Summarizing equations (a.6) ~ (a.7), (a.12)~(a.13), and (a.17), the error between the reference model and the plant with Coulomb friction, and the step response of the plant with model reference controller are represented in equations (3.48)~(3.51) (proof end).

APPENDIX B

PHASE PLANE DIAGRAM

The dynamic behavior of the error between the reference model and the plant with friction uncertainty is concluded in Equation (3.55).

$$\begin{aligned} \frac{de_y}{dt} &= e_v \\ \frac{de_v}{dt} &= -\omega_m^2\left(1+k_{mp}\right)e_y - F_c \operatorname{sgn}\left[e_v(t)+v_m(t)\right] \end{aligned} \tag{3.55}$$

(1) If $v_{err}(t) > -v_m(t)$, The error dynamic equation can be written as Equations (b.1) and (b.2).

$$\frac{de_y}{dt} = e_v \tag{b.1}$$

$$\frac{de_v}{dt} = -\omega_m^2\left(1+k_{mp}\right)e_y - F_c \tag{b.2}$$

The solution of Equations (b.1) and (b.2) is in Equation (b.3).

$$e_v(t) = -\frac{F_c}{\omega_m\sqrt{1+k_{mp}}}\sin\left(\omega_m\sqrt{1+k_{mp}}\,t\right) \tag{b.3}$$

Dividing Equation (b.2) by (b.1) gets

$$\frac{de_v}{de_y} = -\omega_m^2\left(1+k_{mp}\right)\frac{e_y}{e_v} - \frac{F_c}{e_v} \tag{b.4}$$

which can be rewritten as Equation (b.5).

$$e_v de_v = -\left[\omega_m^2\left(1+k_{mp}\right)e_y + F_c\right]de_y \tag{b.5}$$

The solution for phase plane path is achieved by integrating Equation (b.5) on both sides:

$$e_v^2 + \omega_m^2(1+k_{mp})\left[e_y + \frac{F_c}{\omega_m^2(1+k_{mp})}\right]^2 = 2C + \frac{F_c^2}{\omega_m^2(1+k_{mp})} \qquad \text{(b.6)}$$

In Equation (b.6), C is a constant induced by integration. The phase plane diagram is a family of ellipses with the center at $\left(-\frac{F_c}{\omega_m\sqrt{1+k_{mp}}}, 0\right)$.

To simplify the solution in Equation (b.6), Equation (3.57) is defined as follow:

$$\bar{e}_y = \omega_m\sqrt{1+k_{mp}}\,e_y \qquad \text{(3.57)}$$

The corresponding phase diagram plotted as e_v against $\bar{e}_y$ are circular paths in Equation (3.56).

$$e_v^2 + \left(\bar{e}_y + \frac{F_c}{\omega_m\sqrt{1+k_{mp}}}\right)^2 = \bar{C} \qquad \text{(3.56)}$$

The constant $\bar{C}$ is expressed in Equation (b.7).

$$\bar{C} = 2C + \frac{F_c^2}{\omega_m^2(1+k_{mp})} \qquad \text{(b.7)}$$

(2) If $e_v(t) < -v_m(t)$, the dynamic of the error follows Equation (b.8).

$$\begin{aligned} \frac{de_y}{dt} &= e_v \\ \frac{de_v}{dt} &= -\omega_m^2\left(1+k_{mp}\right)e_y + F_c \end{aligned} \qquad \text{(b.8)}$$

The phase plane curves are family of ellipses with the center at $\left(\frac{F_c}{\omega_m\sqrt{1+k_{mp}}}, 0\right)$ show in Figure 3.9.

$$e_v^2 + \left(\overline{e}_y - \frac{F_c}{\omega_m \sqrt{1+k_{mp}}} \right)^2 = \overline{C} \tag{3.58}$$

REFERENCES

1. Abelmann, L., Bolhuis, T., Hoesum, A. M., Krijnen, G. J. M., & Lodder, J. C. (2003). Large capacity probe recording using storage robots. IEE Proceedings: Science, Measurement and Technology, Vol. 150, No. 5, 218–221.

2. Adriaens, H. J. M. T. S., Koning, W. L. D & Banning, R. (2000). Modeling piezoelectric actuators. IEEE/ASME Transactions on Mechatronics, Vol. 5, 331-341.

3. Albrecht, T., Despont, M., Eleftheriou, E., Bu, J. U., & Hirano, T. (2004). MEMS in mass storage systems. Enabling Technologies for MEMS and Nanodevices, Vol.1, Ch 6, 193–236.

4. Armstrong-Hélouvry, B. Dupont, P. & Wit, C. C. D. (1994). A survey of models, analysis tools and compensation methods for the control of machines with friction. Automatica, Vol. 30, 1083-1138.

5. Ballato, A. (1996). Piezoelectricity: History and new thrusts. Proceedings of the IEEE Ultrasonics Symposium, No. 1, 575–583.

6. Baril, C. G. & Gutman, P. (1997). Performance enhancing adaptive friction compensation for uncertain systems. IEEE Transaction on Control Systems Technology, Vol. 5, 466-479.

7. Bashash, S., & Jalili, N. (2007). Intelligence rules of hysteresis in the feedforward trajectory control of piezoelectrically-driven nanostagers. Journal of Micromechanics and Microengineering, Vol. 17, No. 2, 342–349.

8. Biediger, E., Lawrence, J., & Singhose, W. (2005). Improving trajectory tracking for systems with unobservable modes using command generation. American Control Conference, Vol. 1, 513-518.

9. Bitner, D.V., & Ukrainetx, P.R. (1990). Linear position control using simple solenoids and an electromagnet. Society of Automotive Engineers Transactions, Vol. 99, Issue 2, 376.

10. Bona, B. & Indri, M. (1995). Friction compensation and robustness issues in force/position controlled manipulators. IEE Proceedings on Control Theory Application, Vol. 142, 569-574.

11. Brinkerhoff, R., & Devasia, S. (2000). Output tracking for actuator deficient/ redundant systems: Multiple piezoactuator example. Journal of Guidance, Control, and Dynamics, Vol. 23, No. 2, 370–373.

12. Chang, T. N. (2002). Multiple degree-of-freedom piezoelectric actuator. U.S Patent number 06359370.

13. Chang, T. N. (2010). http://web.njit.edu/~chang/bio_2010.pdf.

14. Chang, T. N., Cheng, B., & Sriwilaijaroen, P. (2006). Motion control firmware for high speed robotic systems. IEEE Transactions on Industrial Electronics, Vol. 25, No. 5, 1713-1722.

15. Chang, T. N., Hou, E. & Godbole, K. (2003). Optimal input shaper design for high-speed robotic workcells. Journal of Vibration and Control, Vol. 9, 1359-1376.

16. Chang, T. N., Jaroonsiriphan, P., Bernhardt, M., & Ludden, P. (2006). Web-based command shaping of cobra 600 robot with a swinging load. IEEE Transactions on Industrial Informatics, Vol. 2 , No. 1, 59-69.

17. Chang, T. N., Parthasarathy, S., Wang, T., Gandhi, K., & Soteropolous, P. (2006). Automated liquid dispensing pin for DNA microarray applications. IEEE Transactions on Automation Science and Engineering, Vol.3, No. 2, 187-191.

18. Chang, T. N. & Sun, X. (2001). Analysis and control of monolithic piezoelectric nano-actuator. IEEE Transactions on Control Systems Technology, Vol. 9, 69-75.

19. Chang, T. N., Yuan, D., & Hanek, H. (2008). Feedforward control of a high precision robot with velocity deadzone. IEEE Transactions on Control Systems Technology, Vol. 16, No. 1, 94-102.

20. Cheung, N. C., Lim, K.W., & Rahman, M. F. (1993). Modelling a linear and limited travel solenoid. Industrial Electronics, Control, and Instrumentation. Proceedings of the IECON, International Conference on. Vol. 3, 1567-1572.

21. Ciliz, M. K. & Tomizuka, M. (2004). Neural network based friction compensation in motion control. Electronics Letters, Vol. 40, 752-753.

22. Croft, D., & Devasia, S. (1998). Hysteresis and vibration compensation for piezoactuators. Journal of Guidance, Control, and Dynamics, Vol. 21, No. 5, 710–717.

23. Croft, D., Shed, G., & Devasia, S. (2001). Creep, hysteresis, and vibration compensation for piezoactuators: Atomic force microscopy application. Journal of Dynamic Systems, Measurement and Control, Transactions of the ASME, Vol. 123, No. 1, 35–43.

24. Cutforth, C. F. & Pao, L. Y. (2004). Adaptive input shaping for maneuvering flexible structures. Automatica, Vol. 40, 685-693.

25. Despont, M., Drechsler, U., Häberle, W., Lantz, M. A., & Rothuizen, H. E. (2007). A vibration resistant nanopositioner for mobile parallel- probe storage applications. Journal of Microelectromechanical Sysems, Vol. 16, No. 1, 130–139.

26. Devasia, S. (2002). Should model-based inverse inputs be used as feedforward under plant uncertainty? IEEE Transactions on Automatic Control, Vol. 47, No. 11, 1865–1871.

27. Devasia, S., Eleftheriou, E. & Moheimani, S. O. R. (2007). A Survey of Control Issues in Nanopositioning. IEEE Transactions on Control Systems Technology, Vol. 15, 802-823.

28. Dijkstra, B. G. & Bosgra, O. H. (2003). Exploiting iterative learning control for input shaping with application to a wafer stage. Proceedings of the American Control Conference, 4811-4815.

29. Fasik, J. C. (1998). An inchworm actuator for the next generation space telescope. Burleigh Instruments, Inc., Fishers, NY.

30. Ferretti, G., Magnani, G. & Rocco, P. (2004). Single and multistate integral friction models. IEEE Transactions on Automatic Control, Vol. 49, 2292-2297.

31. Fukada, E. (2000). History and recent progress in piezoelectric polymers. IEEE Transactions on Ultrasonics, Ferroelectrics, and Frequency Control, Vol. 47, No. 6, 1277–1290.

32. Hekman, K., Singhose, W. & Lawrence, J. (2004). Input shaping with coulomb friction compensation on a solder cell machine. Proceedings of the 2004 American Control Conference, 728-733.

33. Hensen, R., Molengraft, M. & Steinbuch, M. (2001). High performance regulator control for mechanical systems subjected to friction. Proceedings of the 2001 IEEE International Conference on Control Applications, 200-205.

34. Horowitz, R. (2004). Microactuators for dual-stage servo systems in magnetic disk files. Springer Handbook of Nanotechnology, B. Bhushan, Ed. Berlin, Germany: Springer–Verlag, Ch. 31, 921–950.

35. Hu, H., Georgiou, H. M. S., & Ben-Mrad, R. (2005). Enhancement of tracking ability in piezoceramic actuators subject to dynamic excitation conditions. IEEE/ASME Transactions on Mechatronics, Vol. 10, No. 2, 230–9.

36. Hwang, C. (2008). Microprocessor-based fuzzy decentralized control of 2-D piezo-driven systems. IEEE Transactions on Industrial Electronics, Vol. 55, No. 3, 1411-1420.

37. IEEE standard on piezoelectricity, 1988.

38. Jin, M., Kang, S. H., & Chang, P. H. (2008). Robust compliant motion control of robot with nonlinear friction using time-delay estimation. IEEE Transactions on Industrial Electronics, Vol. 55, No. 1, 258-269.

39. Jung, H., Shim, J. Y., & Gweon, D. (2000). New open-loop actuating method of piezoelectric actuators for removing hysteresis and creep. Reviews of Scientific Instruments, Vol. 71, No. 9, 3436–3440.

40. Kajima, T., & Kawamura, Y. (1995). Development of a high-speed solenoid valve: Investigation of solenoids. IEEE Transactions on Industrial Electronics, Vol. 42, No. 1, 1-8.

41. Kapila, V., Tzes, A. & Yan, Q. (2000). Closed-loop input shaping for flexible structures using time-delay control. Transactions of the ASME, Vol. 122, 454-460.

42. Kermani, M. R., Wong, M., Patel, R. V., Moallem, M. & Ostojic, M. (2004). Friction compensation in low and high-reversal-velocity manipulators. Proceedings of the 2004 International Conference on Robotics & Automation, 4320-4325.

43. Kim, Y., & Lee, S. (2004). An approach to dual-stage servo design in computer disk drives. IEEE Transactions on Control Systems Technology, Vol. 12, No.1, 12–20.

44. Kobayashi, M., & Horowitz, R. (2001). Track seek control for hard disk dualstage servo systems. IEEE Transactions on Magnetics, Vol. 37, No. 2, 949–954.

45. Kuhnene, K., & Janocha, H. (2001). Inverse feedforward controller for complex hysteretic nonlinearities in smart-material systems. Control and Intelligent Systems, Vol. 29, No. 3, 74–83.

46. Lantz, M., Binnig, G., Despont, M., & Drechsler, U. (2005). A micromechanical thermal displacement sensor with nanometer resolution. Nanotechnology, Vol. 16, 1089–1094.

47. La-orpacharapan, C. & Pao, L. (2002). Shaped control for damped flexible structures with friction and slew rate limits. 41st IEEE Conference Decision and Control, 3099-3105.

48. Lawrence, J., Singhose, W. & Hekman, K. (2002). An analytical solution for a zero vibration input shaper for systems with coulomb friction. Proceeding of the American Control Conference.

49. Lawrence, J., Singhose, W. & Hekman, K. (2005). Friction-compensating command shaping for vibration reduction. Journal of Vibration and Acoustics, Vol. 127, 307-314.

50. Lee, S. H., & Royston, T. J. (2000). Modeling piezoceramic transducer hysteresis in the structural vibration control problem. Journal of Acoustical Society America, Vol. 108, No. 6, 2843–2855.

51. Lim, K. W., Cheung, N.C., & Rahman, M. F. (1994). Proportional control of a solenoid actuator. IECON International Conference on Industrial Electronics, Control and Instrumentation, Vol.3, 2045-2050.

52. Liu, X., Lara-Rosano, F. & Chan, C. W. (2004). Model-reference adaptive control based on neurofuzzy networks. IEEE Transactions on Systems, Man, and Cybernectics-Part C: Application and Reviews, Vol. 34, 302-309.

53. Marton, L., & Lantos, B. (2007). Modeling, identification and compensation of stick-slip friction. IEEE Transactions on Industrial Electronics, Vol. 54, No. 1, 1713-1722, & 511-521.

54. Meldrum, D. R, Pence, W. H., Moody, S. E., Cunningham, D. L., Holl, M., Wiktor, P. J., Saini, M., Moore, M. P., Jang, L.-S., Kidd, M., Fisher, C., & Cookson, A. (2001). Automated, integrated modules for fluid handling, thermal cycling and purification of DNA samples for high throughput sequencing and analysis. IEEE/ASME International Conference on Advanced Intelligent Mechatronics, 1211–1219.

55. Mrad, R. B., & Hu, H. (2002). A model for voltage to displacement dynamics in piezoceramic actuators subject to dynamic voltage excitations. IEEE/ASME Transactions on Mechatronics, Vol. 7, No. 4, 479–489.

56. MTI Instruments Inc. (2004). MTI-2100 Fotonic Sensor User's Manual.

57. National Instruments Corp. (1994). NI 6023E/6024E/6025E family specifications.

58. Olsson, H., Astrom, K. J., Canudas de Wit, C., Gafvert, M., & Lischinsky, P. (1998). Friction models and friction compensation. European Journal of Control, Vol. 4, Issue 3, 76-195.

59. Pan, J., Cheung, N.C., & Yang, J. (2005). High-precision position control of a novel planar switched reluctance motor. IEEE Transactions on Industrial Electronics, Vol. 52, No. 6, 1644-1652.

60. Pedrak, R., Ivanov, T., Ivanova, K., Gotszalk, T., Abedinov, N., Rangelowa, I. W., Edinger, K., Tomerov, E., Schenkel, T., & Hudek, P. (2003). Micromachined atomic force microscopy sensor with integrated piezoresistive, sensor and thermal bimorph actuator for high-speed tappingmode atomic force microscopy phase-imaging in higher eigenmodes. Journal of Vacuum Science & Technology B, Vol. 21, No. 6, 3102–3107.

61. Poty, A., Melchior, P., Orsoni, B., Levron, F., & Oustaloup, A. (2003). ZV and ZVD shapers for explicit fractional derivative systems. Proceedings of ICAR 2003.

62. Rihong, Z., Daocai, X., Zhixing, Y., & Jinbang, C. (1998). Research on systems for measurements of CCD parameters. Proceedings of SPIE Detectors, Focal Plane Arrays, Imaging Devices II, 297–301.

63. Rhim, S. & Book, W. J. (2004). Adaptive time-delay input shaping filter for flexible manipulator control. IEEE/ASME Transactions on Mechatronics, Vol. 9, 619-626.

64. Salapaka, S., Sebastian, A., Cleveland, J. P., & Salapaka, M. V. (2002). High bandwidth nano-positioner: A robust control approach. Review of Scientific Instruments, Vol. 73, No. 9, 3232–3241.

65. Sato, K., Mishima, Y. Tsuruta, K. & Murata, K. (2004). Adaptive H_∞ control for linear slider with friction compensation using σ -modification strategy. Proceedings of the 2004 IEEE International Conference on Control Applications, 794-799.

66. Schitter, G., & Stemmer, A. (2003). Model-based signal conditioning for high-speed atomic force and friction force microscopy. Microelectronic Engineering, Vol. 67–68, 938–944.

67. Sebastian, A., & Salapaka, S. M. (2005). Design methodologies for robust nano-positioning. IEEE Transactions on Control System Technology, Vol. 13, No. 6, 868–876.

68. Singer, N. C., & Seering, W. P. (1990). Preshaping command inputs to reduce system vibration. Journal of Dynamic Systems, Measurement, and Control, Vol.112, 76-82.

69. Singhose, W. E. (1997). Command generation for flexible systems. Ph.D. Dissertation, MIT.

70. Shen, Q., Chang, T. N., & Yu, L. (2007). Automated real-Time spotting system for DNA/protein microarray applications. Industrial Electronics, ISIE 2007. IEEE International Symposium.

71. Shen, Q., Chang, T. N., & Yu, L. (2008). Control and implementation of a real-time liquid spotting system for microarray applications. IEEE Transactions on Industrial Electronics, Vol. 55, No. 9, 3266-3272.

72. Shieh, H., Lin, F., Huang, P., & Teng, L. (2006). Adaptive displacement control with hysteresis modeling for piezoactuated positioning mechanism. IEEE Transactions on Industrial Electronics, Vol. 53, No. 3, 905- 914.

73. Spectrum Digital Incorporated (2003). TMS320C6416T-DSK technical reference.

74. Sun, Q, Anderson, J. N. & Alouani, A. T. (1990). A scheme for estimating joint friction using a model-based controller. 22nd Southeastern Symposium on System Theory, 137-140.

75. Sun, X. (2001). Analysis and control of monolithic piezoelectric nano-actuator. Ph.D. Dissertation, New Jersey Institute of Technology.

76. Su, Y. X., Duan, B. Y., Zheng, C. H., Zhang, Y. F., Chen, G. D. & Mi, J. W. (2004). Disturbance-rejection high-precision motion control of a Stewart platform. IEEE Transaction on Control Systems Technology, Vol. 12, 364-374.

77. Tan, K. K., Huang, S. N., Dou, H. F., Lee, T. H., Chin, S. J. & Lim, S. Y. (2001). Adaptive robust motion control for precise trajectory tracking applications. ISA Transactions, Vol. 40, 57-71.

78. Tan, K.K., Lee, T. H., & Zhou, H. X. (2001). Micro-positioning of linearpiezoelectric motors based on a learning nonlinear PID controller. IEEE/ASME Transactions on Mechatronics, Vol. 6, No. 4, 428–36.

79. Tan, X., & Baras, J. S. (2005). Adaptive identification and control of hysteresis in smart materials. IEEE Transactions on Automatic Control, Vol. 50, No. 6, 827–839.

80. Tao, G., & Kokotovic, P. V. (1995). Adaptive control of plants with unknown hysteresis. IEEE Transactions on Automatic Control, Vol. 40, No. 1, 200–212.

81. Tas. N., Wissink, J., Sander, L., Lammerink, T., & Elwenspoek, M. (1998). Modeling, design and testing of the electrostatic shuffle motor. Sensors Actuators A—Physical, Vol. 70, 171–178.

82. Texas Instrument (2005). Code composer studio quick start reference guide.

83. Tien, S., Zou, Q., & Devasia, S. (2005). Iterative control of dynamics-coupling-caused errors in piezoscanners during high-speed AFM operation. IEEE Transations on Control System Technology, Vol. 13, No. 6, 921–931.

84. Tomizuka, M. (1993). On the compensation of friction in precision motion control. Proceedings of Asia-Pacific Workshop on Advances in Motion Control, 69-74.

85. Tsai, M. S., & Chen, J. S. (2003). Robust tracking control of a piezoactuator using a new approximate hysteresis model. Journal of Dynamic Systems, Measurement and Control, Vol. 125, 96–102.

86. Ueno, T., Qiu, J., & Tani, J. (2003). Magnetic force control with composite of giant magnetostrictive and piezoelectric materials. IEEE Transactions on Magnetic, Vol. 39, No. 6, 3534–3540.

87. Verma, S., Kim, W., & Shakir, H. (2005). Multi-axis Maglev nanopositioners for precision manufacturing and manipulation applications. IEEE Transactions on Industry Applications, Vol. 41, No. 5, 1159–1167.

88. Wai, R., & Chang, L. (2006). Adaptive stabilizing and tracking control for a nonlinear inverted-pendulum system via sliding-mode technique. IEEE Transactions on Industrial Electronics, Vol. 53, No. 2, 674- 692.

89. Wai, R., & Liu, W. (2003). Nonlinear control for linear induction motor servo drive. IEEE Transactions on Industrial Electronics, Vol. 50, No.2, 920-935.

90. Wang, X. –S, Hong, H. & Su, C. –Y. (2003). Model reference adaptive control of continuous-time system with unknown input dead-zone. IEEE Proceedings on Control Theory Applications, Vol. 150, 261-266.

91. Wang, Y.,Megli, T. & Haghgooie, M. (2002). Modeling and control of electromechanical valve actuator. Society of Automotive Engineers, 2002-01-1106.

92. Wang, Y. Xiong, Z., Ding, H. & Zhu, X. (2004). Nonlinear Friction compensation and disturbance observer for a high-speed motion platform. Proceedings of the 2004 IEEE International Conference on Robotics & Automation, 4515-4520.

93. White, D. L., & Wood, O. R. (2000). Novel alignment system for imprint lithography. Journal of Vacuum Science and Technology *B*, Vol. 18, No. 6, 3552–3556.

94. Wit, C. C. D., Olsson, H., Åström, K. J. & Lischinsky, P. (1995). A new model for control of systems with friction. IEEE Transactions on Automatic Control, Vol. 40, 419-425.

95. Xu, Y., & Jones, B. (1997). A simple means of predicting the dynamic response of electromagnetic actuators. Mechatronics, Vol. 7, Issue 7, 589-598.

96. Yoneya, A., & Kondo, T. (1998). Two-valued PID controller. IEEE Transactions on Industrial Electronics, Vol. 45, No. 1, 183-184.

97. Yuan, D., & Chang, T. N. (2008). Model reference command shaper design with applications to a high-speed robotic workcell with variable loads. IEEE Trans. on Industrial Electronics, Vol. 55, No. 2, 842-851.

98. Yuan, Q., & Li, P. Y. (2004). Self-calibration of push-pull solenoid actuators in electrohydraulic valves. Proceedings of 2004 ASME International Mechanical Engineering Congress.

99. Yu, L., & Chang, T. N. (2008). Model reference zero vibration balance control of dual solenoid position actuator. International Symposium on Flexible Automation.

100. Yu, L., & Chang, T. N. (2010). Model reference zero vibration control of ultrahigh precision piezoelectric nanopositioner, American Control Conference 2010.

101. Yu, L., & Chang, T. N. (2008). Variable model reference high precision position control of dual solenoid actuator. Industrial Electronics, IECON 2008. 34th Annual Conference of the IEEE.

102. Yu, L., & Chang, T. N. (2007). Zero vibration on-off position control of dual solenoid actuator. Industrial Electronics, IECON 2007. 33rd Annual Conference of the IEEE.

103. Yu, L., & Chang, T. N. (2010). Zero vibration on-off position control of dual solenoid actuator. IEEE Transactions on Industrial Electronics, Vol. 57, No. 7, 2519-2526.

104. Zhao, Y., & Jayasuriya, S. (1995). Feedforward controllers and tracking accuracy in the presence of plant uncertainties. ASME Journal of Dynnamic System, Measurement and Control, Vol. 117, 490–495.

105. Zou, Q., Leang, K. K., Sadoun, E., Reed, M. J., & Devasia, S. (2004). Control issues in high-speed AFM for biological applications: Collagen imaging example. Asian Journal of Control: Special Issue Advanced Nano-Technology Control, Vol. 6, No. 2, 164–178.